CZECH TECHNICAL UNIVERSITY
IN PRAGUE

Faculty of Nuclear Sciences and Physical Engineering

Department of Physics

Master's thesis

Incoherent photoproduction of J/ψ in ultra-peripheral Pb–Pb collisions with ALICE

Author: Bc. David Grund
Supervisor: prof. Jesús Guillermo Contreras Nuño, Ph.D.
Academic year: 2020/2021

ČESKÉ VYSOKÉ UČENÍ TECHNICKÉ
V PRAZE

Fakulta jaderná a fyzikálně inženýrská

Katedra fyziky

Diplomová práce

Nekoherentní fotoprodukce J/ψ v ultra-periferálních Pb–Pb srážkách na ALICE

Autor: Bc. David Grund
Školitel: prof. Jesús Guillermo Contreras Nuño, Ph.D.
Akademický rok: 2020/2021

ČESKÉ VYSOKÉ UČENÍ TECHNICKÉ V PRAZE
FAKULTA JADERNÁ A FYZIKÁLNĚ INŽENÝRSKÁ
PRAHA 1 - STARÉ MĚSTO, BŘEHOVÁ 7 - PSČ 115 19

Katedra: fyziky *Akademický rok:* 2020/2021

ZADÁNÍ DIPLOMOVÉ PRÁCE

Student:	Bc. David Grund
Studijní program:	Aplikace přírodních věd
Obor:	Experimentální jaderná a částicová fyzika
Název práce: (česky)	Nekoherentní fotoprodukce J/psi v ultra-periferálních Pb-Pb srážkách na ALICE
Název práce: (anglicky)	Incoherent photoproduction of J/psi in ultra-peripheral Pb-Pb collisions with ALICE

Pokyny pro vypracování:

1) Shrnutí nejnovějších výsledků z měření nekoherentní fotoprodukce J/psi v Pb-Pb srážkách na ALICE
2) Vypracování rešerše o fenomenologických modelech popisujících nekoherentní fotoprodukci J/psi
3) Studium nekoherentní fotoprodukce J/psi v oblasti centrální rapidity v Pb-Pb srážkách na ALICE v datech z Run 2 urychlovače LHC

Doporučená literatura:

[1] S. R. Klein and H. Mäntysaari: Imaging the nucleus with high-energy photons. Nature Rev. Phys. 1, 662-674 (2019)

[2] ALICE Collaboration: Coherent J/psi photoproduction at forward rapidity in ultra-peripheral Pb-Pb collisions at sNN = 5.02 TeV. Phys. Lett. B 798, 134926 (2019)

[3] T. Laapi and H. Mäntysaari: Incoherent diffractive J/Psi-production in high energy nuclear DIS. Phys. Rev. C 83, 065202 (2011)

Jméno a pracoviště vedoucího diplomové práce:

prof. Jesús Guillermo Contreras Nuño, Ph.D., Katedra fyziky
Fakulta jaderná a fyzikálně inženýrská ČVUT v Praze

Datum zadání diplomové práce: 23.10.2020

Termín odevzdání diplomové práce: 03.05.2021

Doba platnosti zadání je dva roky od data zadání.

.....
garant oboru

.....
vedoucí katedry

.....
děkan

V Praze dne 23.10.2020

Prohlášení

Prohlašuji, že jsem svou diplomovou práci vypracoval samostatně a použil jsem pouze podklady (literaturu, projekty, software, atd.) uvedené v přiloženém seznamu.

Nemám závažný důvod proti použití tohoto školního díla ve smyslu § 60 Zákona č. 121/2000 Sb., o právu autorském, o právech souvisejících s právem autorským a o změně některých zákonů (autorský zákon).

V Praze dne 3. května 2021

.....
David Grund

Acknowledgments

I wish to express my deepest gratitude to my supervisor, prof. Jesús Guillermo Contreras Nuño, Ph.D., for providing guidance, for many helpful discussions, patient advice, invaluable insight into the topic and language corrections. Many thanks also go to Mgr. Michal Broz, Ph.D. for the preparation of nanoAOD datasets that constituted the starting point of the experimental analysis. Lastly, I would like to extend my sincere thanks to my family and to my girlfriend for their continuous support.

David Grund

Title:
Incoherent photoproduction of J/ψ in ultra-peripheral Pb–Pb collisions with ALICE

Author: Bc. David Grund

Specialisation: Experimental Nuclear and Particle Physics

Sort of project: Master's thesis

Supervisor: prof. Jesús Guillermo Contreras Nuño, Ph.D., Department of Physics, Faculty of Nuclear Sciences and Physical Engineering, Czech Technical University in Prague

Consultant: —

Abstract: The analysis of diffractive photoproduction of vector mesons in ultra-peripheral collisions of heavy ions at the LHC offers an efficient way to probe the structure of nuclei at low Bjorken-x. It enables one to examine the effects of high-energy QCD phenomena such as nuclear shadowing or gluon saturation, which are nowadays actively researched. In particular, with the incoherent photoproduction, one can study event-by-event fluctuations of the transverse structure of nucleons.

In the experimental part of this master's thesis, the analysis of the incoherent photoproduction of J/ψ mesons in Pb–Pb collisions at the centre-of-mass energy of $\sqrt{s_{\mathrm{NN}}} = 5.02$ TeV with ALICE is presented. The J/ψ mesons are reconstructed using the dimuon decay channel and the first estimate of the incoherent photoproduction cross section at midrapidity is determined. A substantial increase in the number of measured events is observed with respect to the previous ALICE measurement.

Key words: ALICE, ultra-peripheral collisions, incoherent photoproduction, J/ψ

Název práce:
Nekoherentní fotoprodukce J/ψ v ultra-periferálních Pb–Pb srážkách na ALICE

Autor: Bc. David Grund

Obor: Experimentální jaderná a částicová fyzika

Druh práce: Diplomová práce

Vedoucí práce: prof. Jesús Guillermo Contreras Nuño, Ph.D., Katedra fyziky, Fakulta jaderná a fyzikálně inženýrská, České vysoké učení technické v Praze

Konzultant: —

Abstrakt: Analýza difrakční fotoprodukce vektorových mezonů v ultraperiferních srážkách těžkých iontů na urychlovači LHC představuje účinný způsob, jak lze zkoumat strukturu jader při nízkých Bjorkenových x. Tyto procesy umožňují prozkoumat účinky některých jevů ve kvantové chromodynamice při vysokých energiích, jako jsou jaderné stínění či gluonová saturace, v jejichž oblasti dnes probíhá aktivní výzkum. Konkrétním příkladem je nekoherentní fotoprodukce, s jejíž pomocí lze studovat fluktuace příčné struktury nukleonů.

V experimentální části této diplomové práce je představena analýza nekoherentní fotoprodukce mezonů J/ψ v Pb–Pb srážkách při těžišťové energii $\sqrt{s_{\mathrm{NN}}} = 5.02$ TeV na experimentu ALICE. J/ψ mezony jsou zrekonstruovány z rozpadu na mionové páry a je stanoven prvotní odhad účinného průřezu nekoherentní fotoprodukce v oblasti centrální rapidity. Je pozorován výrazný nárůst v počtu nalezených částic vůči předchozímu měření na ALICE.

Klíčová slova: ALICE, ultraperiferní srážky, nekoherentní fotoprodukce, J/ψ

Contents

List of figures

List of tables

Introduction

This master's thesis is dedicated to the study of incoherent J/ψ photoproduction in ultra-peripheral collisions (UPCs) of lead ions with ALICE at the Large Hadron Collider (LHC).

In UPCs, two heavy ions pass by at a distance that is larger than the sum of their radii, which enables one to study the electromagnetic processes between the participants since any hadronic interactions that would overshadow them are suppressed. One of the processes that may occur in UPCs is the so-called diffractive photoproduction of vector mesons, where, as a result of the interaction between the emitted virtual photon and the nuclear target, a vector meson is produced. If the photon interacts coherently with the whole nucleus, the produced vector mesons have a rather low average transverse momentum, $\langle p_{\mathrm{T}} \rangle \approx 60$ MeV/c. The dependence of the cross section of the coherent photoproduction on the square of the transverse momentum of the vector meson is directly related to the transverse distribution of gluons inside the target.

On the other hand, if the photon interacts incoherently, with only a single nucleon, the $\langle p_{\mathrm{T}} \rangle$ of the photoproduced vector mesons reaches several hundreds of MeV/c. In a Good-Walker approach, the incoherent process is sensitive to event-by-event fluctuations of the transverse structure of the target. Nowadays, it is a well-known fact that the hadronic structure evolves with the energy of the probe, or in other words, depends on the value of the so-called Bjorken-x variable. As will be shown, the UPCs studied at hadronic colliders such as the LHC are a very powerful experimental instrument to examine the structure of hadrons in the region of low Bjorken-x and to study the associated high-energy QCD phenomena such as gluon saturation or nuclear gluon shadowing.

The thesis is organised as follows. In Chapter 1, the historical development in the study of the structure of hadrons is summarised, with the emphasis placed on the results from the deeply inelastic scattering (DIS) experiments and their interpretation using the parton model. The above-mentioned nonlinear effects in QCD, gluon saturation and nuclear shadowing, are also introduced.

Chapter 2 is dedicated to the physics of ultra-peripheral collisions and, in particular, to the description and classification of the photoproduction of vector mesons in Pb–Pb and p–Pb collisions. In addition, the calculation of the energy spectrum of photons that are emitted by the nuclei is briefly described.

Chapter 3 then offers an overview of the various models that describe the interaction between the photon and the target and thus give predictions on the so-called photonuclear cross section. First, the STARlight model based on the vector meson dominance, and then the concept of models employing perturbative QCD calculations at the leading order, are described. Second, several models derived from the colour dipole formalism are summarised, including the models, where the transverse hadronic structure is parametrised in terms of hot spots, which describe regions of high gluon density.

The experimental infrastructure of ALICE at the LHC is presented in Chapter 4. In

addition to a general overview of the experiment, the detectors that are of vital importance for the measurements of UPCs are described.

The previous measurement of the incoherent J/ψ photoproduction with ALICE is reviewed in Chapter 5. It is based on data collected in Pb–Pb collisions at $\sqrt{s_{\mathrm{NN}}} = 2.76$ TeV during Run 1 of the LHC. The chapter is then suplemented with the overview of the latest ALICE measurements of the coherent J/ψ and $\psi(2S)$ photoproduction.

My own analysis, where the incoherent J/ψ photoproduction at midrapidity in the Pb–Pb collisions at the higher centre-of-mass energy of $\sqrt{s_{\mathrm{NN}}} = 5.02$ TeV is studied for the first time, is presented in Chapter 6. All the steps that are necessary to obtain the first estimate of the incoherent cross section are discussed in detail. Should the fluctuations of the subnucleonic structure be dominant, one may expect an enhancement, with respect to the case without fluctuations, of the incoherent processes, which would lead to somewhat higher values of the cross section.

The references cited in this thesis are those from where the information was obtained, but not necessarily the original sources.

Chapter 1

The structure of hadrons

From today's perspective, dramatic progress has been made in the past 120 years towards the understanding of the structure of atomic nuclei. The discovery of spontaneous radioactivity by Henri Becquerel in 1896 can surely be considered a milestone as it resulted in the progressive development of nuclear physics as a discipline distinct from contemporary atomic physics. However, it was not until 1911 that the atomic nucleus was discovered by Ernest Rutherford and his colleagues Hans Geiger and Ernest Marsden in the famous gold foil experiment. Then, another 20 years had to pass until the first realistic description of nuclei such as the liquid drop model or the early attempts towards the nuclear shell model were developed, following the discovery of the neutron by James Chadwick in 1932.

A huge step forward was taken by the end of 1960s when the development of particle accelerators enabled to probe the inner structure of nucleons with high-energy electrons. This process, known today as *deeply inelastic scattering* (DIS), can be considered an extension of the Rutherford scattering with much finer resolution thanks to the higher energies of the particle beams. The early DIS experiments were conducted at the 20 GeV Stanford linear accelerator in SLAC, which was completed in 1966. In 1990, J. I. Friedman, H. W. Kendall and R. E. Taylor from MIT and SLAC were awarded the Nobel Prize in Physics [1] for their pioneering contributions to the DIS experiments, results of which later provided experimental evidence of the quark model.

In this chapter, the inner structure of nucleons and nuclei, or more generally of any composite particles that are held by the strong force—hadrons, will be described. Most of the information concerning DIS and the parton model were taken from the lecture handouts by M. Thomson [2] and were sometimes complemented with historical remarks from the Nobel lecture by J. I. Friedman [3]. A similar review has been already given in the Research Project [4], where some parts are covered in more detail.

1.1 Deeply inelastic scattering

Generally, DIS is the scattering of a lepton (most often an electron or a neutrino) off a nucleon with the energy high enough to cause the latter to disintegrate. At the leading order of the perturbative expansion, it can be pictured as an exchange of a single virtual particle, a photon or an electro-weak gauge boson ($W^{\pm}$, Z^0). However, in the considered kinematic range, the contribution from the massive gauge boson will be typically negligible. Hence, the further discussion will be restricted to the most common example, the proton-electron scattering depicted in Fig. 1.1.

The process will be described in the laboratory frame, i.e. the rest frame of the target

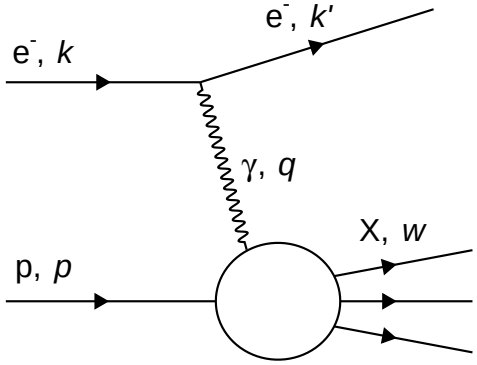

Figure 1.1: Sketch of the deeply inelastic scattering of an electron off a proton. The letters written in italics denote the four-momenta of the corresponding particles.

proton. The four-momenta of the participants are denoted as $k = (E_e,\boldsymbol{k})$ (the incident electron), $k' = (E'_e,\boldsymbol{k'})$ (the scattered electron), $p = (M_p,\boldsymbol{0})$ (the target proton) and $w = (W,\boldsymbol{w})$ (the hadronic state X). The kinematics of DIS can be described by a set of Lorentz-invariant variables:

- The *virtuality* of the exchanged photon $Q^2 = -q^2 = (k - k')^2$, which corresponds to the squared momentum transfer between the electron and the target proton.
- The variable $\nu = \frac{pq}{M_p}$, which is, in this frame, equal to the energy loss of the incident electron, $\nu = E_e - E'_e$.
- The *invariant mass* of the final hadronic state $W^2 = (p + q)^2 = M_p^2 + 2pq - Q^2$.
- The *Bjorken variable* defined as $x = \frac{Q^2}{2pq} = \frac{Q^2}{2M_p\nu}$. In the elastic case, the proton remains intact, thus $W^2 = M_p^2$, which is satisfied for $2pq = Q^2$ (equivalent to stating that $x = 1$). In DIS, values of Bjorken-x range between 0 and 1.
- The *inelasticity* $y = \frac{pq}{pk}$. In this system, y can be expressed as $y = \frac{\nu}{E_e}$, so it corresponds to the fraction of energy loss of the incoming electron. In the case of elastic scattering $y = 0$, while $y \in (0,1]$ in the inelastic case.

In the elastic electron-proton scattering, the differential cross section $\mathrm{d}\sigma/\mathrm{d}\Omega$ is given by the well-known Rosenbluth formula, see e.g. [4]. The inelastic cross section, however, has to be expressed in terms of two independent variables from the list above, the form that is often used reads

$$\frac{\mathrm{d}^2\sigma}{\mathrm{d}x\mathrm{d}Q^2} = \frac{4\pi\alpha^2}{Q^4}\left[\left(1 - y - \frac{M_p x y}{s}\right)\frac{F_2(x,Q^2)}{x} + y^2 F_1(x,Q^2)\right], \tag{1.1}$$

where α is the fine-structure constant and $F_1(x,Q^2)$, $F_2(x,Q^2)$ are the dimensionless proton structure functions. The early results on the measured inelastic cross section showed two surprising features. First, the cross section showed a rather weak Q^2-dependence at fixed W^2 and did not fall as rapidly with increasing Q^2 as the previously examined elastic cross section.

The second unexpected behaviour is referred to as *Bjorken scaling* and was suggested by J. D. Bjorken in 1969. Originally, it was observed that the structure functions F_1 and F_2 were almost constant functions of Q^2 at a fixed value of x and only *scaled* with the dimensionless number x. This led R. Feynman in around 1969 to develop the so-called *parton model*, in which

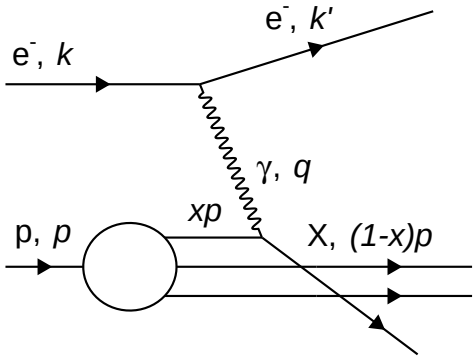

Figure 1.2: The parton model of the proton-electron DIS. The letters written in italics denote the four-momenta of the corresponding particles. The struck parton carries the fraction x of the longitudinal momentum p of the proton.

the proton is thought to be build up of point-like constituents, *partons*, but without specifying what the partons physically are.

1.2 Feynman's parton picture

The parton model is defined in the *infinite momentum frame* (IMF) of the proton. In this frame, one can neglect the proton mass as well as the parton masses and their transverse momentum. Due to the relativistic time dilation, the proton may be perceived as a stream of non-interacting (almost free) point-like partons. Then, as indicated in Fig. 1.2, DIS can be interpreted as the elastic scattering of the electron off one of the partons. Furthermore, the physical meaning of the Bjorken variable can be inferred from the parton description. In the IMF, x corresponds to the fraction of the proton four-momentum p (or its classical momentum $\boldsymbol{p}$) that is carried by the struck parton.

As highlighted in [3], many attempts to explain the results of DIS experiments emerged at the beginning of the 1970s. After several years of ongoing experiments, it was eventually the *constituent quark model*, based on the flavour SU(3) symmetry, which provided the most satisfying predictions. This model was independently proposed by M. Gell-Mann and G. Zweig in 1964 as an effective ordering scheme to classify hadrons. Some of the successes of the quark model will be presented in the rest of this section.

Within the quark model, one can easily obtain the predictions of the parton model for the structure functions F_2 and F_1. Equation (1.1) can be compared with the cross section for the elastic scattering of an electron off a point-like spin-1/2 quark multiplied by the probability of finding a particular quark type with the momentum fraction between x and $x + \mathrm{d}x$ inside the proton. For the quark of a flavour f, this probability can be denoted as $f^p(x)\mathrm{d}x$, where the superscript p specifies that the proton is considered. Summing over possible flavours of *valence* quarks and *sea* $q\overline{q}$ pairs, this comparison gives

$$F_2 = x \sum_f e_f^2 \left[f^p(x) + \overline{f}^p(x) \right] , \tag{1.2}$$

where $\overline{f}^p(x)$ is the probability distribution for the corresponding antiquark and e_f is the fraction of the elementary charge e of a quark of the flavour f, e.g. $e_f = -1/3$ for the d quark.

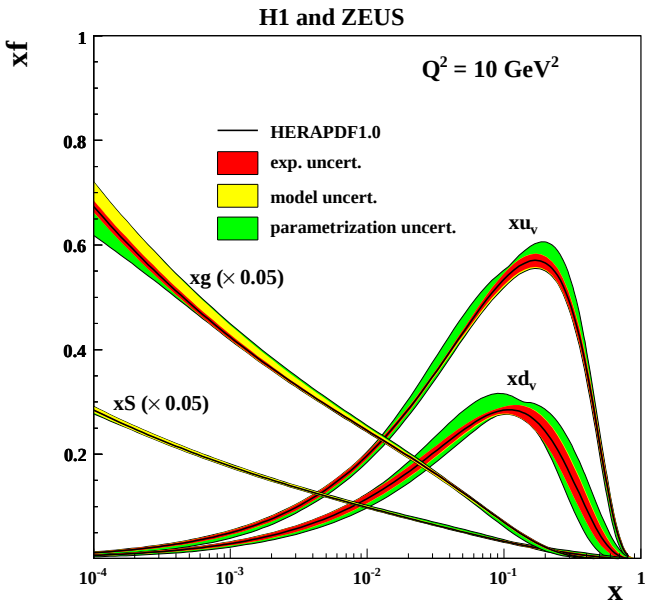

Figure 1.3: PDFs for the proton at $Q^2 = 10$ GeV^2 extracted from HERA data [5]. $S(x)$ stands for the contribution from all sea quarks and antiquarks. Note that the values of the gluon and sea distributions are suppressed by a factor of 20 for displaying purposes.

Generally, for a given hadron h, the $f^h(x)$ functions are referred to as the *parton distribution functions* (PDFs) and characterise its quark content. In contrast to the structure functions F_1 and F_2, the PDFs are universal in the sense that they do not depend on the type of scattering, i.e. which particle is used as a probe.

In the early 1970s, the first experimental data on the neutron structure functions were extracted from measurements with deuterium targets. It was found that both the proton and neutron structure functions obey the Callan-Gross relation, $F_2(x) = 2xF_1(x)$, which can be derived under the assumption that the partons are spin-1/2 particles. Applying the isospin symmetry and integrating the measured proton and neutron structure functions over the whole Bjorken-x range, it was later shown that the up quarks in the proton carry twice the momentum of the down quarks, as expected.

In 1972, new experimental data were extracted from the DIS experiments with neutrinos and antineutrinos, which independently verified many predictions of the quark model. These experiments were performed at the 24 GeV Synchrotron at CERN, making use of the large heavy-liquid bubble chamber Gargamelle designed for the detection of neutrinos. Refer to [3, 4] for more details.

Surprisingly, it emerged that the contribution from all valence and sea quarks accounts for only $\approx 50\%$ of the total proton momentum. This suggests that the rest has to be carried by neutral particles (*gluons*) that do not posses the electroweak charge and hence cannot be probed by leptons. The gluon content is described by the gluon distribution function $g^p(x)$.

The proton structure is in fact very dynamic and dramatically evolves with Bjorken-x. Figure 1.3 shows the x-dependence of the proton PDFs determined on the basis of the measurements at HERA, the former German electron-proton collider. HERA, located at DESY in Hamburg, operated between 1992 and 2007 and especially two of its experiment, ZEUS and H1, extensively contributed to the measurements of the proton PDFs and the structure functions

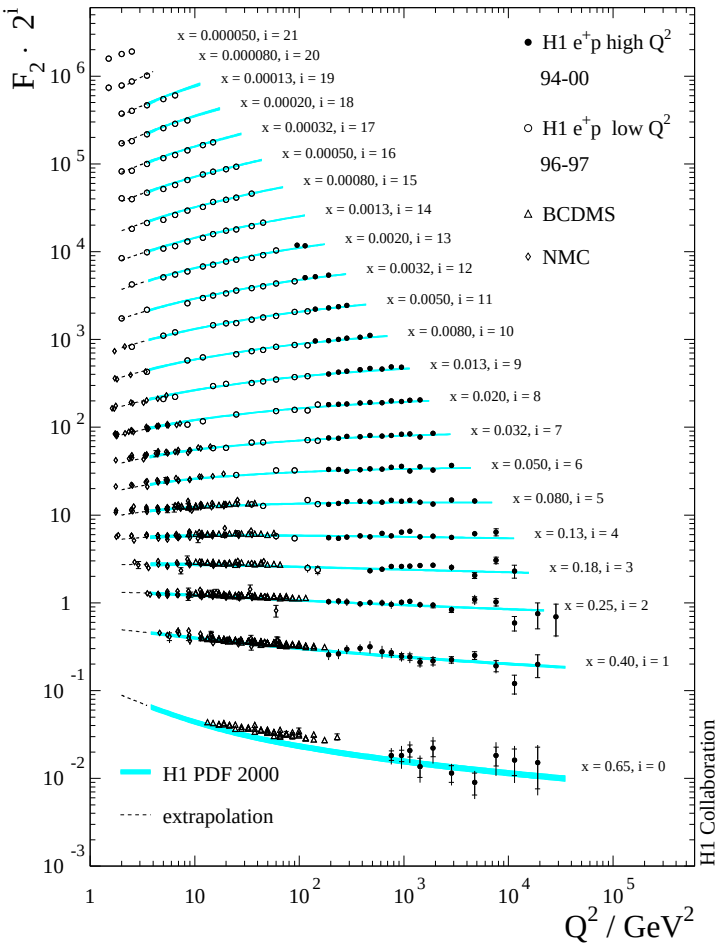

Figure 1.4: Q^2-dependence of the proton structure function F_2 measured at various values of Bjorken-x [7]. Note that the vertical axis is in the log scale.

down to $x \approx 10^{-5}$. As shown in Fig. 1.3, towards the low-x region ($x < 0.1$), the contribution from gluons and sea pairs increasingly dominates over the *uud* valence quarks.

Returning back to Bjorken scaling, it must be noted that it is not an exact phenomenon and is valid only in a specific kinematic limit known as *Bjorken limit*, where $Q^2 \to \infty$ and $\nu \to \infty$ with $x = Q^2/(2M_p\nu)$ kept finite. This was later demonstrated in experiments, as can be seen in Fig. 1.4. The scaling holds in the intermediate ($x \sim 0.1$) region, but is clearly violated in the region of low ($x \lesssim 0.05$) and high ($x > 0.2$) Bjorken-x, which were experimentally accessed later on. This reminds us that both the structure functions and the PDFs are generally Q^2-dependent. Simply speaking, the scaling violation can be explained taking into account the interactions between the partons (quarks and gluons) themselves and is correctly predicted by quantum chromodynamics (QCD) [6].

1.3 QCD evolution and gluon saturation

In DIS, it is the virtuality of the photon that determines the resolving power. The photon of the virtuality Q^2 thus probes the partons of the apparent size $1/Q^2$ [8]. If Q^2 is large enough, e.g. in the Bjorken limit, the proton appears to be a dilute system of tiny quarks and gluons and the phase space is sparsely occupied [8]. This corresponds to the infinite momentum frame, where

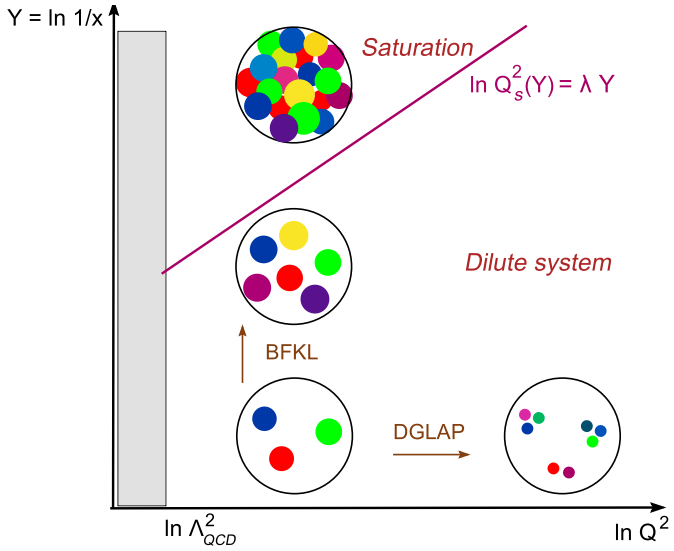

Figure 1.5: The hadron phase diagram [9]. Q^2 denotes the virtuality of the probe, x is the momentum fraction of the partons and Q_s stands for the saturation scale. The coloured dots represent the partons and the grey shaded area on the left indicates the region where the value of the QCD coupling constant $\alpha_s(Q)$ is too large to allow for perturbative calculations.

the parton model is formulated. The Q^2 evolution of the PDFs in this limit can be conveniently calculated perturbatively since the QCD coupling constant is a monotonically decreasing function of Q [8]. Such a Q^2 evolution is described by the linear DGLAP (Dokshitzer-Gribov-Lipatov-Altarelli-Parisi) equation and is illustrated by the horizontal arrow in Fig. 1.5.

Another important limit in QCD dynamics is reached when $s \to \infty$ and $x \to 0$ at fixed Q^2 and is schematically marked by the vertical arrow in Fig. 1.5. This asymptotic regime is called the Regge-Gribov limit [9]. Moving towards the region of low Bjorken-x, it was shown that the number of gluons grows rapidly (see Fig. 1.3), so one can neglect any additional contributions from quarks. The energy evolution of the hadron system in this region is described by the linear BFKL (Balitsky-Fadin-Kuraev-Lipatov) equation [9].

However, the gluon PDFs cannot rise indefinitely [10]. Sooner or later, the gluon phase space is so densely occupied that the gluons start to overlap. This regime of QCD is known as *gluon saturation* but has not yet been conclusively observed. As QCD allows for the gluon self-coupling, the gluons begin to *recombine* ($gg \to g$), which counteracts the increase in the number of partons caused by the energy evolution and leads to the formation of a balanced state. The momentum scale $Q_s(x)$, where the nonlinear effects such as gluon recombination start to play a major role, is called the *saturation scale* and has a form $Q_s^2(x) \propto x^{-\lambda}$ with the saturation exponent $\lambda \simeq 0.25$ [9]. At larger Q^2, higher energies (lower Bjorken-x) have to be reached in order to probe the saturation region. The energy evolution of hadrons in the saturated regime can be studied for example with the BK (Balitsky-Kovchegov) equation.

1.4 Nuclear shadowing

So far, only nucleons as individual hadrons were taken into account in the discussion. Since 1970s, it is a well-known fact that the nuclear structure functions $F_2^A(x,Q^2)$ cannot be considered as a mere superposition of the nucleon structure functions $F_2^{\text{nuc}}(x,Q^2)$ [11]. Instead, to study the

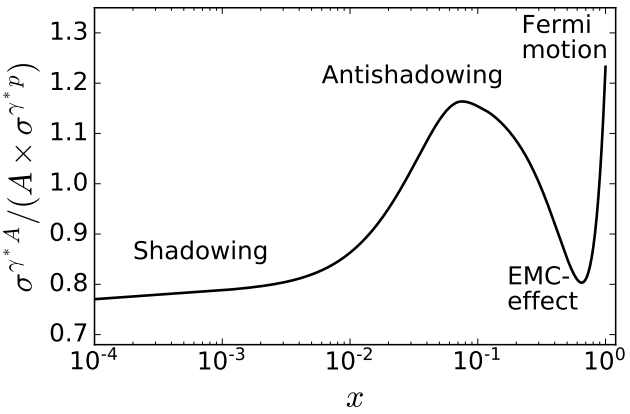

Figure 1.6: Different nuclear effects observed in DIS with nuclear targets at fixed Q^2 [10].

effects of the nuclear environment on the structure, one introduces the ratio

$$R_{F_2}^A = \frac{F_2^A(x,Q^2)}{A \cdot F_2^{\text{nuc}}(x,Q^2)}\,, \tag{1.3}$$

where A is the mass number of a given nucleus. The nucleon structure function is usually computed as an average of the deuteron structure function, $F_2^{\text{nuc}}(x,Q^2) = F_2^{\text{deu}}(x,Q^2)/2$, because the structure is assumed to be negligibly modified in such a small nuclear system [11].

It was discovered that the way how the PDFs of a bound nucleon are modified by the nuclear environment with respect to the PDFs of a free nucleon depends on Bjorken-x. One has to distinguish between four distinct regions [10, 11] as indicated in Fig. 1.6:

- The enhancement $R_{F_2}^A > 1$ at $x \sim 1$ caused by the Fermi motion of nucleons in the nucleus.
- The shadowing $R_{F_2}^A < 1$ at $0.3 \lesssim x \lesssim 0.8$ known as the *EMC effect*. It was first observed in 1983 by the European Muon Collaboration at CERN.
- The antishadowing $R_{F_2}^A > 1$ in the intermediate region $0.1 \lesssim x \lesssim 0.3$ enforced by momentum conservation.
- Eventually, the *nuclear shadowing* dominates in the lowest Bjorken-x region $x \lesssim 0.1$. It can be pictured as follows: two small-x gluons might fuse together, forming a single gluon with higher momentum [10]. This is likely to occur in heavy-density environments, such as near the centres of heavy nuclei. As a result, the nuclear PDFs experience suppression at small x.

The nuclear structure and the related effects such as the nuclear shadowing are nowadays extensively studied in photoproduction processes in ultra-peripheral collisions. This topic will be addressed in Chapter 2. In order to extract data on the nuclear shadowing from the experimentally measured cross sections, one defines the so-called *nuclear suppression factor* which will be introduced in Sec. 3.7.

Chapter 2

Ultra-peripheral collisions

Even though the inclusive[1] DIS experiments presented in the previous chapter constitute a straightforward way to examine the structure of hadrons, more complex physical processes have to be considered if one wishes to obtain more detailed information[2] about the inner structure [10]. Example of such a process is the *photoproduction*.

Both DIS and photoproduction off proton targets were extensively studied at HERA, but the world still lacks an *electron-ion collider* (EIC) that would be able to efficiently probe the structure of nuclei [10]. In January 2020, however, it was finally decided that an EIC will be built over the next decade upon the existing infrastructure of the Relativistic Heavy Ion Collider (RHIC) at Brookhaven National Laboratory (BNL) in the United States [12]. Until an EIC is constructed, photoproduction at high energies can be studied in so-called *ultra-peripheral collisions* (UPCs) of heavy ions at the LHC or RHIC. The physics of photoproduction in UPCs will be described in this chapter in a similar manner as in the Research Project [4]. Most of the information in this chapter was taken from the review [13], unless stated otherwise.

UPCs offer a possibility to study the electromagnetic interactions between hadrons by suppressing possible hadronic interactions that would overshadow them. Since the strong force is restricted to short subnucleonic ranges ($\lesssim 1$ fm), this is ensured by colliding the hadrons at impact parameters that are larger than the sum of their radii. Hence, the interaction in UPCs has to be mediated by virtual photons emitted by the moving projectiles.

The *equivalent photon approximation* (EPA) in which the time-dependent electromagnetic field of a moving charged particle is treated as a flux of virtual photons was originally proposed by Enrico Fermi as early as 1924 [14]. In 1934, Weizsäcker and Williams provided the extension of the model to ultra-relativistic ions [14]. Because the flux of photons radiated by fast ions is proportional to the square of the proton number Z, UPCs are most often realised as symmetric collisions of heavy ions, A–A (Pb ions at the LHC, gold ions at the RHIC), or alternatively as asymmetric p–A collisions.

The photons are coherently emitted by the whole ions, whose longitudinal dimension is indeed relativistically contracted to R_a/γ_L with γ_L being the Lorentz factor. This gives the projectiles the so-called pancake shape. Employing the uncertainty principle, the longitudinal momentum of the photons can extend up to $q_\parallel \sim \gamma_L/R_a$ [14]. At HERA, where the photons were emitted by electrons and positrons, centre-of-mass energies of the γp system between 20 and 300 GeV were achieved [15]. However, the linear increase of the photon momentum with γ_L

[1] The term *inclusive* in this sense refers to the DIS reaction of the type $l + h \to l + X$, where l is a lepton probe, h is a target hadron and the product X represents each of all possible final states.

[2] E.g. distribution of partons in the transverse plane or event-by-event fluctuations of the structure.

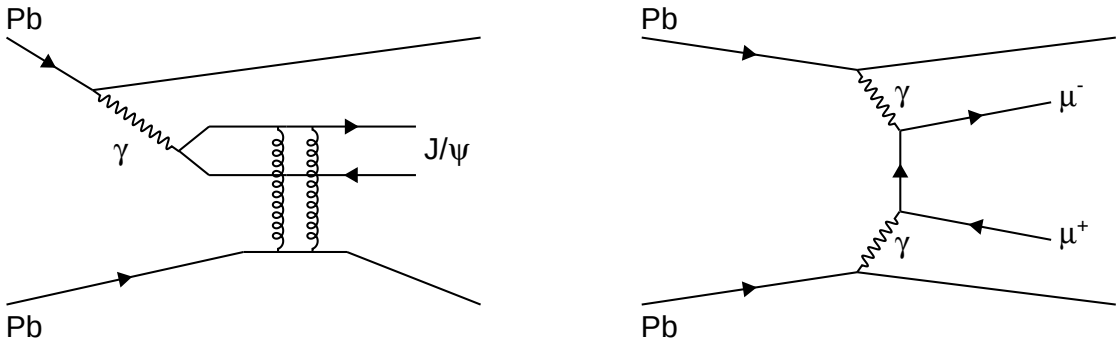

Figure 2.1: Examples of processes in ultra-peripheral Pb–Pb collisions: vector meson photoproduction (left) and production of a lepton pair in a two-photon process (right). Adapted from [13].

ensures that the maximum energies in γPb (γp) collisions at the LHC correspond to 500 (1500) GeV.

Of the relevant processes that may occur in UPCs, the most important one for this work is the *diffractive photoproduction of vector mesons*[3], where the photon emitted by one of the nuclei interacts with the second hadron or with one of its constituents via an exchange of gluons, see the left panel of Fig. 2.1. Therefore, it is referred to as a *photonuclear reaction*.

In the case of diffractive photoproduction, no net colour charge is exchanged in the strong interaction, i.e. it is realised as an exchange of the *pomeron* (a colourless state of gluons). Therefore, this type of photoproduction can be counted among the *diffractive processes*, which can be generally characterised by large gaps in the rapidity distribution of the products [16]. The exclusively photoproduced vector meson is surrounded by large rapidity gaps as it is the only product in an otherwise empty detector. Even in case that the target hadron dissociates, the vector meson is usually clearly separated from the hadronic remnants that are dominantly emitted in very forward directions [10].

Typically, the produced vector mesons have very short lifetimes and need to be reconstructed from the measured decay products. The analysis presented in Chapter 6 focuses on photoproduced J/ψ mesons, whose mean lifetime is of the order 10^{-21} s and which are usually reconstructed from the leptonic decay channels, i.e. e^+e^- or $\mu^+\mu^-$, both with the branching ratios of about 6% [17].

Instead of vector mesons, dijets can be also created in photoproduction reactions. These processes have not been studied by ALICE yet, but were analysed by the ATLAS Collaboration [10]. A considerable background in UPC events can also come from two-photon processes, such as the production of a lepton pair, see the right panel of Fig. 2.1.

2.1 Photoproduction of vector mesons

As at least two gluons are exchanged in the photoproduction of vector mesons, the cross section of such process is proportional to the square of the target gluon distribution $g(x,Q^2)$ [10]. In particular, this becomes evident in models employing the leading order perturbative QCD (LO pQCD) that will be introduced in Sec. 3.2.

[3]Vector mesons are spin-1 particles with odd P-parity and C-parity, $J^{PC} = 1^{--}$, unlike *pseudovector* mesons that have the same spin but even P-parity. Examples of vector mesons include ρ, ϕ, J/ψ and Υ.

In the photoproduction of a vector meson of the mass M_V, the target gluon density is probed at the Bjorken-x of $x = M_V^2/W^2$, where W is the centre-of-mass energy of the photon-target hadron system. Within the energies accessible at the LHC, it corresponds to the range of $10^{-5} \lesssim x \lesssim 10^{-2}$ [18], whereas at HERA, the region of $10^{-4} \lesssim x \lesssim 0.02$ was covered [15]. The low-x phenomena such as gluon shadowing in nuclear targets can be thus conveniently studied by analysing experimental data from photoproduction in UPCs.

The target partons are probed at a scale that is determined by the reaction [10]. Owing to the low virtualities of the photons in UPCs, in the photoproduction of vector mesons, the scale is set by the mass of the vector meson as $Q^2 \sim M_V^2/4$.

The following sections focus on vector meson photoproduction in ultra-peripheral Pb–Pb and p–Pb collisions as the Pb ions are used as sources of photons at the LHC.

2.1.1 Pb–Pb collisions

The cross section of the photoproduction in ultra-peripheral Pb–Pb collisions σ_{PbPb} can be factorised as the product of the virtual photon flux $N_{\gamma\mathrm{Pb}}$ and the photonuclear cross section $\sigma_{\gamma\mathrm{Pb}}$, which describes the following interaction between the emitted photon and the target nucleus. The photon flux of heavy nuclei can be computed in a semiclassical approach, which will be briefly described in Sec. 2.2. On the other hand, the photonuclear cross section has to be predicted by phenomenological models, some of which will be introduced in Chapter 3.

Using the arguments above, one can write [19]

$$\frac{\mathrm{d}\sigma_{\mathrm{PbPb}}(y)}{\mathrm{d}y} = N_{\gamma\mathrm{Pb}}(y,\{\boldsymbol{b}\})\sigma_{\gamma\mathrm{Pb}}(y) + N_{\gamma\mathrm{Pb}}(-y,\{\boldsymbol{b}\})\sigma_{\gamma\mathrm{Pb}}(-y)\,, \tag{2.1}$$

where $y = \ln(2\omega/M_V)$ is the rapidity of the vector meson in the laboratory frame, ω is the photon energy. The term $\{\boldsymbol{b}\}$ denotes the impact parameter range taken into consideration in the measurement [19]. In the rest of this thesis, all bold characters denote the transverse (two-dimensional) vectors.

The symmetry of Eq. (2.1) originates from the symmetry of Pb–Pb collisions. Both Pb ions can either serve as a source of the exchanged photon or as a target, so the eventual cross section must be taken as a superposition of both contributions. Because the rapidity of the reconstructed vector meson is defined with respect to the direction of the target nucleus [19], it can be taken as both positive or negative, depending on which Pb ion is considered a target. A sample situation is depicted in Fig. 2.2.

A direct consequence is the two-fold ambiguity in the centre-of-mass energy of the photon-ion system, $W_{\gamma\mathrm{Pb}}$. The energy is related to the rapidity y through [19]

$$W_{\gamma\mathrm{Pb}}^2 = \sqrt{s_{\mathrm{NN}}} M_V e^{-y}\,, \tag{2.2}$$

where $\sqrt{s_{\mathrm{NN}}}$ is the centre-of-mass energy per nucleon pair. Supposing that the vector meson is produced in some specific direction, then the situation where the rapidity y is negative with respect to the target hadron corresponds to that with the higher energy $W_{\gamma\mathrm{Pb}}$, see Fig. 2.2 (left). Using $x = M_V^2/W_{\gamma\mathrm{Pb}}^2$ and Eq. (2.2), this also implies that the produced vector meson probes the target hadrons at two different values of Bjorken-x, specifically

$$x_\pm = \frac{M_V}{\sqrt{s_{\mathrm{NN}}}} e^{\pm y}\,. \tag{2.3}$$

The measurements at midrapidity, $y \approx 0$, can be in this sense advantageous [20] as the ambiguity in Bjorken-x disappears as seen in Eq. (2.3).

In Pb–Pb UPCs, the photoproduction can be categorised into three types of processes:

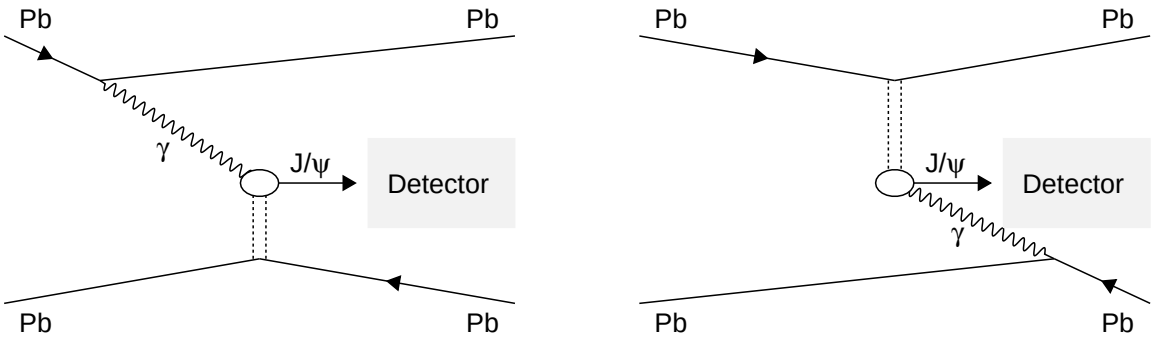

Figure 2.2: The two possible contributions for J/ψ photoproduction in UPCs at the LHC (adapted from [19]). The process on the left corresponds to that with higher centre-of-mass energy $W_{\gamma\mathrm{Pb}}$ of the photon-Pb ion system.

- *Coherent*: The photon couples to the target nucleus as a whole. This processes can be characterised by low transverse momentum of the produced vector meson, the mean value $\langle p_{\mathrm{T}} \rangle$ is around 60 MeV/c. Because the photon couples coherently to all nucleons, the nucleus does not break up.

- *Coherent with nuclear breakup*: Because the electromagnetic fields of colliding heavy nuclei are rather strong, another independent photon interaction that excites one or both of the nuclei is likely to occur. This can lead to nuclear breakup where forward neutrons are often emitted.

- *Incoherent*: The photon interacts with a single nucleon inside the target, which causes nuclear breakup. Vector mesons are produced with $\langle p_{\mathrm{T}} \rangle$ of several hundreds of MeV/c. The difference in the average p_{T} for coherent and incoherent production reflects the difference between the transverse size of a nucleus and of a nucleon [21]. Even the target nucleon can be left excited and can later dissociate, which results in even higher transverse momentum of the vector meson [20].

2.1.2 p–Pb collisions

Because of the Z^2-dependence of the photon flux, the proton contribution to the photon emission can be neglected in ultra-peripheral p–Pb collisions. The dominant contribution to the cross section thus reads

$$\frac{\mathrm{d}\sigma_{\mathrm{pPb}}(y)}{\mathrm{d}y} \approx N_{\gamma\mathrm{Pb}}(y,\{\boldsymbol{b}\})\sigma_{\gamma\mathrm{Pb}}(y)\,. \tag{2.4}$$

Introducing similar nomenclature, two types of the photoproduction off proton targets must be distinguished:

- *Exclusive*: The target proton survives the interaction and the vector meson is produced with $\langle p_{\mathrm{T}} \rangle$ around 300 MeV/c.

- *Dissociative*: The proton gets excited and subsequently dissociates. The photoproduced vector meson has $\langle p_{\mathrm{T}} \rangle$ of 1 GeV/c.

2.2 Photon flux

In the photoproduction processes, the photon virtuality is usually very low ($Q^2 \sim 0$) [10]. This is indeed satisfied in heavy-ion UPCs because in the Weizsäcker-Williams approach the photons are emitted coherently by the whole nucleus, which limits their virtuality to $Q^2 \lesssim 1/R^2$, where $R = 1.2$ fm $A^{1/3}$ is the nuclear radius and A the mass number [22]. Thus the photon can be considered almost a real particle and the expression *quasi-real* is often used [22]. On the other hand, the term *electroproduction* refers to virtual photons ($Q^2 > 0$). Electroproduction can be in principle studied in electron-ion collisions thanks to the point-like structure of the electron [10].

In the following, the spectrum $n(\omega)$ describing the number of equivalent photons of the energy ω that are coherently emitted by the nucleus with the proton number Z will be discussed. Basic properties of the spectrum will be demonstrated on a simplified example where the nuclear spin is 0, the emission is elastic and the plane wave approximation is used. In this approximation one gets [22]

$$n(\omega) = \frac{\alpha Z^2}{\pi} \int \mathrm{d}^2 q_\mathrm{T} \frac{q_\mathrm{T}^2}{\left[\left(\frac{\omega}{\gamma_L}\right)^2 + q_\mathrm{T}^2\right]^2} F_\mathrm{el}^2 \left(\left(\frac{\omega}{\gamma_L}\right)^2 + q_\mathrm{T}^2\right) , \tag{2.5}$$

where α is the fine-structure constant, q_T is the photon transverse momentum and γ_L is the Lorentz factor in the nucleus frame. $F_\mathrm{el}^2(Q^2)$ represents the elastic form factor.

Using a very rough approximation of the elastic form factor, the Heaviside step function $F_\mathrm{el}^2(Q^2) = \Theta(1/R^2 - Q^2)$, the integral in Eq. (2.5) can be solved analytically. This $F_\mathrm{el}^2(Q^2)$ shape strictly incorporates the condition of coherency because all the virtualities beyond the cut-off value of $Q^2 \sim 1/R^2$ are neglected. Integration of the photon flux then gives [22]

$$n(\omega) = \frac{2\alpha Z^2}{\pi} \ln\left(\frac{\gamma_L}{\omega R}\right) . \tag{2.6}$$

One can conclude that the approximated spectrum logarithmically decreases as $\propto \ln(1/\omega)$ and the maximum photon energy corresponds to $\omega_\mathrm{max} \approx \gamma_L/R$.

In order to acquire the energy spectrum of photons radiated by heavy ions, a semiclassical approach may be used [22]. In the following, two methods to obtain the photon flux $N_{\gamma\mathrm{Pb}}$ will be introduced.

2.2.1 Hard-sphere approximation

The first method starts with the definition of the photon flux per unit area in the impact-parameter plane in the case of E1 (electric dipole) excitations [22],

$$n(\omega, \boldsymbol{b}) = \frac{\alpha Z^2}{\pi^2 b^2} u^2 \left[K_1^2(u) + \frac{1}{\gamma_L} K_0^2(u)\right] , \tag{2.7}$$

where b is the impact parameter, $u = \omega b/\gamma_L$ and $K_0(u)$, $K_1(u)$ are the modified Bessel functions. Eq. (2.7) is then integrated starting from b_min, i.e.

$$n(\omega) = \int_{b_\mathrm{min}}^{\infty} \mathrm{d}^2\boldsymbol{b}\; n(\omega,\boldsymbol{b}) = \frac{2\alpha Z^2}{\pi} \left[\xi K_0(\xi) K_1(\xi) - \frac{\xi^2}{2}\left(K_1^2(\xi) - K_0^2(\xi)\right)\right] , \tag{2.8}$$

where $\xi = \omega b_\mathrm{min}/\gamma_L$. It can be shown that Eq. (2.8) agrees with the logarithmic approximation given by Eq. (2.6) in the limit $\xi \to 0$ [22].

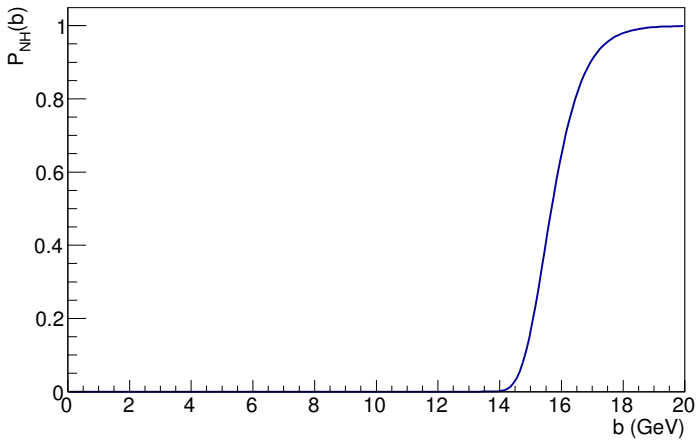

Figure 2.3: Probability of no hadronic interaction in Pb–Pb collision at the impact parameter b [19].

In the simplest picture, the nuclei can be treated as hard spheres and one may assume that hadronic interactions cannot occur if the nuclei do not overlap [23]. Then, one can set the lower limit as the sum of nuclear radii, $b_{\mathrm{min}} = 2R$, which is about 14 fm for the Pb ions. This method is referred to as the *hard-sphere approximation*. Such a treatment is accurate for heavy ions, but less suitable for lighter nuclei [23].

Eventually, the rapidity-dependent photon flux which enters Eq. (2.1) is obtained from

$$N_{\gamma\mathrm{Pb}}(y,\{\boldsymbol{b}\}) = \omega\frac{\mathrm{d}n(\omega)}{\mathrm{d}\omega}\,, \tag{2.9}$$

where proper values of Z and γ_L have to be inserted into $n(\omega)$.

2.2.2 Probability of no hadronic interaction

An alternative method was presented in [24]. Here, the probability $P_{\mathrm{NH}}(b)$ that no nucleon-nucleon interaction occurs in the collision of two nuclei at the impact parameter b is determined from a Glauber model using the Poisson distribution with the mean $T_{\mathrm{AA}}(b)\sigma_{\mathrm{NN}}$, where $T_{\mathrm{AA}}(b)$ is the nuclear overlap function and σ_{NN} is the inelastic nucleon-nucleon cross section. The $T_{\mathrm{AA}}(b)$ function was computed assuming the Woods-Saxon distribution for the nuclear density profile $\rho(b)$. For Pb ion, the calculated $P_{\mathrm{NH}}(b)$ is shown in Fig. 2.3.

Lastly, the convolution of the photon flux per unit area $n(\omega,b)$ with the probability $P_{\mathrm{NH}}(b)$ is integrated to obtain a more realistic description of the photon flux $N_{\gamma\mathrm{Pb}}$.

Chapter 3

Models for the photonuclear production of vector mesons

This chapter offers an overview of several types of models that predict the cross section of the photonuclear production of vector mesons. Where a specific process is considered, it is the J/ψ photoproduction off protons or Pb nuclei as a relevant process studied at the LHC. As pointed out in [13], the models provide three main ingredients: (i) the nuclear distribution in the transverse plane, (ii) the prescription for the wave function of the vector meson and (iii) have to relate the free parameters to the photoproduction off protons and fix their values according to fits to available data (most often from HERA).

The chapter is organised as follows: Sec. 3.1 summarises the vector meson dominance model, Sec. 3.2 briefly introduces the ideas of the models employing the leading order pQCD and starting from Sec. 3.3, the models based on the colour dipole formalism are discussed. The chapter ends with the definition of the nuclear suppression factor in Sec. 3.7.

3.1 Vector dominance model

The *vector meson dominance model* (VDM) is based on the fact that the quantum numbers of the photon J^{PC} are identical to that of vector mesons, 1^{--}, so the photon wave function can be decomposed into a sum of Fock states [14]

$$|\gamma\rangle = C_{\text{bare}}\,|\gamma_{\text{bare}}\rangle + C_\rho\,|\rho\rangle + C_\omega\,|\omega\rangle + C_\phi\,|\phi\rangle + C_{\text{J}/\psi}\,|\text{J}/\psi\rangle + \cdots + C_{q\overline{q}}\,|q\overline{q}\rangle\ , \tag{3.1}$$

where apart from the wave function of the bare photon, $|\gamma_{\text{bare}}\rangle$, the strongly interacting vector meson states into which the photon may fluctuate are considered. The bare photon amplitude is indeed $C_{\text{bare}} \approx 1$, whereas the vector meson amplitude C_V which corresponds to the probability that the photon fluctuates into the vector meson can be related to the photon-vector meson coupling f_V through $|C_V|^2 = 4\pi\alpha/f_V^2$ [14]. The leptonic decay widths, e.g. $\Gamma(V \to e^+e^-)$, may be used to estimate the values of f_V couplings for the given vector mesons [23]. However, these results have to be corrected for the non-diagonal couplings, e.g. $\langle\rho|\omega\rangle$, which are implemented in the *generalised vector meson dominance model* (GVDM).

The model by S. Klein and J. Nystrand (KN) [24] is based on the computations within the VDM and on the parametrisation of the existing data on the photoproduction of vector mesons off protons. This model is implemented in the STARlight Monte Carlo generator that can simulate photon-pomeron and two-photon interactions and is widely used in the UPC community. The rest of this section summarises the main ingredients of the KN model according to [13, 24].

First, the nuclear form factor $F(t)$ is factorised from the photonuclear cross section as

$$\sigma_{\gamma\mathrm{Pb}}(y) = \sigma(\gamma + \mathrm{Pb} \to V + \mathrm{Pb}) = \left.\frac{\mathrm{d}\sigma(\gamma + \mathrm{Pb} \to V + \mathrm{Pb})}{\mathrm{d}t}\right|_{t=0} \int_{t_{\min}}^{\infty} \mathrm{d}t \; |F(t)|^2 \,, \tag{3.2}$$

where t is the square of the four-momentum transferred in the target nucleus vertex and for narrow resonances, $t_{\min} = (M_V^2/2\omega)^2$ with M_V being the vector meson mass and ω the photon energy. Now, one can use the VDM that relates the $\gamma + \mathrm{Pb} \to V + \mathrm{Pb}$ process to $V + \mathrm{Pb} \to V + \mathrm{Pb}$ through

$$\left.\frac{\mathrm{d}\sigma(\gamma + \mathrm{Pb} \to V + \mathrm{Pb})}{\mathrm{d}t}\right|_{t=0} = \frac{4\pi\alpha}{f_V^2} \left.\frac{\mathrm{d}\sigma(V + \mathrm{Pb} \to V + \mathrm{Pb})}{\mathrm{d}t}\right|_{t=0} \tag{3.3}$$

and the optical theorem which links the previous results to the total cross section of the $V + \mathrm{Pb}$ interaction,

$$\left.\frac{\mathrm{d}\sigma(V + \mathrm{Pb} \to V + \mathrm{Pb})}{\mathrm{d}t}\right|_{t=0} = \frac{1}{16\pi}\sigma_{\mathrm{tot}}^2(V + \mathrm{Pb}) \,. \tag{3.4}$$

Afterwards, a classical Glauber model is employed to link the total cross section at the nuclear level to that at the nucleon level, $\sigma_{\mathrm{tot}}(\mathrm{p} + V)$. This reads

$$\sigma_{\mathrm{tot}}(\mathrm{Pb} + V) = \int \mathrm{d}^2\boldsymbol{b} \; \left[1 - \exp\left(-\sigma_{\mathrm{tot}}(\mathrm{p} + V) T_{\mathrm{Pb}}(\boldsymbol{b})\right)\right] \,, \tag{3.5}$$

where $T_{\mathrm{Pb}}(\boldsymbol{b})$ is the nuclear thickness function. Similarly as in Sec. 2.2.2, the expression $\exp\left[-\sigma_{\mathrm{tot}}(\mathrm{p} + V) T_{\mathrm{Pb}}(\boldsymbol{b})\right]$ denotes the probability that no interaction occurs at a considered impact parameter $\boldsymbol{b}$.

Now, the analogous procedure is followed at the nucleon level. The VDM and the optical theorem are applied in a similar way to Eq. (3.3) and (3.4), so one is eventually left with the elementary cross section for the $\gamma + \mathrm{p} \to V + \mathrm{Pb}$ process which is usually parametrised as

$$\left.\frac{\mathrm{d}\sigma(\gamma + \mathrm{p} \to V + \mathrm{p})}{\mathrm{d}t}\right|_{t=0} = b_V \left(X \cdot W_{\gamma\mathrm{p}}^{\epsilon} + Y \cdot W_{\gamma\mathrm{p}}^{-\eta}\right) \,, \tag{3.6}$$

where $W_{\gamma\mathrm{p}}$ is the centre-of-mass energy of the photon-proton system and the parameters b_V, X, Y, ϵ, η have to be determined from fits to measured data.

3.2 Leading order perturbative QCD

Considering a two-gluon exchange in QCD, one can start from Eq. (3.2) and calculate the forward scattering amplitude $\mathrm{d}\sigma/\mathrm{d}t$ at $t = 0$ perturbatively. To leading order, one gets [13, 23]

$$\left.\frac{\mathrm{d}\sigma(\gamma + \mathrm{Pb} \to V + \mathrm{Pb})}{\mathrm{d}t}\right|_{t=0} = \frac{16\pi^3\alpha_s^2\Gamma_{ee}}{3\alpha M^5} \left[x g_A\left(x, Q^2 = \frac{M^2}{4}\right)\right]^2 \,, \tag{3.7}$$

where α is the fine-structure constant and Γ_{ee} is the decay width of the vector meson into electrons (the appearance of a rather specific constant Γ_{ee} in Eq. (3.7) can be traced back to the prescription for the vector meson wave function that was considered). The coupling constant of the strong interaction $\alpha_s(Q^2)$ and the nuclear gluon distribution function $g_A(x,Q^2)$ are taken at the scale $Q^2 = M_V^2/4$ that is determined by the vector meson mass.

As mentioned earlier, the LO pQCD approach is very illustrative as it shows how the photoproduction cross section can be directly related to the gluonic content of the target. The distribution of gluons inside the nucleus can be modelled as [13]

$$g_A(x,Q^2) = R_A^g(x,Q^2) g_p(x,Q^2), \tag{3.8}$$

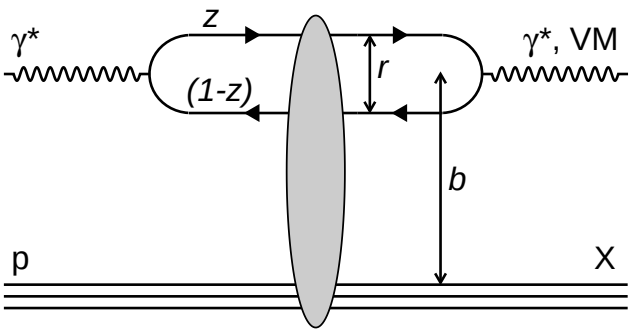

Figure 3.1: The dipole-proton scattering. The shaded area represents the exchange of gluons. Adapted from [8].

where $g_p(x,Q^2)$ is the gluon PDF for the proton and R_A^g is referred to as the *nuclear modification factor* of the gluon distribution. One can choose from several parametrisations of R_A^g incorporating the nuclear effects, for example EPS08, EPS09 and HKN07 are widely used [13].

3.3 Colour dipole approach

In the dipole picture, it is assumed that (i) an incident photon fluctuates into a quark-antiquark pair (into a colour dipole), (ii) the dipole then interacts with the nuclear/hadronic target with the cross section σ_{dip} via an exchange of the pomeron and (iii) a vector meson is eventually formed from a colour dipole [13]. This process is depicted in Fig. 3.1. It is further assumed that long time periods pass between these three events, which means that the dipole lifetime is long enough that its configuration can be considered unchanged during the time it spends in the nucleus [10].

In the dipole formalism, the photonuclear cross section is constructed from the imaginary part of the scattering amplitude [21]

$$A^j(x,Q^2,\boldsymbol{\Delta})_{T,L} = i \int \mathrm{d}^2\boldsymbol{r}\ \mathrm{d}^2\boldsymbol{b} \int_0^1 \frac{\mathrm{d}z}{4\pi}\ [\Psi^*\Psi_V]_{T,L}\ e^{-i(\boldsymbol{b}-(1-z)\boldsymbol{r})\cdot\boldsymbol{\Delta}} \left(\frac{\mathrm{d}\sigma_{\text{dip}}}{\mathrm{d}^2\boldsymbol{b}}\right)^j , \tag{3.9}$$

where

- $\boldsymbol{r}$ is the dipole size (the transverse separation between the quark and the antiquark),
- $\boldsymbol{b}$ is the impact parameter (the distance between the centre of the target and of the dipole),
- z denotes the fraction of the photon momentum that is carried by the quark,
- $\boldsymbol{\Delta}$ is the transverse momentum transferred in the nuclear vertex between the nuclei, $\boldsymbol{\Delta}^2 = -t$,
- Ψ is the wave function of the photon splitting into the $q\overline{q}$ dipole, Ψ_V is the vector meson wave function and
- the subscripts T, L correspond to contributions from transversely and longitudinally polarised photons.

The superscript j in Eq. (3.9) denotes the specific geometrical configuration of the nuclear substructure. The sensitivity to target configurations is further incorporated in the dipole cross section σ_{dip}. In a Good-Walker approach, it can be shown that the cross section for the coherent photonuclear production is proportional to the square of the amplitude averaged over possible target configurations [21]

$$\left.\frac{\mathrm{d}\sigma_{\gamma\mathrm{Pb}}}{\mathrm{d}t}\right|_{T,L}^{\mathrm{coh}} = \frac{(R_g^{T,L})^2}{16\pi}\left|\left\langle A(x,Q^2,\boldsymbol{\Delta})_{T,L}\right\rangle_j\right|^2 , \tag{3.10}$$

where

$$R_g^{T,L}(\lambda_g^{T,L}) = \frac{2^{2\lambda_g^{T,L}+3}}{\sqrt{\pi}}\frac{\Gamma(\lambda_g^{T,L}+5/2)}{\Gamma(\lambda_g^{T,L}+4)} \tag{3.11}$$

with

$$\lambda_g^{T,L} = \frac{\partial \ln(A_{T,L})}{\partial \ln(1/x)} \tag{3.12}$$

is the so-called *skewedness correction* [13, 21] which compensates for the fact that an "average" value of Bjorken-x is used in the calculation even though the two gluons exchanged between the dipole and the target (see the left panel of Fig. 2.1) are assigned different values of Bjorken-x.

In order to obtain pictures of the transverse density profile of the target structure, the t-dependence of the coherent photonuclear cross section has to be measured, $\mathrm{d}\sigma_{\gamma\mathrm{Pb}}^{\mathrm{coh}}/\mathrm{d}t$. As the transverse momentum transfer is the Fourier conjugate to the impact parameter, the transverse distribution of interaction sites inside the nucleus, $F(b)$, can be computed as the Fourier transform of $\mathrm{d}\sigma_{\gamma\mathrm{Pb}}^{\mathrm{coh}}/\mathrm{d}t$ [10]. Recently, the t-dependence of the coherent cross section was measured for the first time by ALICE [25]. This measurement will be summarised in Sec. 5.4.

On the other hand, the incoherent photonuclear cross section in a Good-Walker formalism is given as a variance over target configurations [21],

$$\left.\frac{\mathrm{d}\sigma_{\gamma\mathrm{Pb}}}{\mathrm{d}t}\right|_{T,L}^{\mathrm{inc}} = \frac{(R_g^{T,L})^2}{16\pi}\left[\left\langle\left|A(x,Q^2,\boldsymbol{\Delta})_{T,L}\right|^2\right\rangle_j - \left|\left\langle A(x,Q^2,\boldsymbol{\Delta})_{T,L}\right\rangle_j\right|^2\right] . \tag{3.13}$$

The switched ordering between the averaging and squaring of the amplitude ensures that the incoherent processes are sensitive to *event-by-events fluctuations* of the transverse nuclear structure [10]. There are multiple sources of inner fluctuations: the positions of nucleons inside the target can fluctuate as well as the partonic substructure of individual nucleons. During the interaction with the colour dipole, the nuclear configuration can be considered unvarying ("frozen") thanks to time dilation, which is a consequence of the high energy of the process [10]. Because the nucleus gets excited in the incoherent photoproduction, at least some energy must be transferred in the nuclear vertex, so the incoherent cross section is expected to vanish when approaching $t \to 0$ [10].

One may also introduce the correction $1+\beta^2$ with $\beta = \tan\left(\pi\lambda_g^{T,L}/2\right)$ into Eq. (3.10) and (3.13) to account for the real part of the scattering amplitude [26].

3.4 Model by T. Lappi and H. Mäntysaari

In this section, the colour dipole-based model for the J/ψ photoproduction developed by T. Lappi and H. Mäntysaari (LM) is introduced. The detailed description of the formalism can be found in [26] (focusing on the incoherent process), the predictions for both the coherent and incoherent photoproduction at the LHC energies (especially for the energy of $\sqrt{s_{\mathrm{NN}}} = 2.76$ TeV) were later

presented in [27]. The models were developed without using any nuclear data to constrain the parameters.

Considering that the colour dipole formalism is valid only in the high-energy limit when the gluon Bjorken-x is sufficiently low, the authors performed the calculations for $x < 0.02$. The transition from the proton targets to nuclear photoproduction was realised via a Glauber-like independent scattering approximation, where the nuclear S-matrix is written as a product

$$S_A(\boldsymbol{r},\boldsymbol{b},x) = \prod_{i=1}^{A} S_p(\boldsymbol{r},\boldsymbol{b}-\boldsymbol{b}_i,x)\,, \tag{3.14}$$

where, recalling the standard notation, $\boldsymbol{r}$ is the dipole size in the transverse plane, $\boldsymbol{b}$ is the impact parameter and $\boldsymbol{b}_i$ are the positions of nucleons in the transverse plane.

Applying the optical theorem, one can relate the colour dipole-proton cross section to the imaginary part of the forward dipole-target amplitude $\mathcal{N}(\boldsymbol{r},\boldsymbol{b},x)$ [15],

$$\frac{\mathrm{d}\sigma^{\mathrm{p}}_{\mathrm{dip}}}{\mathrm{d}^2\boldsymbol{b}}(\boldsymbol{r},\boldsymbol{b},x) = 2\mathcal{N}(\boldsymbol{r},\boldsymbol{b},x)\,. \tag{3.15}$$

Ideally, since the forward amplitude satisfies the small-x BK equation, one would like to use the data from DIS experiments to fit the initial conditions and then to compute the evolution using the BK equation to obtain the amplitude $\mathcal{N}(\boldsymbol{r},\boldsymbol{b},x)$ that may be used in the photoproduction of vector mesons. However, it is crucial to know the precise b-dependence of the forward amplitude in order to compute the evolution and the attempts to solve this problem often led to unphysical results[1]. Hence, the authors decided to use two phenomenological parametrisations of the forward amplitude instead, (i) the *IIM* and (ii) the *IPsat* models.

The IIM model includes the parametrisation according to the expected behaviour of the solution to the BK equation [13]. The parameters are determined according to fits to HERA data. The $\boldsymbol{r}$ and $\boldsymbol{b}$ dependence of the dipole cross section is directly factorised as

$$\frac{\mathrm{d}\sigma^{\mathrm{p}}_{\mathrm{dip}}}{\mathrm{d}^2\boldsymbol{b}}(\boldsymbol{r},\boldsymbol{b},x) = 2T_p(\boldsymbol{b})\mathcal{N}(\boldsymbol{r},x)\,, \tag{3.16}$$

where T_p is the transverse profile of the proton for which a Gaussian is used, $T_p(\boldsymbol{b}) = \exp\left(-b^2/2B_p\right)$ with the parameter $B_p = 5.59\ \mathrm{GeV}^{-2}$.

The IPsat model, on the other hand, considers the saturation scale defined as $Q_s(x,r) = F(x,r)T_p(\boldsymbol{b})$, so the dipole cross section becomes

$$\frac{\mathrm{d}\sigma^{\mathrm{p}}_{\mathrm{dip}}}{\mathrm{d}^2\boldsymbol{b}}(\boldsymbol{r},\boldsymbol{b},x) = 2\left[1-\exp\left(-r^2F(x,r)T_p(\boldsymbol{b})\right)\right]\,, \tag{3.17}$$

where T_p is again a Gaussian profile with $B_p = 4.0\ \mathrm{GeV}^{-2}$ and the F function is proportional to the eikonalised gluon distribution function $g(x,Q^2)$ evolved with the DGLAP equation, i.e.

$$F(x,r) = \frac{1}{2\pi B_p}\frac{\pi^2}{2N_c}\alpha_s(\mu^2)\ xg(x,\mu^2)\,, \tag{3.18}$$

where $\mu^2 = \mu_0^2 + 4/\boldsymbol{r}^2$ and $\mu_0^2 = 1.17\ \mathrm{GeV}^2$ is extracted from a fit to data. In order to notably simplify the computational requirements, Eq. (3.17) was also factorised as

$$\frac{\mathrm{d}\sigma^{\mathrm{p}}_{\mathrm{dip}}}{\mathrm{d}^2\boldsymbol{b}}(\boldsymbol{r},\boldsymbol{b},x) \approx 2T_p(\boldsymbol{b})\left[1-\exp\left(-r^2F(x,r)\right)\right]\,. \tag{3.19}$$

[1] These problems have been recently overcome. See [28, 29].

This approximation is denoted as *fIPsat* and is similar to the IIM parametrisation with the specific choice of $\mathcal{N}(\boldsymbol{r},x)$.

In the next step, the coherent and incoherent cross sections were calculated using Eq. (3.10) and (3.13), taking into account the $1+\beta^2$ correction as well. The average over the positions of the nucleons was calculated via

$$\langle \mathcal{O} \rangle_j = \int \prod_{i=1}^{A} \left[\mathrm{d}^2\boldsymbol{b}_i \; T_A(\boldsymbol{b}_i) \right] \mathcal{O}(\{\boldsymbol{b}_i\}) \,, \tag{3.20}$$

where $\mathcal{O}(\{\boldsymbol{b}_i\})$ represents a general function that depends on the transverse positions of nucleons and T_A is the Woods-Saxon distribution of the nuclear target.

To obtain the coherent cross section, one has to calculate the average of the amplitude A given by Eq. (3.9), which for the large and smooth nucleus becomes

$$\begin{aligned} \left\langle A(x,Q^2,\boldsymbol{\Delta}) \right\rangle_j = \int \frac{\mathrm{d}z}{4\pi} \; \mathrm{d}^2\boldsymbol{r} \; \mathrm{d}^2\boldsymbol{b} \; e^{-i\boldsymbol{b}\cdot\boldsymbol{\Delta}} \left[\Psi^*\Psi_V\right](r,Q^2,z) \\ \times 2\left[1 - \exp\left(-2\pi B_p A T_A(b) \mathcal{N}(r,x)\right)\right] \,, \end{aligned} \tag{3.21}$$

where the "Boosted-Gaussian" and "Gauss-LC" prescriptions were used for the vector meson wave functions.

For the incoherent cross section, the average of the squared amplitudes has to be determined first, i.e.

$$\begin{aligned} \left\langle |A(x,Q^2,\boldsymbol{\Delta})|^2 \right\rangle_j = \int \frac{\mathrm{d}z}{4\pi} \frac{\mathrm{d}z'}{4\pi} \; \mathrm{d}^2\boldsymbol{r} \; \mathrm{d}^2\boldsymbol{r}' \; \left[\Psi^*\Psi_V\right](r,Q^2,z) \; \left[\Psi^*\Psi_V\right](r',Q^2,z') \\ \times \left\langle |A_{q\bar{q}}(x,r,r',\boldsymbol{\Delta})|^2 \right\rangle_j \,, \end{aligned} \tag{3.22}$$

where the remaining part of the amplitude can be, after some simplifications (see [26]), expressed as

$$\begin{aligned} |A_{q\bar{q}}(x,r,r',\boldsymbol{\Delta})|^2 = 16\pi B_p A \int \mathrm{d}^2\boldsymbol{b} \; e^{-B_p\boldsymbol{\Delta}^2} \; e^{-2\pi B_p A T_A(b)[\mathcal{N}(r)+\mathcal{N}(r')]} \\ \times \left(\frac{\pi B_p \mathcal{N}(r)\mathcal{N}(r') T_A(b)}{1 - 2\pi B_p T_A(b)[\mathcal{N}(r)+\mathcal{N}(r')]} \right) \,. \end{aligned} \tag{3.23}$$

The incoherent cross section is eventually obtained subtracting the coherent cross section from Eq. (3.22) and adding the necessary corrections and the numerical factor $\frac{1}{16\pi}$.

3.4.1 Results

The authors state that the model should be most reliable at midrapidity $y \approx 0$ where the two contributions with different values of Bjorken-x given by Eq. (2.3) do not differ as much as in the forward direction.

Figure 3.2 shows the predictions of the LM model for the rapidity dependence of the J/ψ photoproduction cross sections at $\sqrt{s_{\mathrm{NN}}} = 2.76$ TeV. A comparison of the coherent cross section with the first ALICE measurements based on data from Run 1 of the LHC is made. Although both parametrisations overestimate the measured data, the fIPsat model with the Gauss-LC form of the wave function seem to give the most reliable predictions.

This might be a consequence of the fact that the data from HERA on the diffractive J/ψ photoproduction off protons are consistent with a smaller width of the Gaussian density

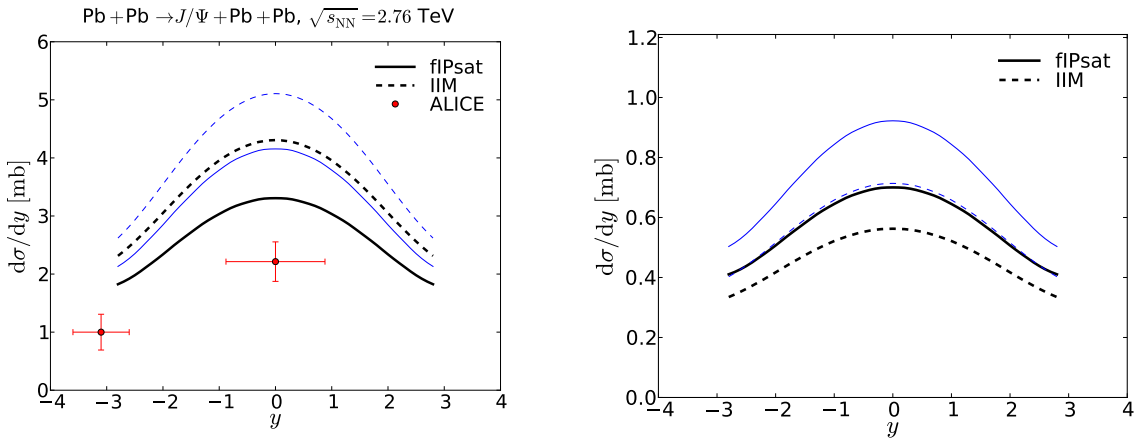

Figure 3.2: The predicted rapidity dependence of the coherent (left) and incoherent (right) J/ψ photoproduction cross section in Pb–Pb collisions at $\sqrt{s_{\mathrm{NN}}} = 2.76$ TeV [27]. The computations with the Boosted-Gaussian (thin blue lines) and Gauss-LC (thick black lines) wave functions are distinguished. In the coherent case, a comparison is made with the Run 1 ALICE measurements [30, 31].

distribution, $B_p = 4.0\ \mathrm{GeV}^{-2}$, which is incorporated in the IPsat model. The IIM parametrisation, on the contrary, is based on a fit to data for inclusive diffraction, which gives a somewhat larger width of $B_p = 5.59\ \mathrm{GeV}^{-2}$.

Figure 3.2 also suggests that the different parametrisations of the wave functions modify mostly the overall normalisation, while the y-dependence is barely affected.

The t-dependence of the predicted cross sections at midrapidity and $\sqrt{s_{\mathrm{NN}}} = 2.76$ TeV (corresponds to $x \approx 10^{-3}$) is depicted in Fig. 3.3. The diffractive minima are a characteristic feature of the t-dependent coherent cross section.

3.5 Probing subnucleonic fluctuations

The importance of taking fluctuations of the proton shape into account was demonstrated on the exclusive and dissociative photoproduction of vector mesons off protons in [32]. A summary of key points can be found in the Research Project [4]. In this section, the extension of the original ideas to the coherent and incoherent J/ψ photoproduction off nuclear targets [33] will be discussed.

The authors employed the dipole framework including saturation effects similarly to the former LM model [26, 27]. The dipole cross section was related to the forward amplitude through Eq. (3.15) and the IPsat parametrisation given by Eq. (3.17) with a DGLAP-evolved gluon distribution (Eq. (3.18)) and impact-parameter-dependent saturation scale was employed. The authors made improvements with respect to their previous calculations in [27] consisting of the Monte Carlo method to calculate the target averages, thanks to which it was not necessary to take the factorised form of the model (fIPsat, see Eq. (3.19)).

The modification introducing geometric fluctuations on the subnucleonic scale was inserted into the model by replacing the ordinary nucleon Gaussian profile $T_p(\boldsymbol{b})$ with the sum of three Gaussian-shaped centres,

$$T_p(\boldsymbol{b}) \to \sum_{i=1}^{3} T_q(\boldsymbol{b} - \boldsymbol{b}_{q,i}) \quad \text{with} \quad T_q(\boldsymbol{b}) = \frac{1}{2\pi B_q} \exp\left(\frac{-\boldsymbol{b}^2}{2B_q}\right), \tag{3.24}$$

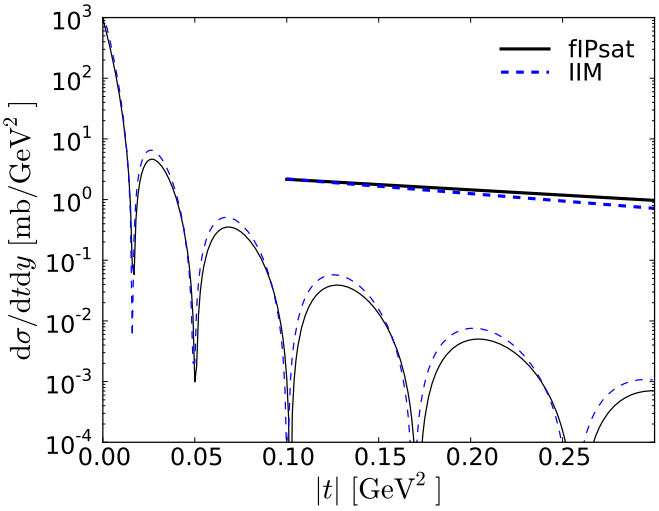

Figure 3.3: The predicted t-dependence of the coherent (thin) and incoherent (thick) cross section of the J/ψ photoproduction in Pb–Pb collisions at $\sqrt{s_{\mathrm{NN}}} = 2.76$ TeV [27]. The calculation was performed at midrapidity $y = 0$ and the Gauss-LC prescription was used for the wave function.

which represent valence quarks and are also called *hot spots*. The positions of hot spots $\boldsymbol{b}_{q,i}$ are sampled from a 2D Gaussian distribution with the width of $B_{qc} = 3.3$ GeV^{-2}. This value, as well as the width of individual hot spots $B_q = 0.7$ GeV^{-2}, were obtained from a fit to HERA data on diffractive J/ψ photoproduction.

The authors also considered a second independent source of fluctuations, which are event-by-event fluctuations of the overall normalisation of the saturation scale $Q_s(x,r) = F(x,r)T_p(\boldsymbol{b})$. This effect can be described by a log-normal distribution, for the details refer to [32].

Lastly, to obtain the nuclear forward amplitude $\mathcal{N}_A$, an independent scattering approximation as in Eq. (3.14) was used, i.e.

$$\mathcal{N}_A(\boldsymbol{r},\boldsymbol{b},x) = 1 - \prod_{i=1}^{A} \left[1 - \mathcal{N}(\boldsymbol{r},\boldsymbol{b} - \boldsymbol{b}_i,x)\right] , \tag{3.25}$$

where $\boldsymbol{b}_i$ are the positions of nucleons and the product on the right side can be interpreted as the probability that the scattering off any of the nucleons does not occur. The rest of the calculation towards the coherent and incoherent cross section proceeds in a full analogy with the technique described in Sec. 3.4. Again, both the Boosted Gaussian and Gauss-LC parametrisations of the vector meson wavefunction were used.

3.5.1 Results

The result that is least affected by the uncertainties related to the parametrisation of the vector meson wave function is the ratio of the incoherent to coherent cross section, where these are mostly cancelled out. The predictions for the energy of $\sqrt{s_{\mathrm{NN}}} = 2.76$ TeV in comparison with the ALICE results [31] can be found in Fig. 3.4. The ratio shows a negligible y-dependence. The inclusion of fluctuations leads to the increase of the ratio by a factor of two, as a result of which the prediction based on the Gauss-LC parametrisation agrees with the ALICE result within the uncertainties.

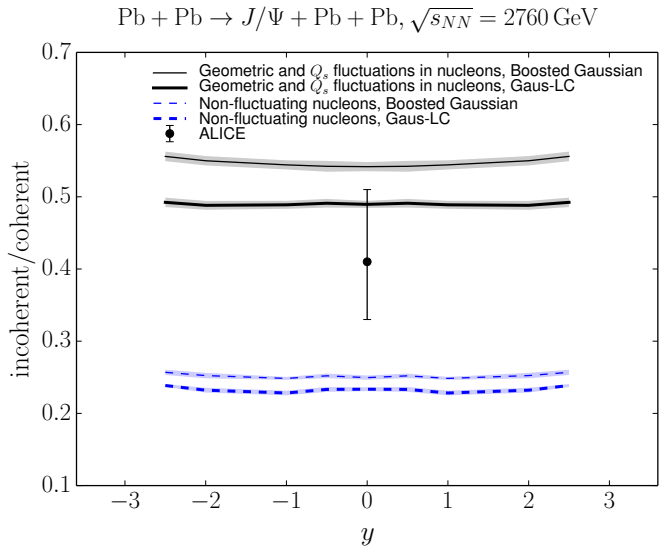

Figure 3.4: The ratio of the incoherent to coherent cross section of the J/ψ photoproduction at $\sqrt{s_{\rm NN}} = 2.76$ TeV [33] in comparison with ALICE results [31].

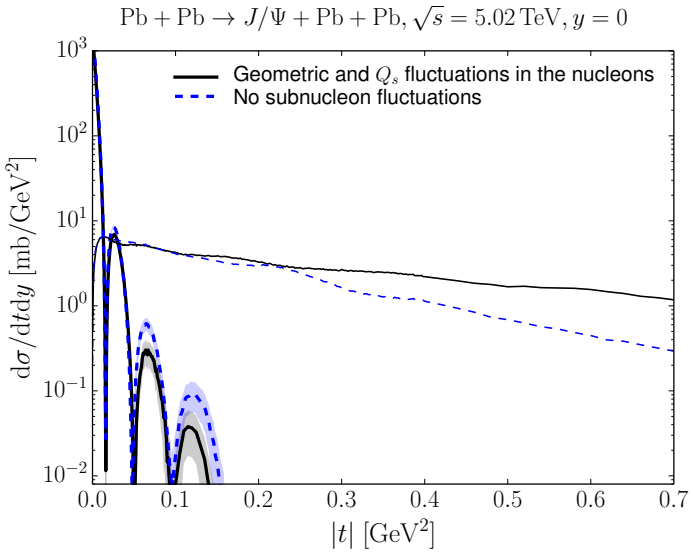

Figure 3.5: Coherent (thick) and incoherent (thin lines) J/ψ photoproduction cross section as a function of t with (solid) and without (dashed lines) subnucleonic fluctuations [33]. The Boosted Gaussian wave function was used. Only the first three diffractive peaks of the coherent cross section are shown.

In Fig. 3.5, one can find the calculated t-dependence of the coherent and incoherent J/ψ photoproduction cross sections in Pb–Pb collisions at $y = 0$ and $\sqrt{s_{\rm NN}} = 5.02$ TeV with and without the inclusion of subnucleonic geometric and saturation scale fluctuations. As a consequence of fluctuations, the incoherent cross section is substantially enhanced in the high-$|t|$ region, $|t| \gtrsim 0.25$ GeV^2.

The predictions for the rapidity dependences of the photoproduction cross sections at the energy of $\sqrt{s_{\rm NN}} = 5.02$ TeV that are relevant for the analysis presented in Chapter 6 are depicted in Fig. 3.6. One may notice that fluctuations of the nucleon structure have the opposite effect on

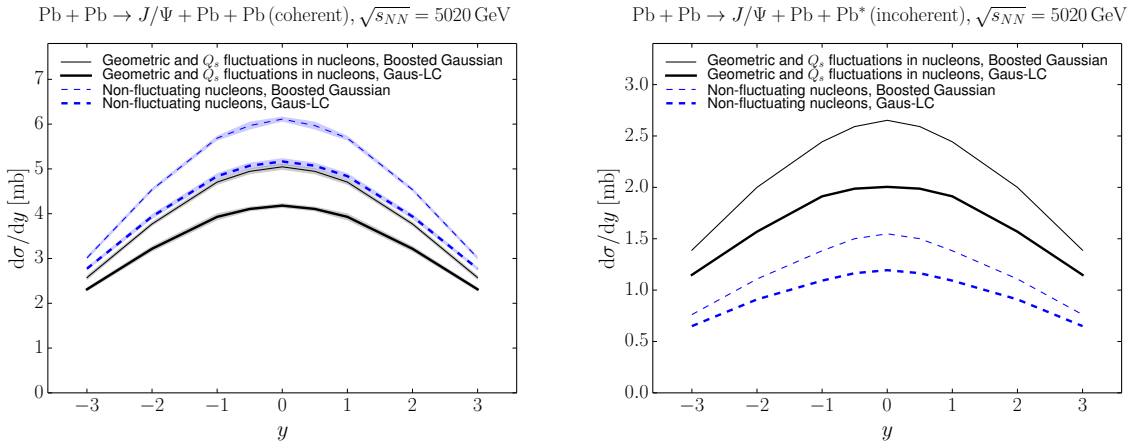

Figure 3.6: Rapidity dependence of the coherent (left) and incoherent (right) J/ψ photoproduction cross sections predicted for the energy of $\sqrt{s_{\mathrm{NN}}} = 5.02$ TeV [33].

the two cross sections. At $y \approx 0$, fluctuations cause a reduction of the coherent cross section of about 25%.

3.6 Energy-dependent hot-spot model

The concept of *hot spots*, around which the gluonic content of nucleons is concentrated in the transverse plane, was further extended by J. Cepila et al. in [15, 21], where the energy evolution was introduced by making the number of hot spots increasing with decreasing Bjorken-x. This reflects the previous observation in Fig. 1.3 that the number of partons that can participate in the process grows towards low Bjorken-x.

In [15], the formalism was applied to the exclusive and dissociative J/ψ photoproduction off protons to show that at higher energies the transverse distribution becomes smoother and possible target configurations start to resemble each other, which leads to a decrease in the variance in Eq. (3.17). Eventually, this manifests itself in the saturation of the dissociative cross section near the centre-of-mass energy of the photon-proton system of $W_{\gamma\mathrm{p}} \approx 500$ GeV that is followed by a steep decrease. Being within the energy range that is accessible at the LHC, the authors thus proposed that the observation of the phenomenon might provide an experimental signature of the gluon saturation.

In [21], the application of the formalism to the coherent and incoherent photoproduction of J/ψ was introduced. The detailed discussion of both papers [15, 21] has been already presented in the Research Project [4]. In the rest of this section, only the predictions from [21] that are crucial for the analysis described in Chapter 6 will be shown.

Two approaches were followed to obtain the dipole-nucleus cross section, namely the standard Glauber-Gribov (GG) formalism and geometric scaling (GS), see [21] for the details. The nuclear profile function $T_A(\boldsymbol{b})$ was either taken as a sum of A Gaussian-shaped nucleons (denoted by the ending -n in the figures) distributed randomly at the positions $\boldsymbol{b}_i$ sampled from a Woods-Saxon nuclear density profile (for each j-th configuration) or the subnucleonic degrees of freedom were included by decomposing the nucleons into a sum of Gaussian-shape hot spots (denoted by -hs) that were distributed according to a Gaussian distribution of a width B_{hs}.

The number of hot spots was calculated from a Poisson distribution with the mean of $\langle N_{hs}(x)\rangle = p_0 x^{p_1}(1 + p_2\sqrt{x})$ with $p_0 = 0.011$, $p_1 = -0.58$ and $p_2 = 250$ [15].

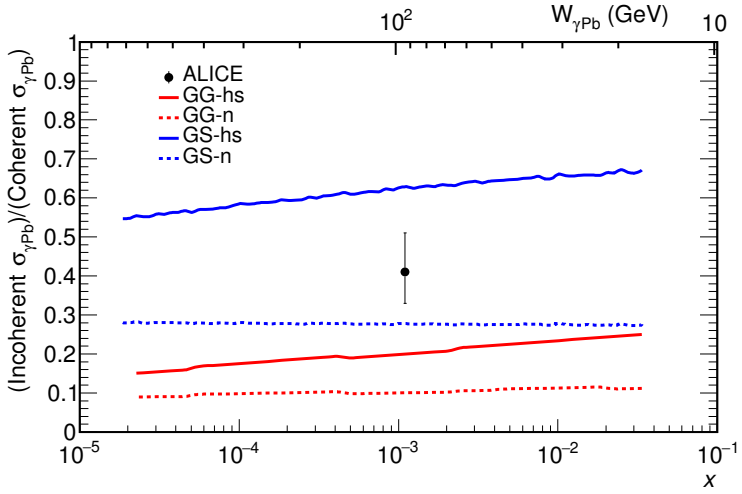

Figure 3.7: The modelled x-dependence of the ratio of the incoherent to coherent J/ψ photonuclear cross sections [21] in comparison with the measurement by ALICE [31].

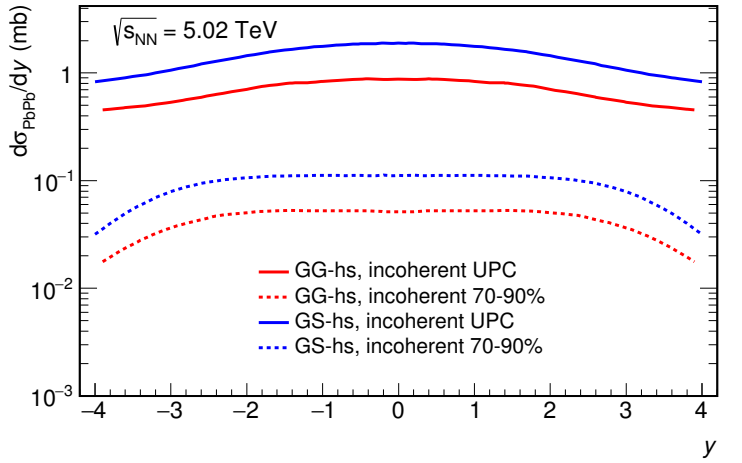

Figure 3.8: The rapidity dependence of the incoherent J/ψ photoproduction cross section in peripheral and ultra-peripheral Pb–Pb collisions at $\sqrt{s_{\mathrm{NN}}} = 5.02$ TeV predicted in [21].

3.6.1 Results

The virtuality of the quasi-real photon was taken as $Q^2 = 0.05$ GeV^2 and the vector meson wave function was described by the Boosted-Gaussian parametrisation.

Within the followed formalism, it turns out that the energy dependence of the number of hot spots introduces an x-dependence of the ratio of the incoherent to coherent J/ψ photonuclear cross section, which is shown in Fig. 3.7. The comparison with the ALICE result [31] corresponding to $x \approx 10^{-3}$ in combination with the PHENIX measurements ($x \approx 0.015$, not shown in the figure) suggests that the ratio might be indeed x-dependent. One of the objectives of the analysis in Chapter 6 is thus to provide a new measurement in the quest to further support or to refute the assumption of the x-dependence of the ratio.

The predictions of the y-dependence of the incoherent J/ψ photoproduction cross section in Pb–Pb collisions at the energy $\sqrt{s_{\mathrm{NN}}} = 5.02$ TeV can be seen in Fig. 3.8. Comparison of

the modelled y-dependence of the coherent and incoherent cross sections at $\sqrt{s_{\mathrm{NN}}} = 2.76$ TeV with the ALICE and CMS results (not shown in this work, see [21]) clearly spoke in favour of the inclusion of fluctuations as without them the measurements were strongly underestimated. Concerning the two approaches extending the formalism to the nuclear case, the GS matched the data quite well while the GG predictions were slightly above the experimental results.

3.7 Nuclear suppression factor

Now that the various approaches to model the photonuclear cross section have been discussed, one may get back to the discussion of the nuclear shadowing. In order to evaluate the effects of the nuclear shadowing based on the experimentally measured cross section of the coherent photoproduction, the *nuclear suppression factor* is defined as [34, 19]

$$S_{\mathrm{Pb}}(W_{\gamma\mathrm{Pb}}) = \left(\frac{\sigma^{\mathrm{data}}_{\gamma\mathrm{Pb}}(W_{\gamma\mathrm{Pb}})}{\sigma^{\mathrm{IA}}_{\gamma\mathrm{Pb}}(W_{\gamma\mathrm{Pb}})} \right)^{1/2} , \tag{3.26}$$

where in the nominator one inserts the measured photonuclear cross section and in the denominator the so-called *impulse approximation* (IA) is used [34, 19],

$$\sigma^{\mathrm{IA}}_{\gamma\mathrm{Pb}}(W_{\gamma\mathrm{Pb}}) = \left. \frac{\mathrm{d}\sigma_{\gamma\mathrm{p}}(W_{\gamma\mathrm{p}} = W_{\gamma\mathrm{Pb}})}{\mathrm{d}t} \right|_{t=0} \int_{t_{\mathrm{min}}}^{\infty} \mathrm{d}t \; |F(t)|^2 \, , \tag{3.27}$$

where the photonuclear cross section is directly related to the forward scattering amplitude of $\gamma + p \to \mathrm{J}/\psi + p$ (which can be extracted from a fit to experimental data) through the square of the nuclear form factor $F(t)$. $W_{\gamma\mathrm{p}}$ is the centre-of-mass energy of the photon-proton system and t_{min} is determined from the minimal longitudinal momentum transfer [34].

In the IA, all nuclear effects except for coherence are neglected [34]. The square root in the definition of S_{Pb} is motivated by the fact that the coherent cross section in the LO pQCD formalism is protoportional to the square of target gluon density [25]. The S_{Pb} factor should be equal to one when the nuclear effects are negligible and $S_{\mathrm{Pb}} < 1$ when a suppression is observed [19].

Chapter 4

ALICE at the LHC

4.1 The LHC

The experimental data analysed in this thesis were collected at the Large Hadron Collider (LHC) [35], which is situated at the European Organization for Nuclear Research (CERN) near Geneva. The LHC is installed in a tunnel with a circumference of 26.7 km at a depth of 45-170 m below the surface. It constitutes the last stage of the CERN accelerator chain and was mainly designed to collide protons at the centre-of-mass energy of 14 TeV and a luminosity reaching 10^{34} cm^{-2}s^{-1}. For fully stripped lead ions $^{208}Pb^{82+}$ the design parameters contemplated a centre-of-mass energy of 5.5 TeV per nucleon pair and a luminosity of 10^{27} cm^{-2}s^{-1}. This makes the LHC the most powerful particle accelerator ever built.

The LHC is a two-ring hadron synchrotron, where the magnetic and electric fields are synchronised with the kinetic energy of the particles being accelerated. At the LHC, the protons or heavy ions circulate in two counter-rotating beams that are held inside toroidal vacuum pipes. The trajectories of the particles are bent by superconducting electromagnets with a peak dipole field reaching 8.33 T for the maximum proton energy of 7 TeV. Particles are injected into the LHC from the Super Proton Synchrotron (SPS), having been already accelerated to 450 GeV (protons) or 177 GeV per nucleon (Pb ions) [35].

The layout of the LHC machine is shown in Fig. 4.1. In fact, the LHC tunnel is not a perfect circle, it is segmented into eight arcs and eight long straight sections, in the middle of which the Interaction Points (IP) 1-8 are located. Once per each revolution, the particles are accelerated by a longitudinal oscillating electric field of a frequency of 400.8 MHz in radio-frequency (RF) cavities that are located at IP 4. In order to maintain the synchronisation between the frequency of revolution and the electric field frequency, the particles must be grouped into so-called bunches containing $\approx 1.2 \times 10^{11}$ protons or $\approx 7.0 \times 10^{7}$ heavy ions [35]. In each beam, there are 3564 available bunch positions separated by time intervals of 25 ns. Up to 2808 proton bunches or 592 heavy ion bunches can be accelerated simultaneously.

The construction of the LHC tunnel was carried out as early as 1984-1989 because it was originally designed for the Large Electron-Positron Collider (LEP) which was successfully operated between the years 1989 and 2000, after which it was dismantled to make way for the LHC. The construction of the LHC was finished in 2008 and the proton beams were first injected on the 10th of September of the same year. The first operational run, called Run 1, took place between 2009 and 2013. During Run 1, the contemporary world record on the centre-of-mass energy in proton-proton collisions was set to 8 TeV.

Following Long Shutdown (LS) 1, the next data-taking period (Run 2) was conducted from 2015 to 2018 with the maximum achieved centre-of-mass energies of 13 and 5.02 TeV in

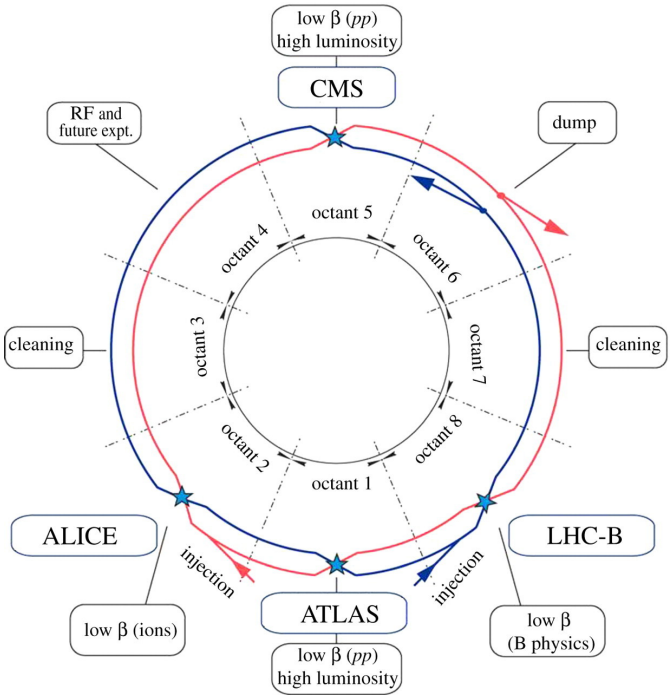

Figure 4.1: The LHC machine layout [36].

proton-proton and Pb–Pb collisions, respectively. In October 2017 it was tested that even the fully stripped xenon ions $^{129}Xe^{54+}$ can be collided at the LHC [37]. Since December 2018, the LHC undergoes LS 2 that is scheduled to end in 2021. During this time, major upgrades are being performed on the LHC and its detectors. These are crucial for the implementation of the High Luminosity LHC project in 2027 which aims at increasing the luminosity by a factor of 10 to 10^{35} cm^{-2}s^{-1}.

There are four main experiments operating at the LHC, as can be seen in Fig. 4.1. Two of them, ALICE at IP 2 and LHCb at IP 8, were installed to the underground caverns that had been previously occupied by the LEP experiments [36]. However, new caverns with sufficient dimensions had to be constructed for the ATLAS and CMS experiments at IP 1 and IP 5.

4.2 ALICE

A Large Ion Collider Experiment (ALICE) is a general-purpose detector system optimised to measure heavy-ion collisions. The purpose of ALICE is to study strongly interacting matter and to explore the properties of the quark-gluon plasma (QGP). The information about the ALICE detectors presented in the following sections was taken from [38], unless stated otherwise.

The layout of ALICE during Run 2 is depicted in Fig. 4.2. The ALICE apparatus is located in a cavern of $26 \times 16 \times 16$ m^3, which lies 56 m beneath the ground and where the L3 experiment at LEP was placed before. Most of the ALICE detectors are embedded in a huge solenoid magnet with an octagonal cross section and a magnetic flux density reaching 0.5 T, which was reused from the L3 experiment. The detectors placed inside the solenoid are called the central-barrel detectors and most of them cover the pseudorapidity range of $|\eta| < 0.9$. ALICE is also equipped with the forward muon spectrometer shown in the right part of Fig. 4.2, which covers the pseudorapidity interval of $-4.0 < \eta < -2.5$.

The inner part of the central barrel is occupied by four detectors that have cylindrical

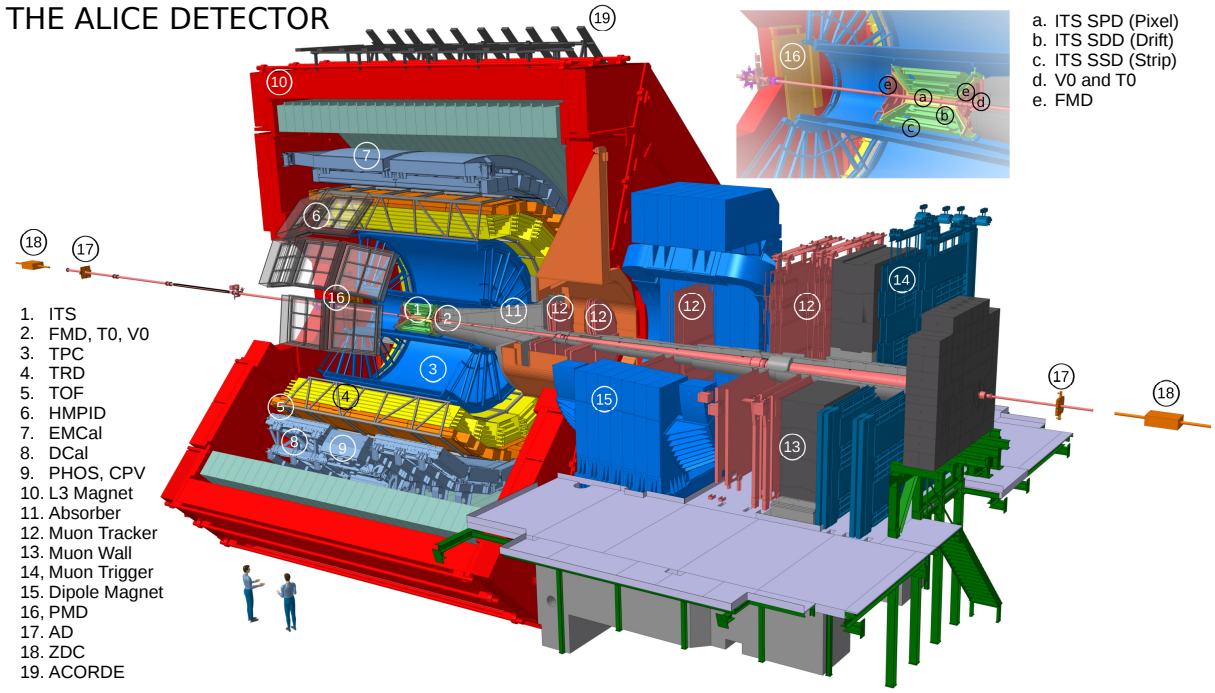

Figure 4.2: Scheme of the ALICE detector set-up during the Run 2 data taking (2015-2018) [39].

geometry and cover the full azimuthal angle. These include the Inner Tracking System (ITS) consisting of position-sensitive silicon detectors that surround the IP 2, the Time Projection Chamber (TPC), the Transition Radiation Detector (TRD) and the Time-Of-Flight detector (TOF). Beyond these, one can find the High Momentum Particle Identification Detector (HMPID) and three electromagnetic calorimeters: the Electromagnetic Calorimeter (EMCal), the Photon Spectrometer (PHOS) and the Di-Jet Calorimeter (DCal). The detectors mentioned above are used for the tracking of particles with high precision or the identification of particles employing some of the common particle identification (PID) techniques: specific energy losses $\mathrm{d}E/\mathrm{d}x$, time-of-flight measurements, transition radiation, Cherenkov radiation etc.

ALICE also makes use of several forward detectors which include the T0, the V0, the AD, the Forward Multiplicity Detector (FMD), the Photon Multiplicity Detector (PMD) and the Zero-Degree Calorimeters (ZDCs). These are situated in close proximity to the beam pipe at small polar angles.

The forward detectors are significant for timing purposes (measurements of the collision time), they provide triggers (e.g. centrality or minimum bias trigger) and separate beam-beam interactions from the background events such as beam-gas interactions [40]. Besides, they can be used to measure global event characteristics such as multiplicity and spatial distribution of particles or event-plane direction and the centrality of nucleus-nucleus collisions. Lastly, some of them participate in beam luminosity measurements.

Some of the forward detectors are comprised of two components, each covering the opposite pseudorapidity side. In this case, the forward ($\eta > 0$) component is denoted by the ending A and the backward ($\eta < 0$) component with C. As indicated in Fig. 4.2, the AD and ZDC components lie outside the L3 solenoid, at an approximate distance of 20 and 113 m away from the IP, respectively.

The detectors that are important in the analysis of UPC events in central or forward

rapidity are described in the rest of this chapter. Most of the following sections are based on Chapter 3 of the Research project [4] where a detailed description of the corresponding ALICE detectors was given.

4.3 Inner Tracking System

The Inner Tracking System (ITS) is the innermost ALICE detector and its main purpose is to locate the primary vertex, reconstruct the secondary vertices, to track and identify particles with low transverse momentum ($p_{\mathrm{T}} \lesssim 0.2$ GeV/c) or particles traversing the TPC dead zones and to improve the results provided by the TPC on the tracks of particles with higher transverse momentum [41].

The ITS is composed of six concentric cylindrical layers of silicon detectors. The two inner layers are made of Silicon Pixel Detectors (SPD), the two middle layers consist of Silicon Drift Detectors (SDD) and the two outer layers exploit the Silicon Strip Detectors (SSD) technology.

The description above refers to the original ITS that operated during Run 1 and Run 2 of the LHC. A complete upgrade of the ITS has been carried out during LS 2. The new design relies on seven layers of 50-μm thick ALPIDE chips that are based on a CMOS Monolithic Active Pixel Sensor (MAPS) technology [42], where the sensor and readout circuitry are integrated into the same silicon wafer. The upgraded ITS will be able to make high-precision tracking of particles with p_{T} up to 1 GeV/c [42].

4.4 Time Projection Chamber

The Time Projection Chamber (TPC) can be considered the main ALICE tracking detector in the midrapidity region. It was designed for the tracking of charged particles, their identification via $\mathrm{d}E/\mathrm{d}x$ and the determination of vertices. The TPC has a good ability to separate two nearby tracks and is capable of detecting particles in a wide range of transverse momenta, from 0.1 to 100 GeV/c. Its pseudorapidity acceptance corresponds to $|\eta| < 0.9$ for the tracks traversing the whole TPC volume and can be extended up to $|\eta| < 1.5$ for reduced track lengths.

The schematic view of the ALICE TPC is shown in Fig. 4.3 (left). It consists of a gas-filled cylindrical field cage with two anodes located at the end caps and a central high-voltage cathode that divides the active volume into halves. The active volume is 500 cm long and has an inner and outer radius of 85 and 250 cm, respectively. It is filled with 90 m^3 of an optimised gas mixture consisting of Ne, CO_2 and N_2 mixed in the ratio 86:10:5 [43]. The central electrode, which is made of a thin aluminised Mylar foil to reduce the amount of material near the IP, is set to a voltage of –100 kV. Thanks to other Mylar strips that are wound around 18 inner and 18 outer longitudinal support rods and connected to resistive potential dividers, a highly uniform axial electric field with an intensity of 400 V/cm is produced.

In general, a long time response is typical of the TPCs. The end plates are radially segmented into 18 inner and 18 outer trapezoidal sections where Inner and Outer Read-Out Chambers (IROC and OROC) are mounted. Their design is based on the Multi-Wire Proportional Chamber (MWPC) technique with cathode pad readout as depicted in Fig. 4.3 (right). When a charged particle traverses the active volume of the TPC, electron-ion pairs are produced in primary ionisation events. The charge carriers are attracted by electrodes of the opposite charges, so the released electrons begin to drift towards the grid of anode wires situated above the pad planes. The anode voltage is set to 1350 V (1570 V) for the IROC (OROC) modules [43]. During the drift, the electrons move with a constant velocity of 2.65 cm/μs. Thus, given the length of the

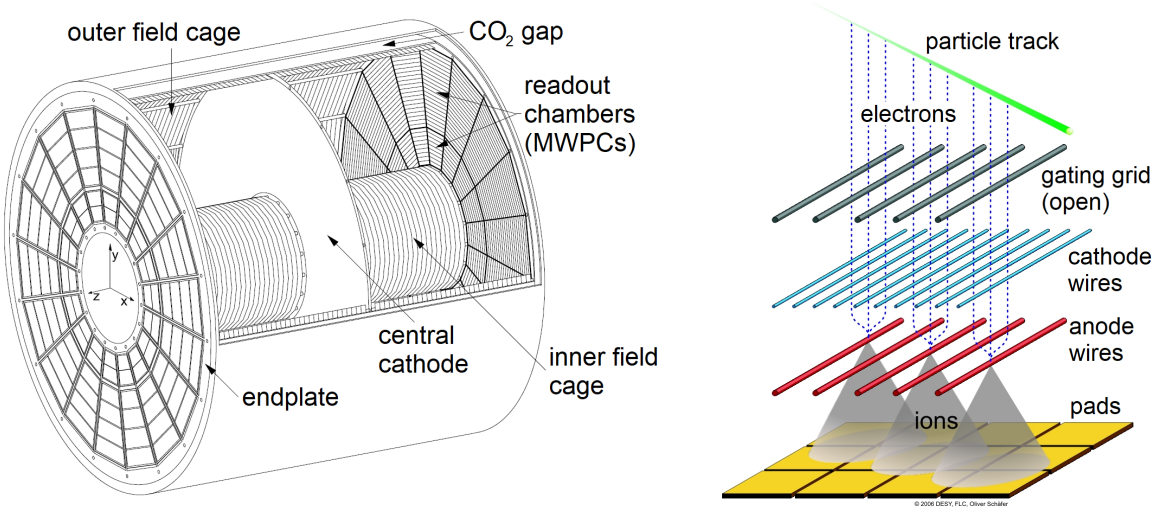

Figure 4.3: Left: The layout of the ALICE TPC field cage [44]. Right: The schematic view of the signal creation in the MWPC modules [45].

active region and the gas mixture composition, the maximum drift time of electrons corresponds to 94 μs [43].

When the electrons approach the anode wires, the field strength is high enough to form Townsend avalanches where secondary ionisation occurs and a lot of positive ions are produced. These ions are then attracted towards the cathode pads (see Fig. 4.3 (right)) and their movement induces current signals from which 2D coordinates in the transverse direction can be reconstructed. The z coordinate is obtained from the drift time of electrons. In the radial and longitudinal directions, the TPC resolution ranges between 800 and 1250 μm [43].

The wire plane delimiting the drift volume is referred to as a gating grid and its main task is (i) to prevent unwanted events from being registered and (ii) to prevent the secondary ions created near the anode wires from moving towards the central cathode which would lead to undesirable space-charge effects. In the open state, a slightly negative voltage V_G is applied to all the wires making the grid transparent for both the electrons and ions. It is switched to the closed state by shifting the voltage on alternate wires to $V_G \pm \Delta V$ [43]. The gate is controlled by the signal from an L1 trigger that is received approximately 7 μs after the interaction time. It can then be opened for a time window of ≈ 90 μs corresponding to the maximum drift time of electrons.

It is necessary to ensure a perfect thermal uniformity inside the TPC so that the drift speed of electrons is not influenced by temperature gradients. For this reason, the whole device is sealed in a vessel containing an insulating CO_2 atmosphere and provided with heat screens installed between the TPC and the surrounding detectors.

4.5 The Time-Of-Flight detector

The Time-Of-Flight (TOF) detector at ALICE is used to perform charged particle identification in the intermediate range of momenta by measuring their velocity $\beta = v/c$. It is able to separate pions from kaons and kaons from protons with a separation of at least 3σ up to momenta of 2.5 GeV/c for π/K and 4.0 GeV/c for K/p [46]. An example of the TOF velocity measurements in Pb–Pb collisions at $\sqrt{s_{\mathrm{NN}}} = 2.76$ TeV can be found in Fig. 4.4 (left). For central UPC

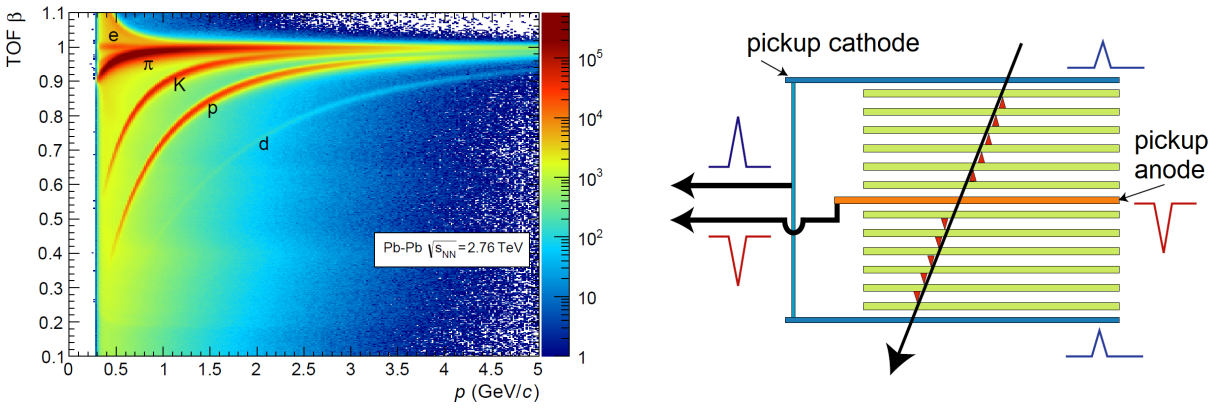

Figure 4.4: Left: A distribution of β measured by TOF as a function of particle momentum p [46]. Right: A schematic layout of a 10 gap double-stack MRPC unit [47] (modified).

triggers, TOF provides the number of fired pads as well as the number of back-to-back hits with a predefined opening angle.

TOF is a large-area cylindrical array located beyond the TRD detector at a radial distance of 370–399 cm from the beam axis with a pseudorapidity acceptance of $|\eta| < 0.9$ and a full azimuthal coverage. The device is of a modular structure divided azimuthally into 18 supermodules, which are segmented into 5 gas-tight modules in the z direction. The basic detection units of TOF are comprised of 122×13 cm^2 tilted strips employing the Multi-gap Resistive-Plate Chamber (MRPC) technology and are placed inside the modules. The MRPC stripes are designed as double-stacks with 10 gaps of 250 μm and are equipped with a central anode pad and two cathode pads as shown schematically in Fig. 4.4 (right).

The incoming particle produces primary ionisation clusters in each of the gaps. As a result, Townsend avalanches are formed in the gaps separately and their sum creates a current signal that is measured on the cathode and anode pads. This design brings an obvious advantage as the presence of resistive plates prevents the spark formation and the detector can be operated at considerably high particle fluxes. The ALICE MRPC stripes thus reach an intrinsic time resolution of 40 ps and an efficiency of almost 100%. Coming back to TOF, it was designed so that its occupancy does not exceed 15% even at the highest anticipated multiplicities ($\mathrm{d}N/\mathrm{d}\eta \approx 8000$) and has an overall time resolution of 80 ps [46].

The operation of the TOF detector is closely related to the T0 forward Cherenkov counter because its modules T0A and T0C generate a start time for the time-of-flight measurement after which the TOF time window is opened for 500 ns. Time resolution of the T0 components is $\sim$ 20-25 ps (40 ps) for Pb–Pb (pp) collisions [46].

4.6 The V0 detector

The V0 system is composed of two arrays of scintillator counters placed asymmetrically at about 329 cm (V0A) and −87 cm (V0C) away from the IP and covering the pseudorapidity ranges of $2.8 < \eta < 5.1$ and $-3.7 < \eta < -1.7$, respectively. The V0C is mounted to the front of the muon arm hadronic absorber.

Both V0 modules are segmented into four rings radially and into eight sectors of 45° azimuthally. This makes a total of 32 individual cells that are made of BC404 plastic scintillator. When a particle traverses the sensitive volume of an organic scintillator, it deposits a part of its

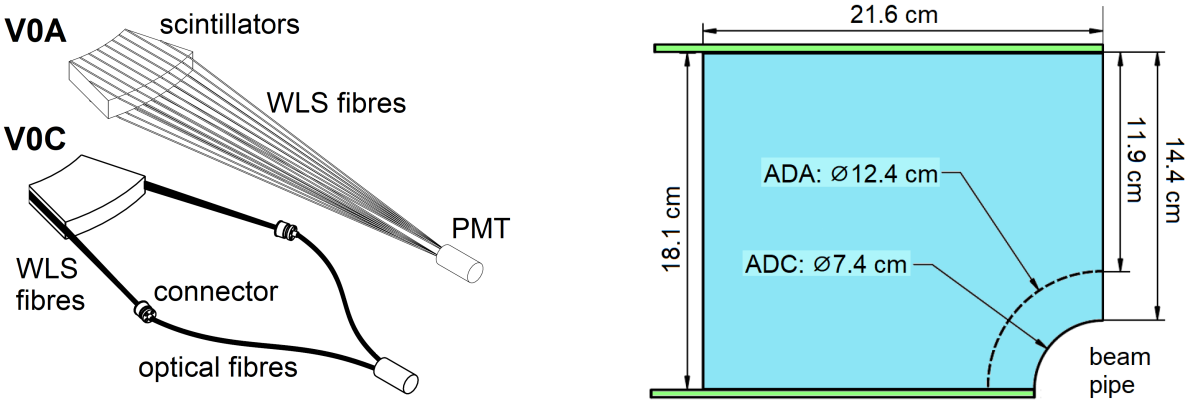

Figure 4.5: Left: Connection of the V0 cells to WLS fibres [38] (modified). Right: Diagram of the AD plastic scintillator pads (blue) and adjacent WLS bars (green) [48] (modified).

energy into excitation of molecules, which can subsequently de-excite via a luminescent process, i.e. the emission of light. In the V0 cells, the light signals are collected by wavelength shifting (WLS) fibres which are connected to photomultiplier tubes (PMTs), as can be seen in Fig. 4.5 (left).

The primary role of V0 is to provide ALICE with a minimum-bias (MB) trigger in both pp and heavy-ion collisions. Several configurations of the MB trigger were used in the past, most of them required hits in one or both of the V0 modules (alternatively accompanied with a hit in the SPD detector) [46]. The V0 also enables to determine centrality by measuring the multiplicity of particles and, when both V0 components are operated in coincidence, it allows for the luminosity measurements [40]. Last but not least, by requiring a positive time of arrival in both arrays, the V0 can help to discriminate between beam-beam and unwanted beam-gas collisions [46].

4.7 The AD detector

The Alice Diffractive (AD) detector was installed during LS 1 in order to enhance the capability of the ALICE apparatus to study diffractive processes and ultra-peripheral collisions.

The AD is composed of two devices situated close to the beam pipe at a rough distance of 18 m and −20 m [16] covering the pseudorapidity intervals of $4.7 < \eta < 6.3$ (ADA) and $-6.9 < \eta < -4.9$ (ADC) [48]. Both AD detectors consist of two identical parallel layers of BC404 plastic scintillators that are divided into four pads of approximate dimensions $22 \times 19 \times 2.5$ cm^3 [48], see Fig. 4.5 (right). Each cell is attached to WLS bars from which the collected light signal is transferred to PMTs via optical fibres.

Owing to its extensive pseudorapidity coverage at small angles, the AD can be considered an extension of the V0 detector and was designed for similar purposes: besides its usage in diffractive physics, it contributes to level 0 (L0) trigger signals, performs beam-background monitoring, measures the centrality and acts as a luminometer [48]. During LS 2, the AD has been upgraded to the Forward Diffractive Detector (FDD) that has the same geometry but exploits faster materials; in particular, the WLS re-emission time will be reduced to 0.9 ns from 8.5 ns [48]. The detector will thus be suitably adapted to conditions that are expected at higher luminosities in Run 3 and Run 4 of the LHC.

As for the role of V0 and AD in measuring UPCs, they provide a veto to suppress events with possible contamination by hadronic interactions. For the case of vector-meson photoproduction

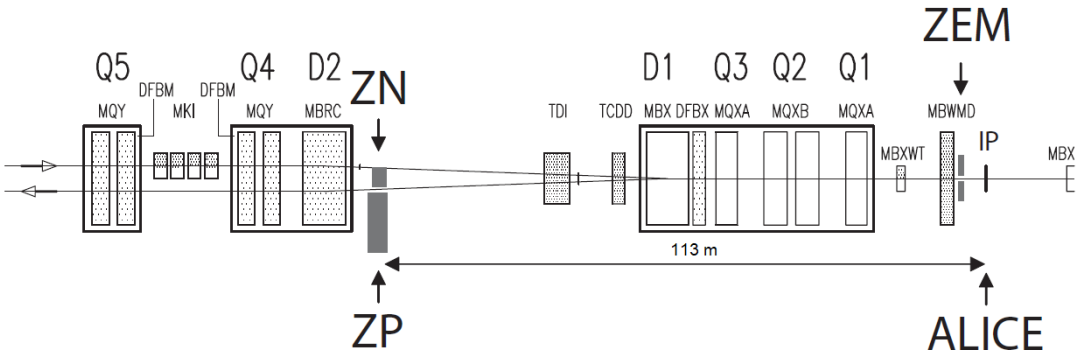

Figure 4.6: Layout of the ZDC system [38]. Colliding beams are indicated by two horizontal lines, Dx and Qx denote positions of the dipole and quadrupoles magnets.

at midrapidity, all the V0 and AD modules are required to be empty (detect no activity), while for the forward analysis the condition on V0C is excluded since its pseudorapidity coverage largely overlaps with that of the muon spectrometer.

4.8 The Zero-Degree Calorimeters

The Zero Degree Calorimeter (ZDC) system consists of forward hadronic and electromagnetic calorimeters that can determine the centrality in heavy-ion collisions by measuring the energy carried away by non-interacting spectator nucleons.

The ZDC is composed of two sets of hadronic calorimeters located roughly 113 m away from the IP in both directions. Each set comprises two distinct types of calorimeters, dedicated to detection of spectator neutrons (ZN) and protons (ZP) separately. Because the trajectories of spectator protons are deflected in the LHC magnetic field, the ZPs are situated beside the beam pipe, while the ZN calorimeters must be placed between the LHC beams (see Fig. 4.6). The ZDC system is completed by the two components of the electromagnetic calorimeter ZEM which are located at 7 m from the IP and surround the beam pipe from both sides. The pseudorapidity coverages of the individual modules are $6.5 < |\eta| < 7.5$ (ZP), $|\eta| > 8.8$ (ZN) and $4.8 < \eta < 5.7$ (ZEM) [46].

The hadronic ZDCs are sampling calorimeters consisting of a stack of grooved metallic plates. The metallic plates act as a passive absorber and are complemented with quartz fibres that are placed in grooves and form an active medium. The segmentation of the hadronic ZDCs makes it a position-sensitive detector and enables to estimate the reaction plane.

Incident hadrons create hadronic cascades which in turn produce Cherenkov radiation when passing through active fibres. Eventually, the light is converted into an electric signal in PMTs. Since the transverse dimensions (ca. 7×7 cm^2) of the ZNs are limited by the surrounding beam pipes, its absorbers are made of a very dense material (tungsten alloy) to maximise the production of showers. In the case of ZPs, brass was chosen to form an absorber as the ZP position is less limiting.

In peripheral collisions, spectator nucleons can often remain bounded in fragments having a similar charge-to-mass ratio to that of Pb ions. As this ratio determines the radius of curvature in the magnetic field, such nuclear fragments can escape without being detected and the energy measured by the ZDC will be lower than the actual value. The ZEM, which focuses on the detection of forward photons, was constructed to overcome this problem. It is again a sampling

calorimeter with a lead absorber and quartz active fibres and the energy deposited in the ZEM decreases monotonically with decreasing centrality of heavy-ion collisions.

The ZDC is very helpful in the analysis of electromagnetic dissociation (EMD) of nuclei in UPCs. In this case, another independent photon-induced interaction occurs between the two nuclei, which can lead to excitations and subsequent dissociation accompanied by the emission of forward neutrons that can be detected in the ZDC. This enables one to divide the analysed events into classes defined according to the number of forward neutrons detected in the ZNA and ZNC.

4.9 The forward muon spectrometer

The muon spectrometer covering $-4.0 < \eta < -2.5$ was designed for the detection of muons coming from the decays of resonances of vector mesons composed of heavy quarks (such as charmonia and bottomia) or the continuum unlike-sign muon pairs with the invariant masses up to 10 GeV/c^2.

In front of the spectrometer, a dense passive absorber that blocks the passage of photons and hadrons is placed, see Fig. 4.2. The absorber is 4.13 m long and is dominantly made of carbon and concrete. The shielding of the spectrometer across its whole length is further provided by a dense absorber tube made of tungsten, lead and steel which surrounds the beam pipe.

The tracking of muons is ensured by the tracking chambers with a resolution of about 100 μm that are placed in five stations, each station being equipped with two chamber planes. The middle station (station 3) is placed inside the dipole magnet with 0.67 T, see Fig. 4.2. The trigger chambers occupy stations 6 and 7 that are situated beyond another muon filter in the form of a 1.2 m-thick iron wall.

In LS 2, the Muon Forward Tracker (MFT) detector covering $-3.6 < \eta < -2.5$ was installed in front of the main absorber of the muon spectrometer. Starting from Run 3, it will considerably improve the measurements performed by the muon spectrometer, it will mainly enhance its vertexing capabilities.

4.10 UPC triggers in 2018

For the purpose of the Run 2 measurements described in Chapter 5 as well as the analysis presented in Chapter 6, the central barrel UPC trigger classes operated in 2018 will be described in this section.

The list includes three classes:

- CCUP29 = !0VBA !0VBC !0UBA !0UBC 0STG,
- CCUP30 = !0VBA !0VBC !0UBA !0UBC 0STG 0OM2 and
- CCUP31 = !0VBA !0VBC !0UBA !0UBC 0STG 0OMU,

which are based on the following Level 0 (L0) trigger inputs:

- !0VBA (!0VBC) = no signal in the V0A (V0C) during the beam-beam time window,
- !0UBA (!0UBC) = no signal in the ADA (ADC) during the beam-beam time window,
- 0STG = the SPD topological trigger demanding at least two back-to-back tracklets[1] with a predefined opening angle in azimuth,

[1] Tracklets are short track segments made of two hits, each in a different layer of the SPD detector.

- 0OMU = between two and six hits in the TOF detector with at least two of them having an opening angle in azimuth $150° < \Delta\phi < 180°$ and
- 0OM2 = two or more hits in TOF.

4.11 Data flow in ALICE

The reconstruction and calibration of the data measured with ALICE is provided by the ALICE Data Preparation Group (DPG), which is also responsible for the Quality Assurance (QA) of the data. The data arriving from the detector are the so-called raw data, which have to be further processed, calibrated and the reconstruction of tracks and vertices is conducted, so that the data can be stored in the form of Event Summary Data (ESD) files. The ESDs may be used for the subsequent physics analysis, but they contain quite a lot of information that might not be necessary for most of the analyses, so working with them can be unnecessarily inefficient and memory-consuming.

Therefore, a lighter compressed data format that is called Analysis Object Data (AOD) is created. Storage, subsequent accession and the analysis of the data is done within the ROOT framework, which is a CERN-developed object-oriented library based on C++. As the performance of the user's computer is usually insufficient to work with large amounts of data efficiently, the Worldwide LHC Computing Grid (simply abbreviated as Grid) is used to distribute, store and analyse the data. The user can run over the AOD files on the GRID using the so-called LEGO train system, thereby creating the nano-AOD files. In the case of UPC events, the nano-AODs are very compact thanks to low multiplicities of produced particles. The analysis in Chapter 6 is based on the UPC nano-AOD files which were centrally produced.

Chapter 5

Previous measurements of J/ψ diffractive photoproduction

In this chapter, the previous measurements of J/ψ photoproduction in ultra-peripheral Pb–Pb collisions by ALICE will be summarised. To date, the ALICE Collaboraton published only one paper describing the incoherent photoproduction of J/ψ which is based on the midrapidity ($|y| < 0.9$) data collected in 2011 during Run 1 of the LHC at $\sqrt{s_{\mathrm{NN}}} = 2.76$ TeV [31]. A detailed description of this article can be found in the Research project [4] but it will be briefly recapitulated in Sec. 5.1 as it can be considered a direct predecessor of the analysis presented in Chapter 6.

The rest of this chapter focuses on the latest ALICE measurements of the coherent J/ψ and $\psi(2S)$ photoproduction in Pb–Pb collisions at $\sqrt{s_{\mathrm{NN}}} = 5.02$ TeV recorded during Run 2. Analyses of both the coherent and incoherent nuclear photoproduction are closely related, so this review offers a useful insight. In Sec. 5.2, the rapidity-differential measurement of the dimuon decay of coherent J/ψ at forward rapidity $-4.0 < y < -2.5$ employing the muon spectrometer is presented [49]. Section 5.3 then summarises the midrapidity photoproduction of both the J/ψ and $\psi(2S)$ vector mesons [20]. Eventually, the first results on the $|t|$-dependence of the coherent J/ψ photoproduction at midrapidity [25] is reviewed in Sec. 5.4.

5.1 Coherent and incoherent J/ψ photoproduction at midrapidity at $\sqrt{s_{\mathrm{NN}}} = 2.76$ TeV

Given the kinematic range of the analysed sample ($|y| < 0.9$, $\sqrt{s_{\mathrm{NN}}} = 2.76$ TeV), Eq. (2.3) implies that the analysis in [31] probed the nuclear gluon distribution at $x \in (0.5, 3.0) \cdot 10^{-3}$. The leptonic decay channels of J/ψ were investigated in order to acquire the cross sections of the coherent and incoherent J/ψ photoproduction, which were then compared with predictions of various phenomenological models. In addition, the cross section of the pair production ($\gamma\gamma \to e^+e^-$) was calculated.

A barrel ultra-peripheral collision (BUPC) trigger required events with just two central tracks in an otherwise empty detector and yielded $\approx 6.5 \times 10^6$ events that were subjected to subsequent selections. See [31] or [4] for the BUPC characteristics and the comprehensive list of additional criteria. The integrated luminosity of the analysed sample was $\mathcal{L} = 23.0^{+0.7}_{-1.2}\ \mu\mathrm{b}^{-1}$.

In order to roughly separate the lepton pairs originating from the decay of coherently or incoherently produced J/ψ, an additional selection on the transverse momentum of the parent

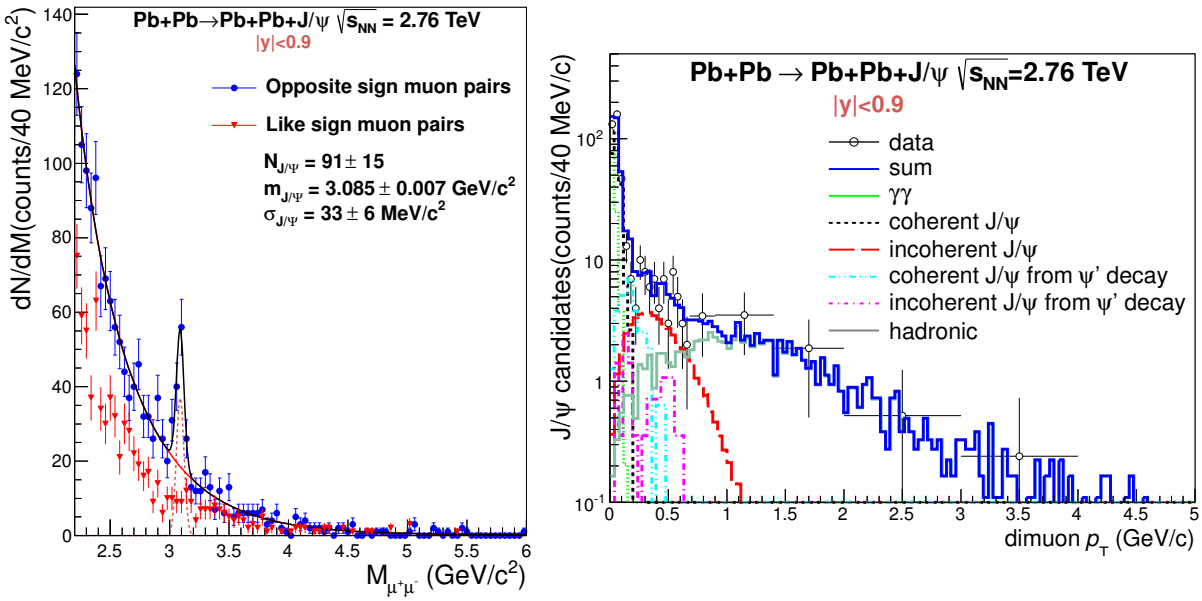

Figure 5.1: Left: The invariant mass distribution of the muon pairs in the incoherent-enriched sample ($p_{\mathrm{T}} > 0.2$ GeV/c) [31]. Right: Transverse momentum distribution of muon pairs with the invariant mass between $3.0 < m_{\mu\mu} < 3.2$ GeV/c^2 [31].

system[1] had to be applied. The p_{T} threshold between the so-called coherent and incoherent-enriched samples was set to 200 (300) MeV/c for dimuons (dielectrons).

The acceptance and efficiency correction $(A \times \varepsilon)_{\mathrm{J}/\psi}$ of the J/ψ reconstruction from the leptonic decay products was computed using a large sample of coherent and incoherent J/ψ events generated by STARlight (see Sec. 3.1) and folded with the Monte Carlo simulations of the ALICE detectors. The correction was calculated as a ratio of the number of simulated events passing all the selections applied to real data to the number of generated events in the rapidity interval $|y| < 0.9$. This procedure yielded the values of 2.71 (4.57)% and 1.80 (3.19)% for dielectrons (dimuons) belonging to the coherent and incoherent-enriched sample, respectively.

The invariant mass distribution of opposite-sign dileptons in the range $2.2 < m_{\mu\mu} < 6.0$ GeV/c^2 was fitted using the Crystal Ball function to describe the J/ψ signal peak and an exponential function (with an extra 5^{th} order polynomial in the incoherent sample) to describe the background. As an example, the fit of the incoherent-enriched sample containing dimuons is depicted in Fig. 5.1 (left). The resulting yields of J/ψ mesons from the coherent (incoherent) samples can be found in Table 5.1a (5.1b) for muon and electron channels separately.

The raw yields N_{yield} also contain contributions from other processes than the desired decay of the coherent or incoherent J/ψ. Restricting the discussion from now on to the incoherent photoproduction, the incoherent-enriched sample is indeed contaminated by dileptons coming from (i) the decay of the coherent J/ψ as well as from (ii) *feed-down* reactions. The latter corresponds to a situation where the excited charmonium state $\psi(2S)$ is exclusively photoproduced and later decays via $\psi(2S) \to \mathrm{J}/\psi + X$, where X is not registered by the detectors. X is often a pair of charged or neutral pions ($\pi^+\pi^-$ or $\pi^0\pi^0$). In such a case, the lepton pair which can be created in a subsequent decay of J/ψ might be misidentified as a decay product of a photoproduced J/ψ even though J/ψ itself is only a decay product of the photoproduced $\psi(2S)$.

[1] In the context of this thesis, the parent system l^+l^- reconstructed from the track of two leptons l^+ and l^- is referred to as a *dilepton*.

Sample	Muons	Electrons
$N_{\rm yield}$	291 ± 18 (stat.) ± 4 (syst.)	265 ± 40 (stat.) ± 12 (syst.)
f_D	$0.10^{+0.05}_{-0.06}$	$0.10^{+0.05}_{-0.06}$
f_I	0.044 ± 0.014	0.150 ± 0.020
$N^{\rm coh}_{\rm J/\psi}$	255 ± 16 (stat.) $^{+14}_{-13}$ (syst.)	212 ± 32 (stat.) $^{+14}_{-13}$ (syst.)
$\mathrm{d}\sigma^{\rm coh}_{\rm J/\psi}/\mathrm{d}y$ [mb]	2.27 ± 0.14 (stat.) $^{+0.30}_{-0.20}$ (syst.)	3.19 ± 0.50 (stat.) $^{+0.45}_{-0.31}$ (syst.)
Total $\mathrm{d}\sigma^{\rm coh}_{\rm J/\psi}/\mathrm{d}y$ [mb]	$2.38^{+0.34}_{-0.24}$ (stat. + syst.)	

(a) Coherent-enriched sample

Sample	Muons	Electrons
$N_{\rm yield}$	91 ± 15 (stat.) $^{+7}_{-5}$ (syst.)	61 ± 14 (stat.) $^{+16}_{-7}$ (syst.)
f_D	0.095 ± 0.055	0.110 ± 0.070
f_C	0.03 ± 0.03	0.47 ± 0.09
$N^{\rm inc}_{\rm J/\psi}$	81 ± 13 (stat.) $^{+8}_{-6}$ (syst.)	39 ± 9 (stat.) $^{+10}_{-5}$ (syst.)
$\mathrm{d}\sigma^{\rm inc}_{\rm J/\psi}/\mathrm{d}y$ [mb]	1.03 ± 0.17 (stat.) $^{+0.15}_{-0.12}$ (syst.)	0.87 ± 0.20 (stat.) $^{+0.26}_{-0.14}$ (syst.)
Total $\mathrm{d}\sigma^{\rm inc}_{\rm J/\psi}/\mathrm{d}y$ [mb]	$0.98^{+0.19}_{-0.17}$ (stat. + syst.)	

(b) Incoherent-enriched sample

Table 5.1: The main experimental results obtained in the analysis of the J/ψ photonuclear production presented in [31]. See the text for the definition of variables.

One thus introduces the ratio f_C (f_D) of the number of coherent (feed-down) events contaminating the incoherent-enriched sample to the number of incoherent events in this sample. This allows one to write for the corrected number of incoherent events $N^{\rm inc}_{\rm J/\psi}$ present in the incoherent-enriched sample the following relation

$$N_{\rm yield} = N^{\rm inc}_{\rm J/\psi} + f_C \cdot N^{\rm inc}_{\rm J/\psi} + f_D \cdot N^{\rm inc}_{\rm J/\psi}\,, \tag{5.1}$$

thus obtaining

$$N^{\rm inc}_{\rm J/\psi} = \frac{N_{\rm yield}}{1 + f_C + f_D}\,. \tag{5.2}$$

Indeed, an analogous relation holds for the number of coherent events $N^{\rm coh}_{\rm J/\psi}$ in the coherent-enriched sample with the corresponding fraction denoted as f_I instead of f_C.

The computed values of the f_D, f_I and f_C corrections are quoted in Tab. 5.1. The fractions f_I and f_C were extracted from the fit of the transverse momentum distribution. For illustration, the measured $p_{\rm T}$ distribution of muon pairs can be found in Fig. 5.1 (right). The data were fitted by the sum of six templates corresponding to different physical processes: (i) coherent and (ii) incoherent J/ψ photoproduction; J/ψ from (iii) coherent or (iv) incoherent $\psi(2S)$ decay; (v) two-photon production of lepton pairs; (vi) J/ψ produced in peripheral hadronic collisions.

For the description of the calculation of systematic errors, see [31]. Finally, the incoherent differential cross section was computed employing the relation

$$\frac{\mathrm{d}\sigma^{\rm inc}_{\rm J/\psi}}{\mathrm{d}y} = \frac{N^{\rm inc}_{\rm J/\psi}}{(\mathrm{Acc} \times \varepsilon)_{\rm J/\psi} \cdot \mathrm{BR}(\mathrm{J/\psi} \to l^+l^-) \cdot \mathcal{L} \cdot \Delta y}\,, \tag{5.3}$$

which holds for the coherent process too if one replaces $N^{\mathrm{inc}}_{\mathrm{J}/\psi}$ with $N^{\mathrm{coh}}_{\mathrm{J}/\psi}$ and substitutes the appropriate value for $(\mathrm{Acc}\times\varepsilon)_{\mathrm{J}/\psi}$. Here BR stands for the branching ratio of the decay of J/ψ into a given pair of leptons and $\Delta y = 1.8$. The resulting cross sections for the muon and electron decay channels can be found in Tab. 5.1. Because both channels are statistically independent samples, the total differential cross section for the coherent and incoherent photoproduction was in both cases calculated as weighted average of the two, the results can be found in the last rows of Tab. 5.1a and 5.1b.

Figure 5.2 shows the comparison of the measured coherent (top) and incoherent (bottom) differential cross sections with the rapidity dependence predicted by phenomenological models. The coherent cross section is in very good agreement with the EPS09 model by Adeluyi and Bertulani which belongs to models based on the LO pQCD (see Sec. 3.2). Generally speaking, the models employing a Glauber approach to calculate the number of nucleons participating in the scattering overestimate the experimental result by a factor of 1.5-2. On the other hand, strong gluon shadowing effects incorporated in the EPS08 parametrisation lead to a considerable underestimation of the data.

The incoherent cross section was found not to be in accordance with the presented models. The STARlight model does not give correct predictions of the coherent and incoherent cross sections individually, but provides an incoherent-to-coherent ratio of 0.41 which accords with the results.

5.2 Coherent J/ψ photoproduction at forward rapidity at $\sqrt{s_{\mathrm{NN}}} =$ 5.02 TeV

The analysis presented in [49] constitutes the first measurement of the coherent J/ψ photoproduction at the Run 2 centre-of-mass energy per nucleon pair, $\sqrt{s_{\mathrm{NN}}} = 5.02$ TeV. The data were taken in 2015 and 2018. The coherently produced J/ψ mesons in the the forward rapidity region, $-4.0 < y < -2.5$, were analysed via their dimuon decay. The whole rapidity range was divided into six bins of equal length (0.25) to study the rapidity dependence of the cross section. According to Eq. (2.3), the forward rapidity corresponds to two regions of gluon Bjorken-x, $1.1\cdot10^{-5} < x < 5.1\cdot10^{-5}$ or $0.7\cdot10^{-2} < x < 3.3\cdot10^{-2}$, depending on which nucleus is the photon source. However, models indicate that the fraction of high Bjorken-x gluons is dominant ($\gtrsim 60\%$) and reaches even $\sim 95\%$ at the lowest rapidity $y = -4$.

The UPC muon trigger was used to select events with two oppositely charged tracks in the muon spectrometer and satisfying online V0A, ADA and ADC vetoes to reject potential hadronic interactions. Both data samples with an estimated integrated luminosities of 216 $\mu\mathrm{b}^{-1}$ (2015) and 538 $\mu\mathrm{b}^{-1}$ (2018) were merged. Altogether, the new method of absolute luminosity normalisation in combination with a bigger size of the data simple ($\approx 200\times$ larger than in the previous Run 1 measurement [30]) resulted in a substantial reduction of statistical and systematic uncertainties.

In the offline selection, the events containing two oppositely charged tracks, both with the pseudorapidity $-4.0 < \eta < -2.5$, were selected. For a thorough description of the offline analysis see [49]. Matching between the track segments in the tracking chambers (stations 1-5) and the trigger chambers (stations 6, 7) was performed and the exclusivity of the produced muon pair was further ensured by requiring offline vetoes in V0A, ADA and ADC and no more than 2 fired cells in V0C. The V0 and AD vetoes on the offline level are more precise as the time window is enlarged to increase the efficiency and the signal is quantified by a more refined algorithm [20].

The results were corrected on the so-called *veto inefficiency* that can be caused by inde-

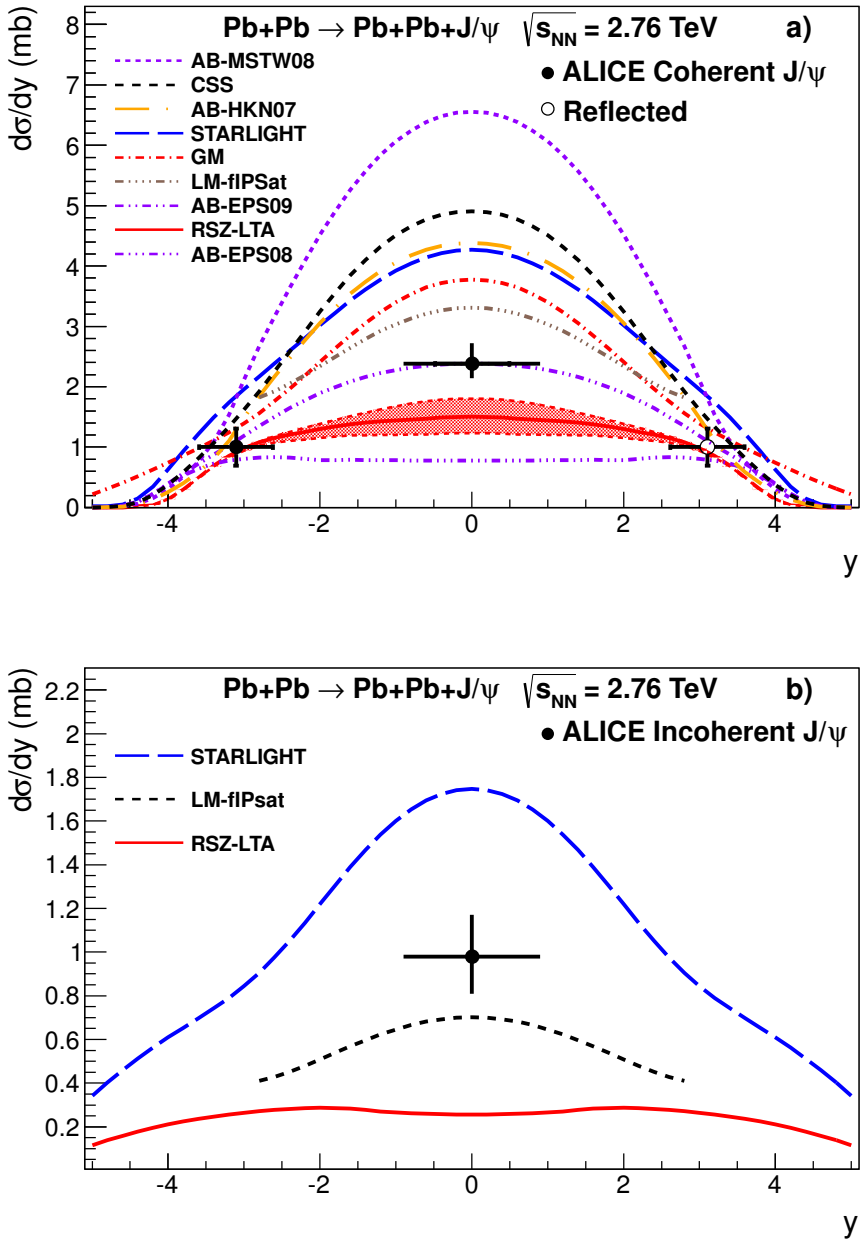

Figure 5.2: Measured differential cross section of the coherent (top) and incoherent (bottom) J/ψ photoproduction in ultra-peripheral Pb–Pb collisions at $\sqrt{s_{\rm NN}} = 2.76$ TeV and $|y| < 0.9$ [31]. The forward coherent measurement was published in [30]. Results are compared with predictions of various models. For the specification of the models see [31].

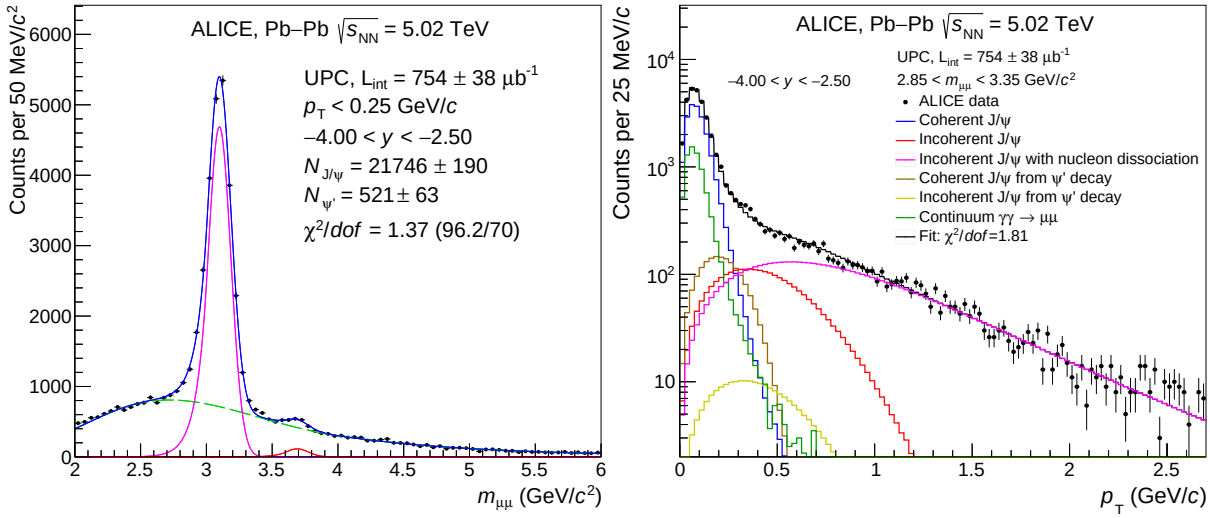

Figure 5.3: Left: The invariant mass distribution of muon pairs in the coherent-enriched sample ($p_{\mathrm{T}} < 0.25$ GeV/c) [49]. Right: Transverse momentum distribution of muon pairs with the invariant mass between $2.85 < m_{\mu\mu} < 3.35$ GeV/c^2 [49].

pendent *pile-up*[2] processes. The average veto efficiency was estimated as $\varepsilon_{\mathrm{veto}} = 95\%$. Similarly to the method described in Sec. 5.1, the acceptance and efficiency $(\mathrm{Acc} \times \varepsilon)_{\mathrm{MC}}$ was evaluated using Monte Carlo events generated in STARlight and simulations of the detector response created with GEANT 3.

A coherent-enriched sample was defined by the selection criterion $p_{\mathrm{T}} < 0.25$ GeV/c. The invariant mass distribution of dimuons was fitted by the sum of two Crystal Ball functions (corresponding to the J/ψ and $\psi(2S)$ peaks) and a fourth-order polynomial for the background at low masses that smoothly turns into an exponential tail for the dimuon masses above 4 GeV/c^2. The fitted mass spectrum for the full rapidity range can be seen in Fig. 5.3 (left). Fits of the invariant mass spectra in separate rapidity bins can be found in [49].

The contaminations of raw J/ψ yields from the invariant mass fits were again separated by means of the fit of the transverse momentum distribution. The p_{T} spectrum of dimuons with $2.85 < m_{\mu\mu} < 3.35$ GeV/c^2 and $-4.0 < y < -2.5$ is depicted in Fig. 5.3 (right), for the spectra in rapidity subranges refer to [49]. Six distinct production mechanisms were recognised, five of which were described by Monte Carlo templates based on the events generated by STARlight. The last contribution, the incoherent J/ψ photoproduction accompanied by nucleon dissociation, which is responsible for the high-p_{T} tail, was described by the H1 parametrisation [50]

$$\frac{\mathrm{d}N}{\mathrm{d}p_{\mathrm{T}}} \sim p_{\mathrm{T}} \left(1 + \frac{b_{\mathrm{pd}}}{n_{\mathrm{pd}}} p_{\mathrm{T}}^2\right)^{-n_{\mathrm{pd}}} , \tag{5.4}$$

with the parameters set to the values $b_{\mathrm{pd}} = 1.79$ (GeV/c)$^{-2}$ and $n_{\mathrm{pd}} = 3.58$ (provided by the H1 collaboration for the data with the photon-proton centre-of-mass energy of $40 < W_{\gamma\mathrm{p}} < 110$ GeV).

When fitting the p_{T} spectrum, the normalisations of the coherent J/ψ, the incoherent J/ψ and the incoherent J/ψ with nucleon dissociation were left free. The normalisation of the

[2]When the vector meson photoproduction is accompanied by an independent electromagnetic or hadronic interaction which occurs in the same bunch crossing and leaves a signal in the V0 or AD detector, it may result in the rejection of the event by online or offline vetoes. The *pile-up correction* has to be calculated in order to account for the lost of potentially interesting events.

$\gamma\gamma \to \mu^+\mu^-$ contribution was fixed to the number of background events with $2.85 < m_{\mu\mu} < 3.35$ GeV/c^2 obtained from the invariant mass fit and the feed-down normalisations were fixed to the primary coherent and incoherent normalisations multiplied by the appropriate f_D fractions. Eventually, the f_I fraction was calculated as $f_I = N_{\mathrm{inc}}/N_{\mathrm{coh}}$, where N_{coh} and N_{inc} is the number of coherent and incoherent (including incoherent followed by nucleon dissociation) events with $p_{\mathrm{T}} < 0.25$ GeV/c. For the considered rapidity bins, values of the f_I fraction range between 4.9 and 6.4%.

The raw J/ψ and $\psi(2S)$ yields from the invariant mass fit in Fig. 5.3 (left) provided the ratio of $R_N = N_{\psi(2S)}/N_{\mathrm{J}/\psi} \approx 0.025$. This result was used to compute the ratio R of the coherent photoproduction cross section of $\psi(2S)$ to that of J/ψ, which was determined as $R \approx 0.15$. The value of R, along with various efficiencies estimated from STARlight, was then employed to extract the values of the feed-down correction f_D, for the details on this method see [49]. For the full rapidity range and $p_{\mathrm{T}} < 0.25$ GeV/c, the result of $f_D \approx 5.5\%$ was obtained.

The relation analogous to Eq. (5.3),

$$\frac{\mathrm{d}\sigma^{\mathrm{coh}}_{\mathrm{J}/\psi}}{\mathrm{d}y} = \frac{N^{\mathrm{coh}}_{\mathrm{J}/\psi}}{(\mathrm{Acc}\times\varepsilon)_{\mathrm{MC}}\cdot\varepsilon_{\mathrm{veto}}\cdot\mathrm{BR}(\mathrm{J}/\psi\to\mu^+\mu^-)\cdot\mathcal{L}\cdot\Delta y}\,, \tag{5.5}$$

with $\mathcal{L} = 754\ \mu\mathrm{b}^{-1}$ was used to calculate the coherent differential cross section in each rapidity bin. The results are plotted in Fig. 5.4. The authors also determined the overall value for the full rapidity range as $\mathrm{d}\sigma^{\mathrm{coh}}_{\mathrm{J}/\psi}/\mathrm{d}y = 2.549 \pm 0.022\ (\mathrm{stat.})\ ^{+0.209}_{-0.237}\ (\mathrm{syst.})$ mb.

A complete summary of experimental results can be found in Tab. 1 in [49]. For the discussion about various contributions to systematic uncertainties refer also to [49]. A possible source of a systematic error that is worth mentioning here due to its relevance for the analysis in Chapter 6 is the shape of the $\gamma\gamma \to \mu^+\mu^-$ template taken from STARlight, which was used in the transverse momentum fit. As can be seen in Fig. 5.3 (right), the maximum p_{T} of the dimuons in the STARlight template does not exceed a few hundred MeV/c because STARlight does not take into account incoherently emitted photons, whose p_{T} may extend well above 1 GeV/c. The alternative is to create the template from the measured data that lie in the so-called side bands of the J/ψ peak in the invariant mass spectrum.

Figure 5.4 offers a comparison of the results with the rapidity dependence predicted by different models. The suppression factor S_{Pb} was determined using Eq. (3.26) to be around 0.8, which is the expected value for gluons with $x \sim 10^{-2}$, see Fig. 1.6, under the assumption that the low-x contribution $x \sim 10^{-5}$ can be neglected. The accordance between the data and the individual models will be discussed at the end of Sec. 5.3, where the latest midrapidity results are also taken into account.

5.3 Coherent J/ψ and $\psi(2S)$ photoproduction at midrapidity at $\sqrt{s_{\mathrm{NN}}} = 5.02$ TeV

The measurement of the coherent J/ψ photoproduction at forward rapidities in Pb–Pb collisions at $\sqrt{s_{\mathrm{NN}}} = 5.02$ TeV presented in the previous section was recently supplemented with the analysis in the central rapidity region $|y| < 0.8$ performed by the ALICE Collaboration [20].

The J/ψ was detected via its leptonic ($\mu^+\mu^-$ or e^+e^-) and proton-antiproton ($\mathrm{p\overline{p}}$, measured for the first time in UPCs) decay channels and the cross section was determined in three rapidity bins: $|y| < 0.15$, $0.15 < |y| < 0.35$, $0.35 < |y| < 0.8$, containing approximately equal numbers of candidates. Additionally, the cross section of the coherent $\psi(2S)$ photoproduction at $|y| < 0.8$ was calculated by investigating its decay to $\mu^+\mu^-\pi^+\pi^-$, $e^+e^-\pi^+\pi^-$ or pure lepton pairs, l^+l^-.

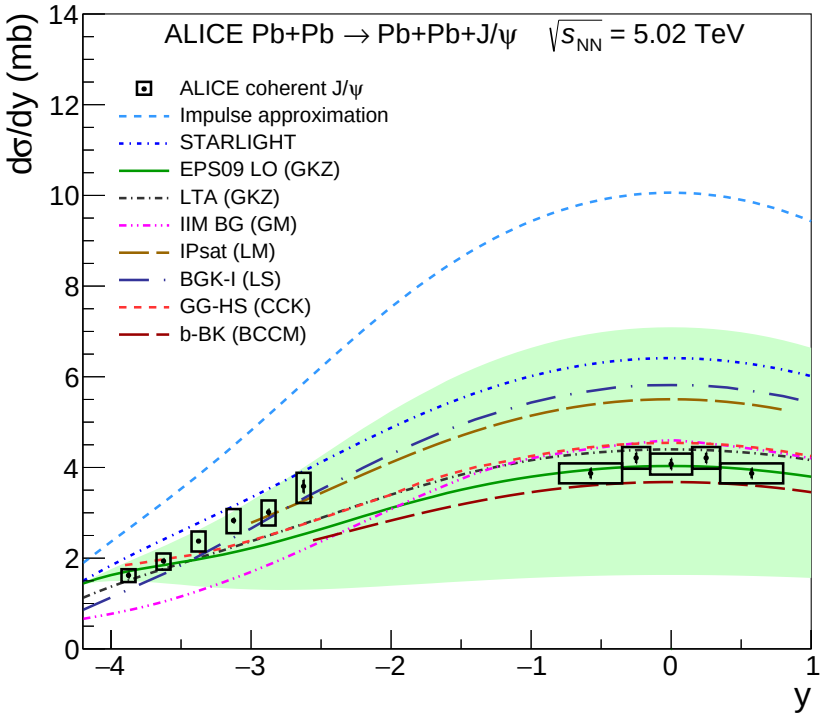

Figure 5.4: Measured coherent differential cross section of the J/ψ photoproduction in six forward rapidity bins [49] and in three central rapidity intervals [20]. The results are compared with predictions of various models, which are specified in [20]. The uncertainty of the EPS09 LO calculation is indicated by the green band.

The interval of probed Bjorken-x of gluons corresponds to $x \in (0.3,\, 1.4) \cdot 10^{-3}$, about a factor of 2 smaller than in the measurement at $\sqrt{s_{\mathrm{NN}}} = 2.76$ TeV described in Sec. 5.1.

The events were triggered by the central barrel UPC trigger classes CCUP29, CCUP30 and CCUP31 introduced in Sec. 4.10. The data sample corresponds to the integrated luminosity of 233 $\mu\mathrm{b}^{-1}$ (about 10 times larger than in the Run 1 measurement [31]), which was estimated from a van der Meer scan with the overall uncertainty of 2.7%. The dataset was then subjected to the list of offline selections, see [20]. Each event is required to have a reconstructed primary vertex from at least two reconstructed tracks that is no more than 15 cm away from the nominal interaction point along the beam direction.

Additional offline V0 and AD veto requirements were applied and the average veto efficiency was estimated as $\varepsilon_{\mathrm{veto}}^{\mathrm{pileup}} = 92\%$. Furthermore, a correction on the *electromagnetic nuclear dissociation*[3] (EMD) was taken into account and the corresponding efficiency was determined as $\varepsilon_{\mathrm{veto}}^{\mathrm{EMD}} = 92\%$.

The two-body decays were selected by requiring events with exactly two global tracks of opposite charges. In the four-body decays of $\psi(2S)$, the events with four tracks were selected and pion pairs were always identified with two tracks of the lowest transverse momentum assuming those tracks were oppositely charged. The TPC and TOF detectors were used for the particle identification employing measurements of $\mathrm{d}E/\mathrm{d}x$ and of the Lorentz factor $\beta = v/c$. In the

[3]In the exclusive charmonium photoproduction, the nuclei can be left in the excited states and later dissociate electromagnetically. Forward neutrons registered by the ZDC can be often accompanied by other particles produced in less forward directions, which may leave a signal in the AD or V0. Thus the event can be rejected by vetoes and the *EMD correction* has to be applied.

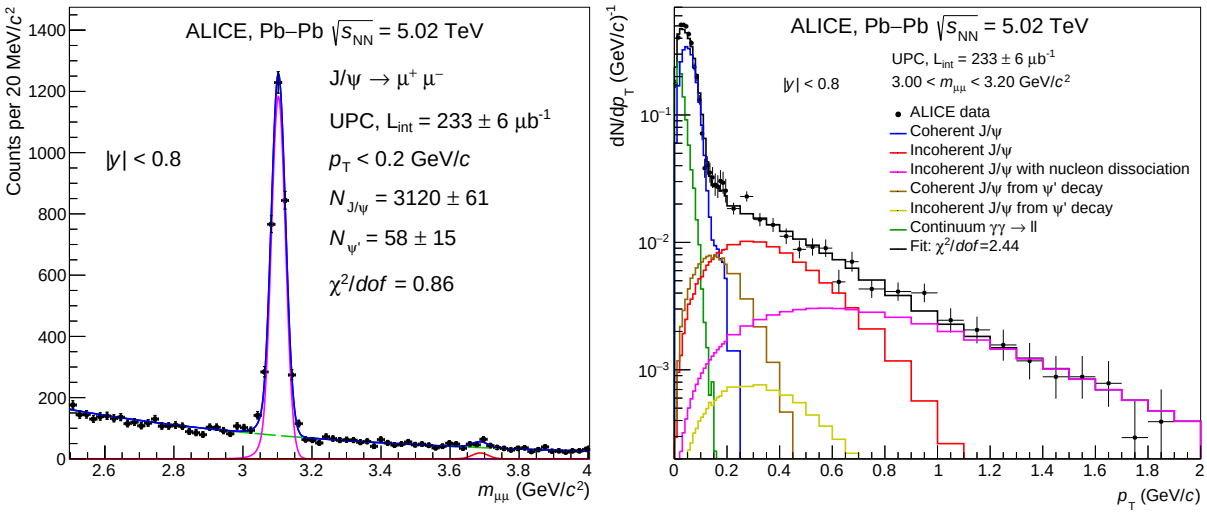

Figure 5.5: Left: The invariant mass distribution of muon pairs in the coherent-enriched sample ($p_{\mathrm{T}} < 0.2$ GeV/c) [20]. Right: Transverse momentum distribution of muon pairs with the invariant mass between $2.85 < m_{\mu\mu} < 3.35$ GeV/c^2 [20].

J/$\psi \to \mathrm{p\bar{p}}$ channel, at least one particle was required to be identified with a proton based on the TOF measurement because the TPC is not able to distinguish well between protons and electrons at the transverse momenta of $p_{\mathrm{T}} < 1$ GeV/c.

The Monte Carlo sample of coherent and incoherent charmonium events generated by STARlight and the simulation of ALICE detectors in GEANT 3 were used to evaluate the acceptance and efficiency of the reconstruction of charmonia.

The coherent-enriched samples of J/ψ and $\psi(2S)$ candidates were constrained by $p_{\mathrm{T}} < 0.2$ GeV/c. The raw yields of both vector mesons were again obtained by means of a fit of the invariant mass distribution of the candidates. As an example, consider Fig. 5.5 (left), where the invariant mass spectrum of dimuons is shown. The fit is a sum of three probability density functions, corresponding to two Crystal Ball functions describing the J/ψ and $\psi(2S)$ peaks and an exponential to account for the continuum. The parameters describing the tails of the J/ψ Crystal Ball function as well as all the parameters of the second Crystal Ball function were constrained to values obtained in the fits of the Monte Carlo data samples generated in STARlight.

In order to separate the unwanted contributions to raw J/ψ yields, the standard procedure employing the fit of the transverse momentum distribution was used. The fit of the p_{T} spectrum of dimuons is shown in Fig. 5.5 (right), the high-p_{T} tail was again described by the H1 parametrisation [50]. The normalisations were treated in the same way as in Sec. 5.2. The fraction of incoherent events was analogously extracted as $f_I = N_{\mathrm{inc}}/N_{\mathrm{coh}}$ (including dissociative events) for $p_{\mathrm{T}} < 0.2$ GeV/c and equals to 4.7% (5.0%) for the dimuon (dielectron) sample. The sample corresponding to the $\mathrm{p\bar{p}}$ channel was too small (contained roughly 60 J/ψ candidates) for the p_{T} fit to be performed, so the value of 4.7% from the muon sample was used for the protons as well since both protons and muons are just negligibly affected by bremsstrahlung radiative losses in contrast to electrons.

Due to the small yields of $\psi(2S)$ in the l^+l^- channels, both samples were merged prior to fitting the invariant mass spectrum to obtain the raw $\psi(2S)$ yield. In the four-body channels the signals were found to be clean, so the yields were calculated by simply adding up the bin

contents in the intervals around the $\psi(2S)$ mass. The incoherent contamination of the $\psi(2S)$ signal was computed as $f_I \approx 6\%$ utilizing the predicted ratio of the coherent cross sections of the J/ψ and $\psi(2S)$ photoproduction.

Similarly as before, the feed-down fraction f_D was estimated from the ratio of raw J/ψ and $\psi(2S)$ yields and the computed efficiencies from the STARlight. The value of 3.5% (4.3%) was obtained for the muon (electron) channel, respectively.

Equation (5.5) with $\varepsilon_{\text{veto}} = \varepsilon_{\text{veto}}^{\text{pileup}} \cdot \varepsilon_{\text{veto}}^{\text{EMD}}$ and appropriate branching ratios was used to calculate the coherent cross sections. For the J/ψ photoproduction, the raw yield from each channel was corrected as

$$N_{\text{J}/\psi}^{\text{coh}} = \frac{N_{\text{yield}}}{1 + f_D + f_I}\,, \tag{5.6}$$

while for the $\psi(2S)$ photoproduction the feed-down correction was irrelevant, so

$$N_{\psi(2S)}^{\text{coh}} = \frac{N_{\text{yield}}}{1 + f_I}\,. \tag{5.7}$$

For the summary of the experimental results and the discussion about various sources of systematic uncertainties refer to Tab. 1-4 in [20]. Eventually, the overall coherent cross sections of the J/ψ and $\psi(2S)$ photoproduction were calculated as weighted averages of the values from all channels using the inverse of the sum of squares of statistic and systematic errors as weights. The averaged values equal to $\mathrm{d}\sigma_{\text{J}/\psi}/\mathrm{d}y = 4.10 \pm 0.07$ (stat.) $\pm\, 0.23$ (syst.) mb and $\mathrm{d}\sigma_{\psi(2S)}/\mathrm{d}y = 0.76 \pm 0.08$ (stat.) $\pm\, 0.09$ (syst.) mb. The authors also evaluated the ratio of the coherent cross sections of the $2S$ to $1S$ charmonium states as ≈ 0.18, where most of the correlated systematic uncertainties are cancelled.

The measured rapidity dependence of the J/ψ cross section is depicted in Fig. 5.4 along with a comparison with predictions of the models. A similar plot showing the results of the $\psi(2S)$ photoproduction can be found in [20]. From Eq. (3.26), a nuclear suppression factor of ≈ 0.65 and ≈ 0.66 was calculated for J/ψ and $\psi(2S)$, respectively. These values more or less reflect the expected magnitude of the gluon shadowing at $x \sim 10^{-3}$.

One can see that the inclusion of nuclear shadowing effects is of great importance as the models neglecting possible nuclear effects (e.g. the impulse approximation or STARlight) overshoot the data across the whole range. The EPS09 LO calculation and the Leading twist approximation (LTA) by V. Guzey et al. (GKZ) agree with the data at central and forward rapidities quite well but underestimate them in the semi-forward region. The tension between the predictions and the data in the semi-forward region occurs also in the case of the the hot-spot model coupled to the Glauber-Gribov formalism (GG-HS) by J. Cepila et al. (CCK), even tough the model gives reasonable predictions in other rapidity regions. The LM model based on the IPsat parametrisation agrees with the ALICE results at semi-forward rapidities $-3 < y < -2.5$, but overshoots them in the central region by $\approx 25\%$. Bendova et al. (BCCM) presented a calculation based on the colour dipole approach and the solution to the BK equation which almost matches the data in the central region.

5.4 The $|t|$-dependence of coherent J/ψ photonuclear production

The same dataset as the one analysed in the paper [20] presented in Sec. 5.3 was exploited to measure the $|t|$-dependence of the coherent J/ψ cross section [25], where $-t$ is the square of the momentum transferred between the incoming and outgoing target nucleus. It should be recalled that the data sample was collected in Pb–Pb collisions at $\sqrt{s_{\text{NN}}} = 5.02$ TeV and its integrated

luminosity amounts to $\mathcal{L} = 233\ \mu\text{b}^{-1}$. J/$\psi$ mesons were detected at midrapidity $|y| < 0.8$ via their decay into muon pairs, probing thus the same Bjorken-x range of $x \in (0.3,\ 1.4) \cdot 10^{-3}$. As discussed in Chapter 3, the importance of this analysis lies in the fact that the two-dimensional Fourier transform of the t distribution of $\mathrm{d}\sigma/\mathrm{d}t$ is related to the gluon distribution in the impact parameter plane, so it can shed light on the spatial distribution of gluons inside the Pb nuclei.

The CCUP31 trigger class described in Sec. 4.10 was used to select events containing two back-to-back tracks. Again, in the offline analysis, the reconstructed primary vertex within ± 15 cm to the nominal interaction point in the longitudinal direction was required and the pseudorapidity of the both tracks was checked to fall within $|\eta| < 0.8$. Additional V0 and AD vetos at the offline level were applied and the total veto pileup efficiency of $\varepsilon_{\text{veto}}^{\text{pileup}} = 0.94$ was determined. The computation of the EMD efficiency correction yielded $\varepsilon_{\text{veto}}^{\text{EMD}} = 0.92$.

The identification of muon pairs was provided by the TPC measurements of the specific ionisation losses. From the events with two oppositely charged muon tracks and the reconstructed dimuon rapidity in $|y| < 0.8$, the coherent-enriched sample was defined by the selection criterion $p_{\text{T}} < 0.11$ GeV/c. Initially, the analysis was performed in six p_{T}^2 bins, which were later converted to the average $|t|$ values taking into account that the approximate relation $|t| \approx p_{\text{T}}^2$ holds for collider kinematics.

In each p_{T}^2 bin, the raw yield of J/ψ candidates was obtained by means of the invariant mass fits. The model consisted of two Crystal Ball functions which describe the J/ψ and $\psi(2S)$ signal peaks and an exponential to fit the remaining background. The well-known procedures were used to estimate the incoherent and feed-down contamination of the J/ψ yield: the fit of the transverse momentum distribution of dimuons with the invariant mass of $3.0 < m_{\mu\mu} < 3.2$ GeV/c^2 and the calculated ratio of the $\psi(2S)$ to J/ψ photoproduction cross sections coupled with estimates of the reconstruction efficiencies $(\text{Acc} \times \varepsilon)_{\text{MC}}$ from STARlight and GEANT 3.

Using the estimated corrections, the raw yield N_{yield} in each p_{T}^2 bin was corrected as

$$N_{\text{J}/\psi}^{\text{coh}} = \frac{N_{\text{yield}}}{1 + f_I + f_D} \frac{1}{(\text{Acc} \times \varepsilon)_{\text{MC}}}\,, \tag{5.8}$$

so that the numbers of coherent J/ψ candidates were obtained. In order to deal with the migration of events between different p_{T}^2 regions, an unfolding of the spectrum was performed. The double-differential cross section for the coherent J/ψ photoproduction was calculated as

$$\frac{\mathrm{d}^2\sigma_{\text{J}/\psi}^{\text{coh}}}{\mathrm{d}y\mathrm{d}p_{\text{T}}^2} = \frac{{}^{\text{unf}}N_{\text{J}/\psi}^{\text{coh}}}{\varepsilon_{\text{veto}}^{\text{pileup}} \cdot \varepsilon_{\text{veto}}^{\text{EMD}} \cdot \text{BR}(\text{J}/\psi \to \mu^+\mu^-) \cdot \mathcal{L} \cdot \Delta y \cdot \Delta p_{\text{T}}^2}\,, \tag{5.9}$$

where Δp_{T}^2 denotes the width of the p_{T}^2 interval and ${}^{\text{unf}}N_{\text{J}/\psi}^{\text{coh}}$ is the number of candidates per bin after unfolding of the results given by Eq. (5.8). The systematic uncertainties resulting from various steps in the signal extraction are summarised in Tab. 2 in [25].

Lastly, the calculated midrapidity differential cross section of the coherent J/ψ photoproduction in UPCs was converted to the photonuclear (γPb) cross section via

$$\left.\frac{\mathrm{d}^2\sigma_{\text{J}/\psi}^{\text{coh}}}{\mathrm{d}y\mathrm{d}p_{\text{T}}^2}\right|_{y=0} = 2N_{\gamma\text{Pb}}(y=0)\frac{\mathrm{d}\sigma_{\gamma\text{Pb}}}{\mathrm{d}|t|}\,, \tag{5.10}$$

where $N_{\gamma\text{Pb}}(y=0)$ is the midrapidity photon flux emitted by the Pb nuclei. However, this conversion brings additional sources of systematic uncertainties. These stem from the fact that (i) both nuclei can form the photon source, so both amplitudes have to be added and an interference

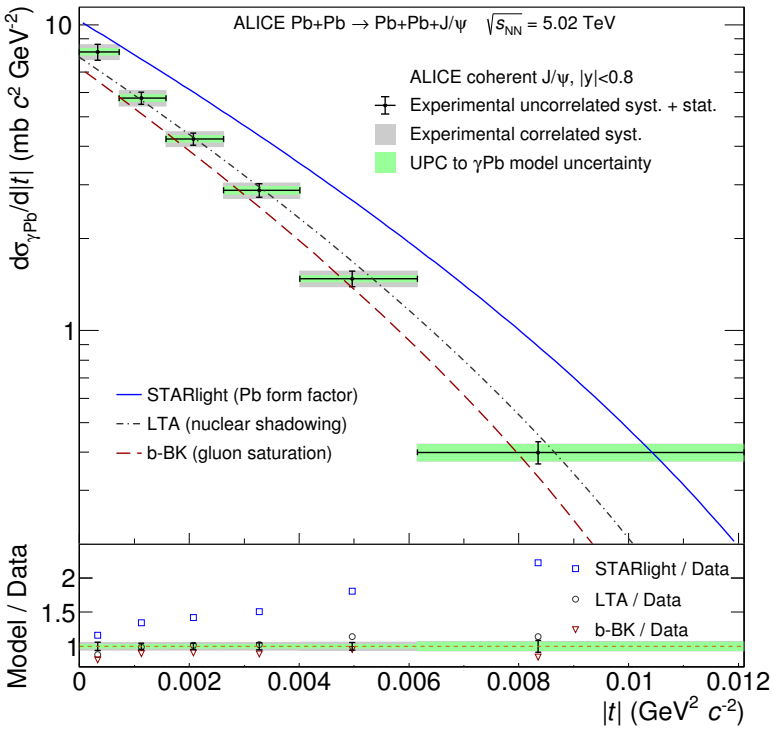

Figure 5.6: Determined $|t|$-dependence of the γPb photonuclear cross section of the coherent J/ψ photoproduction [25]. The bottom panel shows the values of a model-to-data ratio for each bin.

can occur and that (ii) the relation $|t| \approx p_{\mathrm{T}}^2$ is only approximate, so an average value of $|t|$ for each p_{T}^2 bin had to be estimated.

Ultimate results are quoted in Tab. 3 of [25]. The plotted $|t|$-dependence of the measured photonuclear cross section of the J/ψ photoproduction can be found in Fig. 5.6, where a comparison with theoretical predictions of three models is made. STARlight again overestimates the results, while the leading twist approximation including low shadowing effects and the b-BK model by Bendova et al. describe the data quite well.

Chapter 6

Analysis of Run 2 data

The analysis of the cross section of the incoherent photoproduction of J/ψ vector mesons at midrapidity with ALICE at the LHC is presented in this chapter. The first steps have been already described in the Research Project [4]. The analysis is based on the data sample that was collected in ultra-peripheral Pb–Pb collisions at the centre-of-mass energy per nucleon pair of $\sqrt{s_{\mathrm{NN}}} = 5.02$ TeV in 2018 (Run 2 of the LHC) during the operating periods LHC18q and LHC18r. This data sample was also used as an input for the midrapidity analyses in [20, 25]. The conditions were not changed between the two periods, except for the polarity of the L3 solenoid magnet, which was inverted [51].

6.1 Data sample

The list of the so-called *good runs* which meet the qualitative requirements defined for analyses in the central rapidity region was published by the ALICE DPG for the periods LHC18q [52] and LHC18r [53]. The run numbers are listed in Appendix A. The data from the first reconstruction stage, LHC18q_pass1 and LHC18r_pass1, were used in the analysis.

The measured LHC data were also supplemented with the Monte Carlo (MC) simulations of central barrel UPC events anchored to LHC18qr_pass1 [54], with the number of events simulated for each run chosen to follow the run-by-run luminosity of the CCUP31 trigger. The MC data were generated with STARlight and the datasets for the following processes (using the STARlight nomenclature) were considered in this analysis:

- kCohJpsiToMu: coherently photoproduced J/ψ decaying into $\mu^+\mu^-$,
- kIncohJpsiToMu: incoherently photoproduced J/ψ decaying into $\mu^+\mu^-$,
- kCohPsi2sToMuPi: coherently photoproduced $\psi(2S)$ decaying into J/ψ $\pi^+\pi^- \to \mu^+\mu^-$ $\pi^+\pi^-$,
- kIncohPsi2sToMuPi: incoherently photoproduced $\psi(2S)$ decaying into J/ψ $\pi^+\pi^- \to \mu^+\mu^-$ $\pi^+\pi^-$,
- kTwoGammaToMuMedium: continuum two-photon production of dimuons, $\gamma\gamma \to \mu^+\mu^-$, with the dimuon invariant masses of $1.8 < m_{\mu\mu} < 15$ GeV/c^2.

6.2 Selection of events

Because muons are significantly less affected by the radiative losses compared with electrons, which enables one to achieve a better resolution for the measured mass and transverse momentum,

it was decided that the incoherent J/ψ photoproduction will be studied in the muon decay channel, J/$\psi \to \mu^+\mu^-$. The study of the dielectron decay is thus left for potential future work. Similarly to [20], the central rapidity region was delimited by $|y| < 0.8$ and $|\eta| < 0.8$. Even though the pseudorapidity coverage of the ALICE central barrel extends up to $|\eta| = 0.9$ (corresponds to the polar angle of $\theta \approx 44.3°$ with respect to the beam axis), a slightly lower boundary of $|\eta| = 0.8$ ($\theta \approx 48.4°$) was chosen to exclude potential border effects. The analysis is sensitive to the same interval of Bjorken-x of the gluon distribution in the target as in [20], i.e. $x \in (0.3, 1.4) \cdot 10^{-3}$.

The nano-AOD events with the run number from the lists quoted in Appendix A were subjected to the following numbered list of additional selection criteria:

S0 The event contained precisely two good central tracks according to both an SPD and TPC definition. A good SPD track needs to have a cluster in both layers of the SPD detector, so the condition `HasPointOnITSLayer(0) && HasPointOnITSLayer(1)` has to be satisfied. A good TPC track is defined through `TestFilterBit(1<<5)`, see e.g. [55].

S1 The event was triggered by the `CCUP31-B-NOPF-CENTNOTRD` trigger for run numbers below 295881 and by `CCUP31-B-SPD2-CENTNOTRD` for run numbers higher than 295881 inclusive. For the definition of CCUP31 see Sec. 4.10. Here `B` stands for a beam-beam collision and `NOPF` denotes no past-future protection. Starting from the run 295881, the `SPD2` past-future protection on the six previous bunch crossings was introduced.

S2 AD offline hadronic veto (both the ADA and ADC components must be found empty in the offline processing).

S3 V0 offline hadronic veto (both the V0A and V0C components must be found empty in the offline processing).

S4 The dimuon rapidity is in the central range, $|y| < 0.8$.

S5 The pseudorapidity of both tracks is in the central range, $|\eta| < 0.8$.

S6 The tracks are oppositely charged.

S7 The tracks are more likely to be muons than electrons according to the TPC PID via measurements of the specific ionisation losses, i.e.

$$\sigma^2_{\mu,1} + \sigma^2_{\mu,2} < \sigma^2_{e,1} + \sigma^2_{e,2}\,, \tag{6.1}$$

where $\sigma_{l,i}$ is the distance, measured in standard deviations, between the energy loss due to ionisation expected for a lepton l and the real measured energy loss of the i-th track.

S8 The invariant mass $m_{\mu\mu}$ of the dimuon system is within $2.2 < m_{\mu\mu} < 4.5$ GeV/c^2.

S9 The dimuon transverse momentum $p_{\mathrm{T}} > 0.2$ GeV/c.

Table 6.1 summarises the effects of the applied selections. Via the $p_{\mathrm{T}} > 0.2$ GeV/c criterion, the so-called *incoherent-enriched sample* is defined, which is likely to contain mostly the dimuons originating from the decays of incoherent J/ψ since those are characterised by a transverse momentum of several hundreds of MeV/c, unlike the coherent J/ψ mesons. The effect of the transverse momentum selection is illustrated in Fig. 6.1, where the probability density function for a dimuon coming from the decay of a coherent or incoherent J/ψ to have p_{T} in a specific range is shown. The probability density functions were extracted from the normalised p_{T} distributions

No.	Selection	Remaining events
S0	Two good central tracks	2,502,214
S1	Central UPC CCUP31 trigger	2,277,051
S2	AD offline veto	2,241,119
S3	V0 offline veto	1,462,922
S4	The dimuon rapidity $\|y\| < 0.8$	1,417,971
S5	The pseudorapidity of both tracks $\|\eta\| < 0.8$	1,118,383
S6	Opposite charges	813,145
S7	Muon pairs only	725,979
S8	The dimuon inv. mass $2.2 < m_{\mu\mu} < 4.5$ GeV/c^2	19,478
S9	The dimuon transverse momentum $p_{\mathrm{T}} > 0.2$ GeV/c	6,941

Table 6.1: Number of events remaining after the application of selection criteria.

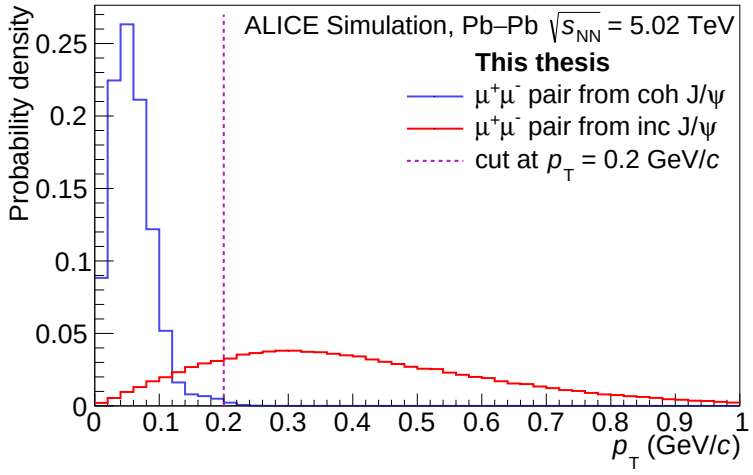

Figure 6.1: The normalised p_{T} distributions of muon pairs from the decay of coherent (blue) and incoherent (red) J/ψ mesons. The plot is based on reconstructed MC data from kCohJpsiToMu and kIncohJpsiToMu. The selections S0-S9 were applied to the data.

of *reconstructed*[1] MC events from the kCohJpsiToMu and kIncohJpsiToMu STARlight data samples after having been subjected to the selections S0-S9 above.

6.3 Incoherent cross section

The differential cross section of the incoherent J/ψ photoproduction per unit of rapidity is given by

$$\frac{\mathrm{d}\sigma^{\mathrm{inc}}_{\mathrm{J}/\psi}}{\mathrm{d}y} = \frac{N^{\mathrm{inc}}_{\mathrm{J}/\psi}}{(\mathrm{Acc}\times\varepsilon)_{\mathrm{J}/\psi}\cdot \mathrm{BR}(\mathrm{J}/\psi\to\mu^+\mu^-)\cdot\mathcal{L}\cdot\Delta y}\,, \tag{6.2}$$

[1] At the *reconstructed* level, the detector response is simulated for STARlight-generated MC events. The kinematic characteristics of reconstructed MC events (such as mass, transverse momentum etc.) thus can be "distorted" by the measurements and should imitate the real data that are measured by ALICE. It is necessary to distinguish them from MC events on the *generated* level, where the kinematic variables are not affected by the simulation of the detectors, so they correspond to the original values given by STARlight.

Process	BR [%]
$J/\psi \to \mu^+\mu^-$	5.961 ± 0.033
$\psi(2S) \to J/\psi\ \mu^+\mu^-$	34.68 ± 0.30
$\psi(2S) \to J/\psi$ neutrals	25.38 ± 0.32

Table 6.2: Branching ratios of the corresponding processes [17].

where $N^{\text{inc}}_{J/\psi}$ is the extracted number of incoherent events, $(\text{Acc} \times \varepsilon)_{J/\psi}$ is the overall acceptance and efficiency of the incoherent J/ψ reconstruction, BR is the branching ratio (see Tab. 6.2), $\mathcal{L}$ is the integrated luminosity of the analysed data sample and $\Delta y = 1.6$ the rapidity width.

From the incoherent-enriched sample, one can straightforwardly obtain the raw yield of incoherent J/ψ mesons N_{yield} by means of fitting the J/ψ signal peak in the invariant mass distribution of dimuons, which will be performed in Sec. 6.4. This number, however, has to be further corrected on the contamination from the coherent and feed-down events. Analogously to Sec. 5.1, one thus introduces the fractions f_C (f_D) of the number of coherent (feed-down) events with $p_{\text{T}} > 0.2$ GeV/c to the number of incoherent events in this p_{T} region, so that

$$N^{\text{inc}}_{J/\psi} = \frac{N_{\text{yield}}}{1 + f_C + f_D}\,. \tag{6.3}$$

In the following sections, the calculations of all the ingredients that are necessary to determine the cross section in Eq. (6.2) will be described.

6.4 Fit of the invariant mass distribution

It was expected that the J/ψ peak in the invariant mass distribution would be fitted by the Crystal Ball (CB) function [56], which consists of a Gaussian core and a stitched power-law tail below a certain threshold $-\alpha$,

$$f_{\text{CB}}(x;\mu,\sigma,\alpha,n) = N \cdot \begin{cases} A \cdot \left(B - \frac{x-\mu}{\sigma}\right)^{-n} & \text{for } \frac{x-\mu}{\sigma} < -\alpha\,, \\ \exp\left(-\frac{(x-\mu)^2}{2\sigma^2}\right) & \text{for } \frac{x-\mu}{\sigma} \geq -\alpha\,, \end{cases} \tag{6.4}$$

where

$$A = \left(\frac{n}{|\alpha|}\right)^n \exp\left(-\frac{|\alpha|^2}{2}\right)\,,$$
$$B = \frac{n}{|\alpha|} - |\alpha|\,, \tag{6.5}$$

and N is a normalisation constant. Because it is generally difficult to determine the values of the tail parameters α and n correctly from a fit to measured data, they were fixed to values obtained from a fit of the invariant mass distribution of reconstructed MC events from the kIncohJpsiToMu data sample. The same selections S0-S9 were applied to MC data prior to performing the fitting. In this case as well as in the following examples, an unbinned extended maximum likelihood fit was used.

It was found, however, that the "single-sided" CB function given by Eq. (6.4) does not describe the MC data properly, as can be seen in Fig. 6.2a (left). In the centre of the mass peak, the values are clearly underestimated, which could not be solved by simply optimizing the parameters of the CB function. Looking at the same plot with a logarithmic scale on the vertical

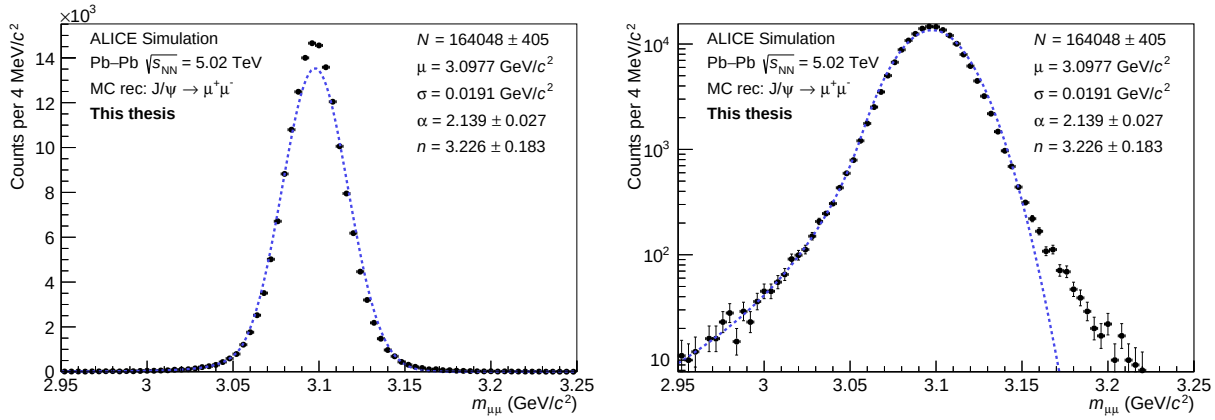

(a) Fit using the single-sided CB function, Eq. (6.4).

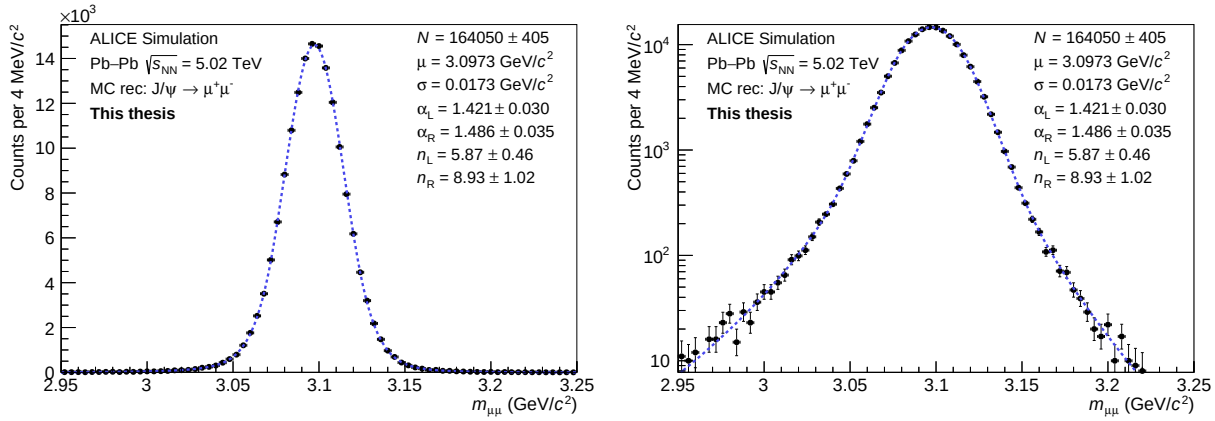

(b) Fit using the double-sided CB function, Eq. (6.6).

Figure 6.2: The fitted invariant mass distribution of reconstructed MC data from the kIncohJpsiToMu sample with the applied selections S0-S9. The plots on the right are in the log vertical scale. The errors of σ and μ are not shown as they were found to be negligibly small, $< 1\%$.

axis, see Fig. 6.2a (right), one may notice that the poor behaviour near the top in fact stems from the incompatibility with the data in the region of $m_{\mu\mu} \gtrsim 3.15$ GeV/c^2. Clearly, the addition of a power-law high-end tail is crucial to obtain a satisfactory agreement with the data. The same behaviour was observed in fits to MC data from the kCohJpsiToMu sample (not shown) or to combined data samples (see Fig. 6.4a).

A straightforward generalisation of Eq. (6.4) is referred to as the double-sided Crystall Ball (DSCB) function,

$$f_{\mathrm{DSCB}}(x;\mu,\sigma,\alpha_L,n_L,\alpha_R,n_R) = N \cdot \begin{cases} A_L \cdot \left(B_L - \frac{x-\mu}{\sigma}\right)^{-n_L} & \text{for } \frac{x-\mu}{\sigma} < -\alpha_L\,, \\ \exp\left(-\frac{(x-\mu)^2}{2\sigma^2}\right) & \text{for } -\alpha_L \le \frac{x-\mu}{\sigma} \le \alpha_R\,, \\ A_R \cdot \left(B_R - \frac{x-\mu}{\sigma}\right)^{-n_R} & \text{for } \frac{x-\mu}{\sigma} > \alpha_R\,, \end{cases} \tag{6.6}$$

where the left and right parameters A, B are defined analogously to Eq. (6.5). Using the DSCB function to fit the incoherent MC data sample, one may notice a significant improvement, see Fig. 6.2b. The same improvement was observed in the fit to combined MC sample, see Fig. 6.4b. It was thus decided to use the DSCB functions to fit the J/ψ invariant mass peaks within this analysis.

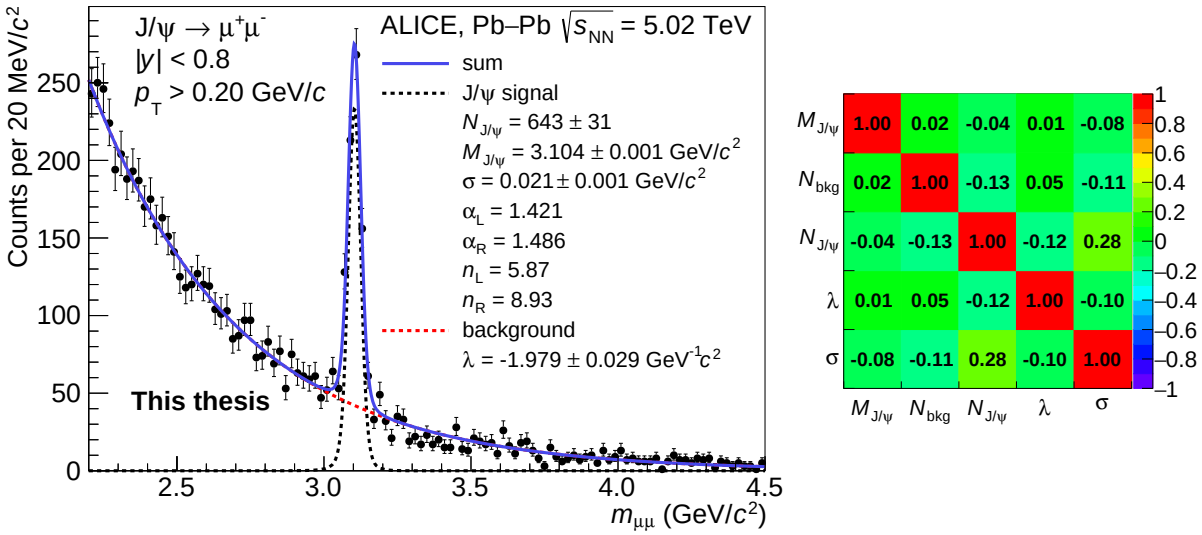

Figure 6.3: Fit of the invariant mass distribution of dimuons from the incoherent-enriched sample. The correlation matrix is shown in the right panel.

The fit of the invariant mass distribution of the incoherent-enriched sample can be found in Fig. 6.3. A sum of an exponential function $e^{\lambda m_{\mu\mu}}$ to account for the background and the DSCB function with the tail parameters α_R, α_L, n_R and n_L fixed to MC values was used as a template. The contribution from the $\psi(2S)$ vector meson was found to be negligible, the signal near $M_{\psi(2S)} = 3.686$ GeV/c^2 [17] hardly exceeds statistical fluctuations, so the corresponding $\psi(2S)$ peak was excluded from the model. The fitting was thus performed with five free parameters, the normalisation of the J/ψ peak $N_{\mathrm{J}/\psi}$, the J/ψ mass $M_{\mathrm{J}/\psi}$, the resolution σ, the total number of background events N_{bkg}, and the background slope λ. By comparing Fig. 6.3 with e.g. Fig. 5.5 (left), one can say that the midrapidity incoherent-enriched sample is more affected by low-mass continuum, which is reflected in the relatively high absolute value of the exponential slope, $\lambda \simeq -2$.

The raw yield of J/ψ candidates, $N_{\mathrm{yield}} = 643 \pm 31$, was then obtained by integrating the fitted CB function in the range $m_{\mu\mu} \in (3.0, 3.2)$ GeV/c^2. It is clear the yield is about seven times higher than the Run 1 result for the muon channel, see Tab. 5.1b. This means that the reduction of statistical errors can be achieved and one can perform more detailed analysis devoted to the sources of systematic uncertainties.

For the purposes which will be clarified later on, the fit of the invariant mass distribution of the data with the modified p_{T} selection (S9) to $0 < p_{\mathrm{T}} < 2$ GeV/c will be needed. Fitting was done in a complete analogy with the above-described method, the tail parameters were fixed to values obtained in the fit of MC data from the merged kCohJpsiToMu and kIncohJpsiToMu samples after the selections S0-S8 and $0 < p_{\mathrm{T}} < 2$ GeV/c had been applied, see Fig. 6.4b. The result is presented in Fig. 6.5.

6.5 Acceptance and efficiency

The overall acceptance and efficiency of the signal reconstruction, $(\mathrm{Acc} \times \varepsilon)_{\mathrm{J}/\psi}$, appearing in Eq. (6.2) may be written as a product

$$(\mathrm{Acc} \times \varepsilon)_{\mathrm{J}/\psi} = (\mathrm{Acc} \times \varepsilon)_{\mathrm{MC}} \cdot \varepsilon_{\mathrm{veto}} \,, \tag{6.7}$$

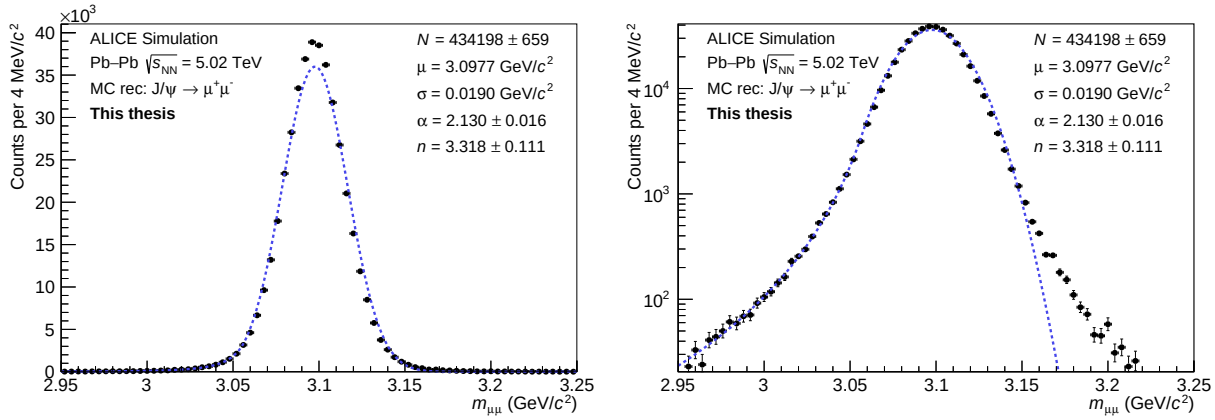

(a) Fit using the single-sided CB function, Eq. (6.4).

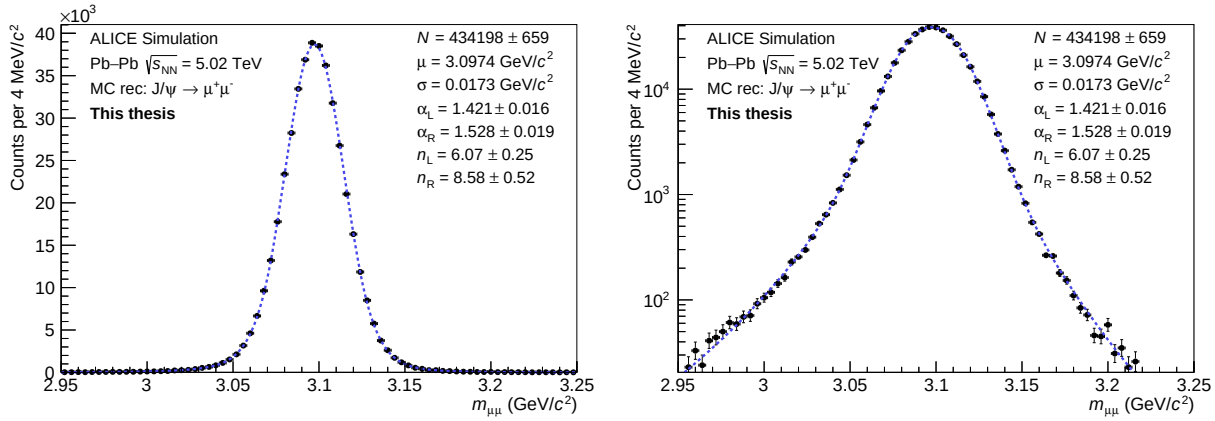

(b) Fit using the double-sided CB function, Eq. (6.6).

Figure 6.4: The fitted invariant mass distribution of reconstructed MC data from the merged kCohJpsiToMu and kIncohJpsiToMu samples with the applied selections S0-S8 and $0 < p_T < 2.0$ GeV/c. The plots on the right are in the vertical log scale. The errors of σ and μ are not shown as they were found to be negligibly small, $< 1\%$.

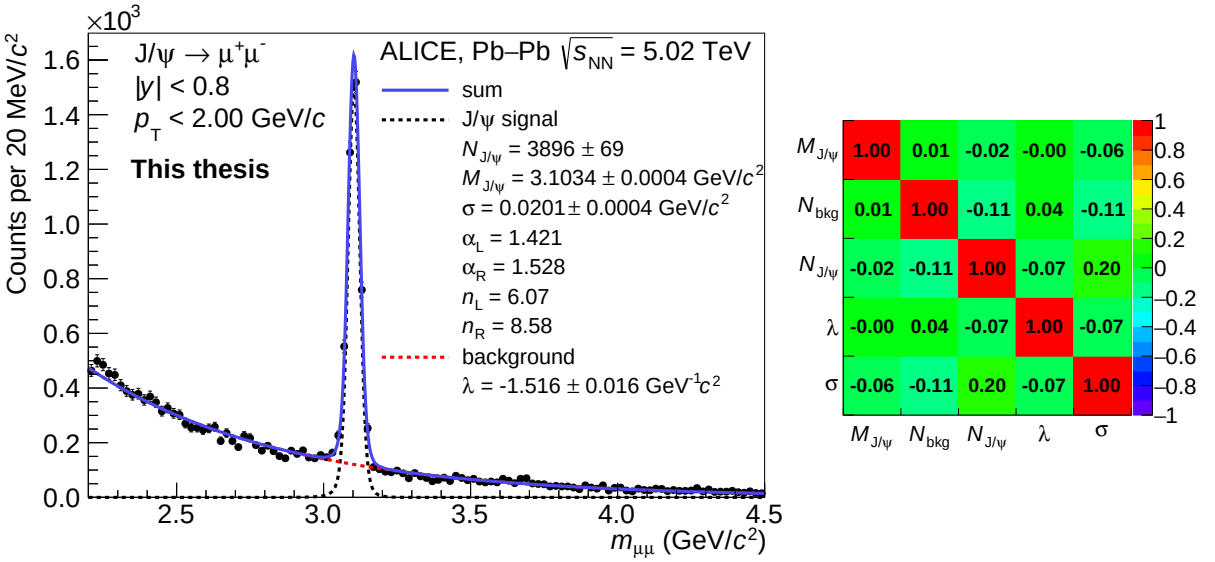

Figure 6.5: Fit of the invariant mass distribution of dimuons from the sample defined by the selections S0-S8 and $0 < p_T < 2.0$ GeV/c. The correlation matrix is shown in the right panel.

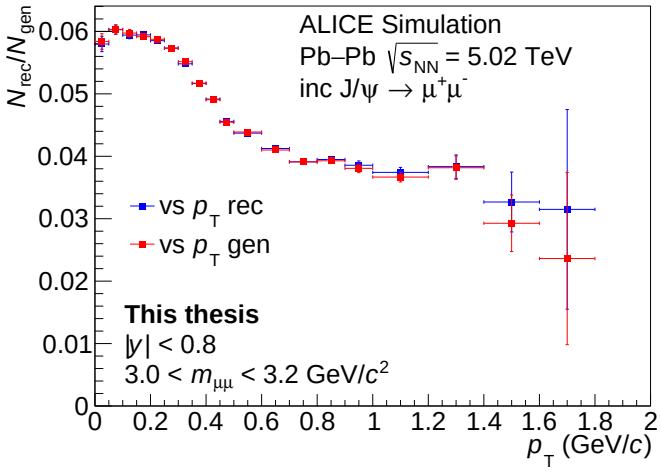

Figure 6.6: The dependence of $(\mathrm{Acc} \times \varepsilon)_{\mathrm{MC}}$ on the reconstructed (blue) and generated (red) transverse momentum of dimuons from the kIncohJpsiToMu sample.

where $\varepsilon_{\mathrm{veto}}$ is the part compensating for AD and V0 vetoes, which was discussed in Chapter 5, and $(\mathrm{Acc} \times \varepsilon)_{\mathrm{MC}}$ can be estimated using simulated MC data from STARlight as a ratio

$$(\mathrm{Acc} \times \varepsilon)_{\mathrm{MC}} = \frac{N_{\mathrm{rec}}(\text{selections S0-S9})}{N_{\mathrm{gen}}(|y| < 0.8)} \,. \tag{6.8}$$

In the nominator, one inserts the number of reconstructed MC events passing the same set of selection criteria as the real data, S0-S9. It is important to note, however, that the S8 selection must be modified to $3.0 < m_{\mu\mu} < 3.2$ GeV/c^2 to account for the invariant mass range that is used to calculate the raw yield of J/ψ candidates when integrating the CB function, which effectively represents a stricter selection criterion than the original S8 selection, $2.2 < m_{\mu\mu} < 4.5$ GeV/c^2, even though its effect on MC data is negligible. This version of the S8 selection is considered in the rest of this chapter wherever the acceptance and efficiency corrections are calculated. In the denominator of Eq. (6.8), one puts the number of MC events at the generated level, for which the J/ψ rapidity falls within $|y| < 0.8$. To calculate the numbers N_{rec} and N_{gen}, the kIncohJpsiToMu data sample was used.

In this sense, $(\mathrm{Acc} \times \varepsilon)_{\mathrm{MC}}$ also covers the efficiency of the CCUP31 trigger, because the trigger is included in the S1 selection.

The corresponding numbers were found to be $N_{\mathrm{rec}} = 163{,}368$, $N_{\mathrm{gen}} = 4{,}009{,}786$. Estimating the statistical errors from the Poisson distribution as $\sqrt{N}$, where N is the number of events, the overall value of the MC acceptance and efficiency can be determined as $(\mathrm{Acc} \times \varepsilon)_{\mathrm{MC}} = 0.0407 \pm 0.0001 = (4.07 \pm 0.01)\%$, where the relative uncertainty of the result was determined by taking the square root of the relative errors of N_{rec} and N_{gen} added in quadrature.

Furthermore, the dependence of $(\mathrm{Acc} \times \varepsilon)_{\mathrm{MC}}$ on the transverse momentum of dimuons was investigated in the region of $p_{\mathrm{T}} \in (0, 2)$ GeV/c, which was divided into 20 bins. Eq. (6.8) was modified as follows:

- in N_{rec}, the selection criterion S9 was modified to require that p_{T} falls within the bin range,
- in N_{gen}, the same condition was added to $|y| < 0.8$, i.e. p_{T} of the generated event falls within the bin range.

In each bin, the acceptance and efficiency was then calculated as the ratio of these two numbers. The result is depicted in Fig. 6.6. Here, in addition, one can make a comparison between two

cases: (i) when the reconstructed p_{T} value is used in the transverse momentum selection in N_{rec} (blue histogram) and (ii) when the generated p_{T} value is used to find N_{rec} per each bin (red histogram). This comparison was made to look for a possible distortion of the spectra during the simulations of detector response that could be caused by a massive migration of events between the p_{T} bins.

One can say that both shapes agree very well within the uncertainties, so only the reconstructed value of p_{T} will be considered when computing N_{rec} in the further discussion. The large statistical uncertainties in the high-p_{T} region are caused by limited statistics (the p_{T} spectrum of dimuons from kIncohJpsiToMu vanishes in this region). In the last p_{T} bin, the N_{rec} is zero in both cases.

It was further studied what the source of the observed p_{T}-dependence of the MC acceptance and efficiency was. First, only the modified S9 selection (p_{T} of the dimuon within the bin range) was applied to data, see Fig. 6.8a, which resulted in a roughly flat dependence. Thus, the ratios of the number of events passing the S9 selection and the i-th selection Si, $N_{\mathrm{rec}}[\mathrm{S9} + \mathrm{S}i]$, to the number of events passing the S9 selection only, $N_{\mathrm{rec}}[\mathrm{S9}]$, were calculated in all bins. The results can be found in Fig. 6.7, where one may notice that the dominant source of the observed p_{T}-dependence of the overall acceptance and efficiency might be the S1 selection criterion, i.e. the CCUP31 trigger. The other selections do not introduce p_{T}-dependence that would be worth highlighting here.

This surmise was indeed confirmed by plotting the p_{T}-dependence of $N_{\mathrm{rec}}/N_{\mathrm{gen}}$ when only the S1 and S9 selections were considered on the reconstructed level, refer to Fig. 6.8b. The observed shape almost matches the dependence observed in Fig. 6.6, except for a higher overall normalisation, which can be explained by the absence of other selection criteria (especially the S5 selection, according to Fig. 6.7). Now, one can look for the definition of the CCUP31 trigger in Sec. 4.10. It had been checked that the hadronic AD and V0 vetoes have a negligible effect on the MC data, so one was left with just two remaining conditions of the trigger, the SPD topological condition, 0STG, and the TOF topological requirement, 0OMU. 0STG was again excluded by observing an approximately flat shape when only the S9 and 0STG selections were included, see Fig. 6.8c. Eventually, Fig. 6.8d shows that the 0OMU condition is indeed causing the observed p_{T}-dependence of the overall MC acceptance and efficiency.

This observation can be explained as follows. Due to momentum conservation, the muon tracks produced at $p_{\mathrm{T}} \approx 0$ are back-to-back in azimuth and their momentum is large enough to ensure the curvature of the tracks in the magnetic field is not too significant. A large azimuthal opening angle, $\Delta\phi \approx 180°$, is therefore maintained when the tracks reach the TOF detector and such events are likely to fulfil the trigger condition imposed by TOF. On the other hand, at larger p_{T}, the opening angle in azimuth $\Delta\phi$ decreases and the topological condition is satisfied less frequently.

6.6 Feed-down contamination

In this section, one of the possible ways to determine the f_D fraction entering Eq. (6.2) is described. As has been already stated in Sec. 5.1, in feed-down reactions $\psi(2S) \to \mathrm{J}/\psi + X$ (undetected), the J/ψ is most often accompanied by a pair of charged pions or by neutral particles (e.g. a pair of neutral pions). The branching ratios of these two types of processes are quoted in Tab. 6.2.

However, one also has to take into account that the primary $\psi(2S)$ can be itself photoproduced both coherently or incoherently. Thus, the overall f_D fraction must be decomposed as a

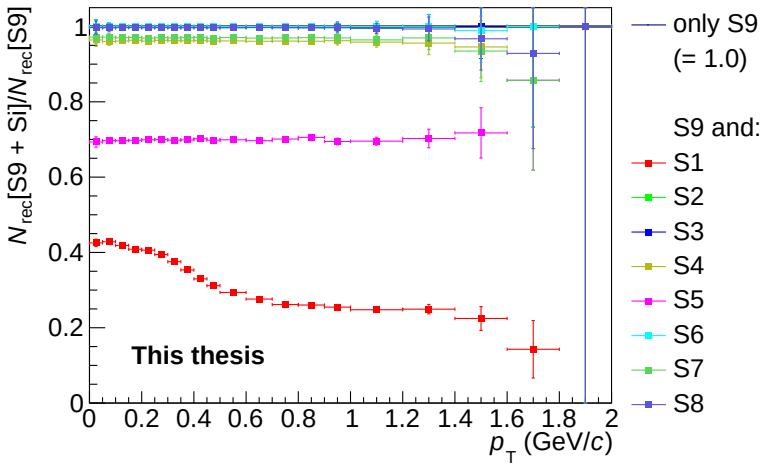

Figure 6.7: The ratio of the number of events per bin passing the S9 selection and the i-th selection Si, $N_{\mathrm{rec}}[\mathrm{S9} + \mathrm{S}i]$, to the number of events per bin passing the S9 selection only, $N_{\mathrm{rec}}[\mathrm{S9}]$.

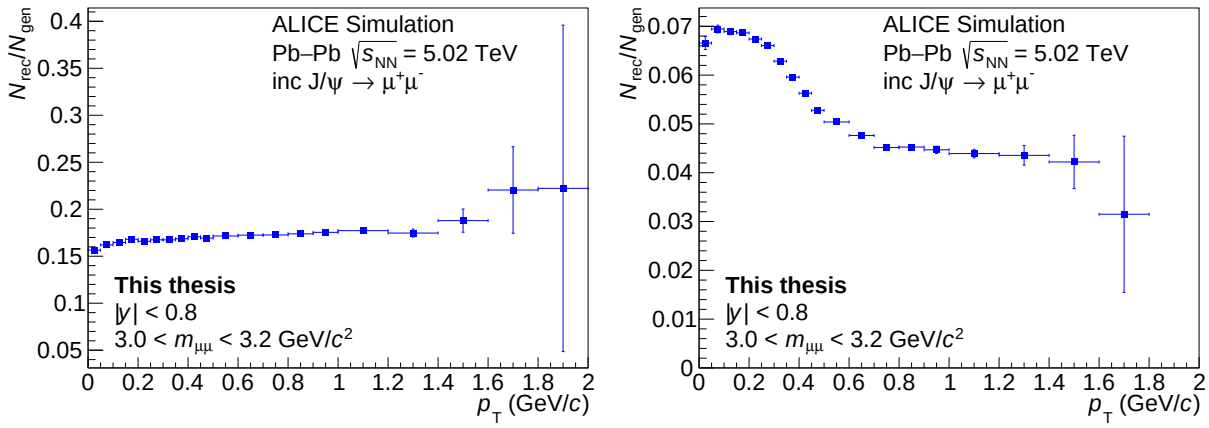

(a) S9 only

(b) S1 and S9

(c) 0STG and S9

(d) 0OMU and S9

Figure 6.8: The p_{T} dependences of the ratio of the number of reconstructed events passing the corresponding selections, N_{rec}, to the number of generated events N_{gen} with $|y| < 0.8$ and the corresponding p_{T}.

$\sigma(\|y\| < 1)$	Coherent [mb]	Incoherent [mb]
J/ψ	12.504	5.247
$\psi(2S)$	2.52	0.92

Table 6.3: STARlight-predicted cross sections of the J/ψ and $\psi(2S)$ photoproduction at midrapidity, integrated over the range $|y| < 1$.

sum of the following contributions,

$$f_D = f_D^{\mathrm{coh,ch}} + f_D^{\mathrm{coh,n}} + f_D^{\mathrm{inc,ch}} + f_D^{\mathrm{inc,n}}\,, \tag{6.9}$$

where the superscripts denote whether the feed-down process was coherent or incoherent and if it was accompanied by a charged pion pair or by neutral particles.

Each of these fractions was calculated via the following method. Consider e.g. $f_D^{\mathrm{coh,ch}}$, which can be written as a ratio of the number of coherently photoproduced $\psi(2S)$ mesons which decayed into $J/\psi + \pi^+\pi^-$, i.e. $N^{\mathrm{coh}}_{\psi(2S)\to J/\psi}$, to the number of incoherently photoproduced J/ψ mesons, $N^{\mathrm{inc}}_{J/\psi}$. Both numbers are considered within the incoherent-enriched sample. Then one may write

$$\begin{aligned} f_D^{\mathrm{coh,ch}} &= \frac{N^{\mathrm{coh}}_{\psi(2S)\to J/\psi}}{N^{\mathrm{inc}}_{J/\psi}} \\ &= \frac{\sigma^{\mathrm{coh}}_{\psi(2S)}(|y| < y_0)}{\sigma^{\mathrm{inc}}_{J/\psi}(|y| < y_0)} \, \frac{(\mathrm{Acc}\times\varepsilon)_{\psi(2S)\to J/\psi}}{(\mathrm{Acc}\times\varepsilon)_{J/\psi}} \\ &\times \frac{\mathrm{BR}(J/\psi \to \mu^+\mu^-)\ \mathrm{BR}(\psi(2S) \to J/\psi + \pi^+\pi^-)}{\mathrm{BR}(J/\psi \to \mu^+\mu^-)} \, \frac{\mathcal{L}}{\mathcal{L}} \\ &= \frac{\sigma^{\mathrm{coh}}_{\psi(2S)}(|y| < y_0)}{\sigma^{\mathrm{inc}}_{J/\psi}(|y| < y_0)} \, \frac{(\mathrm{Acc}\times\varepsilon)_{\psi(2S)\to J/\psi}}{(\mathrm{Acc}\times\varepsilon)_{J/\psi}} \, \mathrm{BR}(\psi(2S) \to J/\psi + \pi^+\pi^-)\,, \end{aligned} \tag{6.10}$$

where in the second step, $N^{\mathrm{inc}}_{J/\psi}$ was expressed in terms of other variables from Eq. (6.2) and an analogous relation was used for $N^{\mathrm{coh}}_{\psi(2S)\to J/\psi}$, assuming the data samples of the same integrated luminosities. Then the identical terms were cancelled.

The cross sections of the coherent $\psi(2S)$ and incoherent J/ψ photoproduction integrated over the midrapidity interval $(-y_0, y_0)$ must be provided. One option is to relate the ratio of these cross sections to the ratio of the measured raw yields of J/ψ and $\psi(2S)$ mesons from the invariant mass fit as was done for instance in [49]. This method is, however, not applicable in this analysis due to the absence of the measured yield of $\psi(2S)$. Instead, the values predicted by STARlight for $y_0 = 1$ were used, which can be found in Tab. 6.3.

The acceptance and efficiency appearing in the denominator of Eq. (6.10) is the overall value of $(\mathrm{Acc}\times\varepsilon)_{\mathrm{MC}} \approx 0.0407$, which was computed in the previous section. The acceptance and efficiency from the nominator was calculated in an analogous way, i.e. using Eq. (6.8), except that the kCohPsi2sToMuPi was used as the input sample of MC data.

Similarly, in order to determine the $f_D^{\mathrm{inc,ch}}$ correction, the kIncohPsi2sToMuPi sample was considered. In the case of neutral fractions, the situation was different because the simulations corresponding to neutral feed-down processes, $\psi(2S) \to J/\psi + \mathrm{neutrals}$, were not provided by STARlight. Instead, the spectra of J/ψ candidates from such processes were simulated using the kCohPsi2sToMuPi and kIncohPsi2sToMuPi data samples and *skipping the pion tracks* when

	Coh $(\mathrm{Acc} \times \varepsilon)_{\psi(2S)\to \mathrm{J}/\psi}$	Inc $(\mathrm{Acc} \times \varepsilon)_{\psi(2S)\to \mathrm{J}/\psi}$
MC dataset	kCohPsi2sToMuPi	kIncohPsi2sToMuPi
Neutral	$(2.785 \pm 0.097)\%$	$(4.274 \pm 0.012)\%$
Charged	$(0.875 \pm 0.005)\%$	$(1.440 \pm 0.007)\%$

Table 6.4: Values of acceptance and efficiency corrections for different feed-down channels determined from the STARlight MC samples.

f_D [%]	Coherent	Incoherent
Neutral	8.34 ± 0.11	4.67 ± 0.06
Charged	3.58 ± 0.04	2.15 ± 0.02

Table 6.5: Calculated feed-down corrections for different channels.

reconstructing the events. This reflects the fact that neutral particles cannot be directly measured by the ALICE detectors involved in this analysis.

The calculated values of $(\mathrm{Acc} \times \varepsilon)$ are quoted in Tab. 6.4 for all feed-down channels. Inserting these values into Eq. (6.10), together with the STARlight cross sections from Tab. 6.3 and the branching ratios from Tab. 6.2, one can calculate the feed-down fractions for all four channels. These results can be found in Tab. 6.5. The total coherent correction is thus $f_D^{\mathrm{coh}} = (11.92 \pm 0.12)\%$, while the overall incoherent fration equals $f_D^{\mathrm{inc}} = (6.82 \pm 0.06)\%$. The errors of $(\mathrm{Acc} \times \varepsilon)$ and of the branching ratios were added in quadrature. Eventually, the overall f_D fraction given by Eq. (6.9) was obtained summing all contributions, i.e. $f_D = (18.74 \pm 0.13)\%$.

At first glance, it might seem surprising that the contribution from the feed-down from the coherent $\psi(2S)$ is almost twice as high as the incoherent feed-down contribution, even though one works within the incoherent-enriched sample, where $p_{\mathrm{T}} > 0.2$ GeV/c. In fact, this can be explained by taking into account the following observations. First, the transverse momentum distribution of muon pairs originating from the coherent feed-down process is considerably broader than the p_{T} distribution of dimuons from the decays of primary J/ψ mesons, compare Fig. 6.1 with Fig. 6.9. Second, according to STARlight, the cross section of the incoherent $\psi(2S)$ photoproduction is more than $\approx 60\%$ lower than that of the coherent $\psi(2S)$ photoproduction. Consequently, the raw yield N_{yield} from the incoherent-enriched sample is more affected by the coherent feed-down reactions.

6.7 Coherent contamination

Similarly to the analyses presented in Chapter 5, the fraction f_C describing the coherent contamination of N_{yield} was determined by means of the fit of the transverse momentum distribution. For these purposes, the invariant mass selection S8 was replaced by $3.0 < m_{\mu\mu} < 3.2$ GeV/c^2, in order to select the events from the J/ψ mass peak region. The transverse momentum selection S9 was also modified to $0 < p_{\mathrm{T}} < 2$ GeV/c. The obtained data sample contained 5097 events. The fitted p_{T} spectrum of these events is depicted in Fig. 6.10. The model consists of six distinct contributions:

- coherent J/ψ photoproduction (kCohJpsiToMu),
- incoherent J/ψ photoproduction (kIncohJpsiToMu),

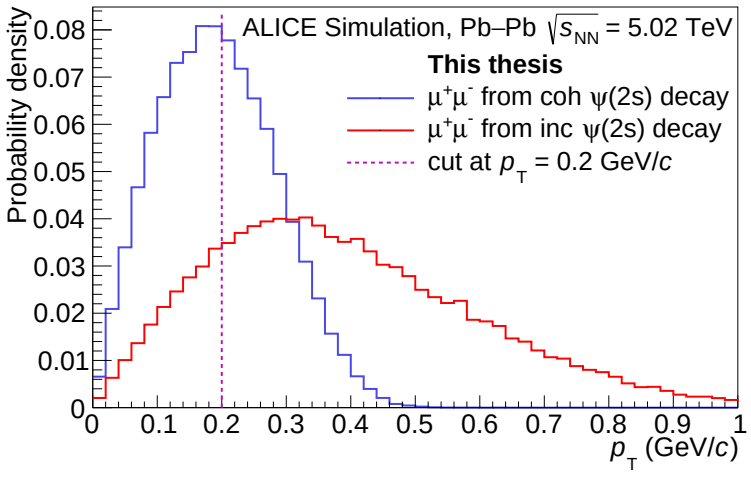

Figure 6.9: The normalised p_{T} distributions of muon pairs from the decay of coherent (blue) and incoherent (red) $\psi(2S)$ mesons into $\mu^+\mu^-$ $\pi^+\pi^-$. The plot is based on reconstructed MC data from kCohPsi2sToMuPi and kIncohPsi2sToMuPi. The selections S0-S9 were applied to the data.

- J/ψ from the decay of coherent $\psi(2S)$ (kCohPsi2sToMuPi),
- J/ψ from the decay of incoherent $\psi(2S)$ (kIncohPsi2sToMuPi),
- background processes $\gamma\gamma \to \mu^+\mu^-$ (kTwoGammaToMuMedium) and
- incoherent J/ψ photoproduction accompanied with nucleon dissociation.

The templates for the first five processes were (by default) taken from STARlight as normalised histograms showing the p_{T} distribution of dimuons from the corresponding STARlight samples, names of which are quoted in the brackets. First, the MC events were subjected to the same selection criteria as the real data, i.e. the selections S0-S9 with the last two selections modified as mentioned above. For the dissociative J/ψ photoproduction, the H1 parametrisation [50] was again used, see Eq. (5.4), with the "high-energy" coefficients $b_{\mathrm{pd}} = 1.79$ (GeV/c)$^{-2}$ and $n_{\mathrm{pd}} = 3.58$.

Fitting was performed with the following free parameters: the number of coherent events, N_{coh}, the number of incoherent events, N_{inc}, and the number of dissociative events, N_{diss}. The normalisation of the background template was fixed to $N_{\mathrm{bkg}} = 1215$, where 1215 ± 10 was extracted from the results shown in Fig. 6.5 as the number of background events with $3.0 < m_{\mu\mu} < 3.2$ GeV/c^2.

The feed-down contributions were constrained to the normalisations of the primary photoproduction processes through $N^{\text{f-d}}_{\mathrm{coh}} = f_D^{\mathrm{coh}} \times N_{\mathrm{coh}}$ and $N^{\text{f-d}}_{\mathrm{inc}} = f_D^{\mathrm{inc}} \times N_{\mathrm{inc}}$. Here, the f_D fractions were calculated analogously as in Sec. 6.6, but when calculating the corresponding values of $(\mathrm{Acc} \times \varepsilon)_{\mathrm{MC}}$ through Eq. 6.8, one had to consider the modified versions of the S8 and S9 selections. Also, since f_D^{coh} now relates the number of coherent feed-down events to N_{coh} (not N_{inc}), the acceptance and efficiency appearing in the denominator of Eq. (6.10) had to be determined from the kCohJpsiToMu sample and the STARlight cross section for $\sigma^{\mathrm{coh}}_{\mathrm{J}/\psi}(|y| < 1)$ had to be used. The suggested procedure yielded $f_D^{\mathrm{coh}} = (7.14 \pm 0.07)\%$ and $f_D^{\mathrm{inc}} = (6.92 \pm 0.07)\%$.

The f_C correction was then calculated from the fitted templates as a ratio of

$$f_C = \frac{N_{\mathrm{coh}}}{N_{\mathrm{inc}} + N_{\mathrm{diss}}} = (0.93 \pm 0.07)\%\,, \tag{6.11}$$

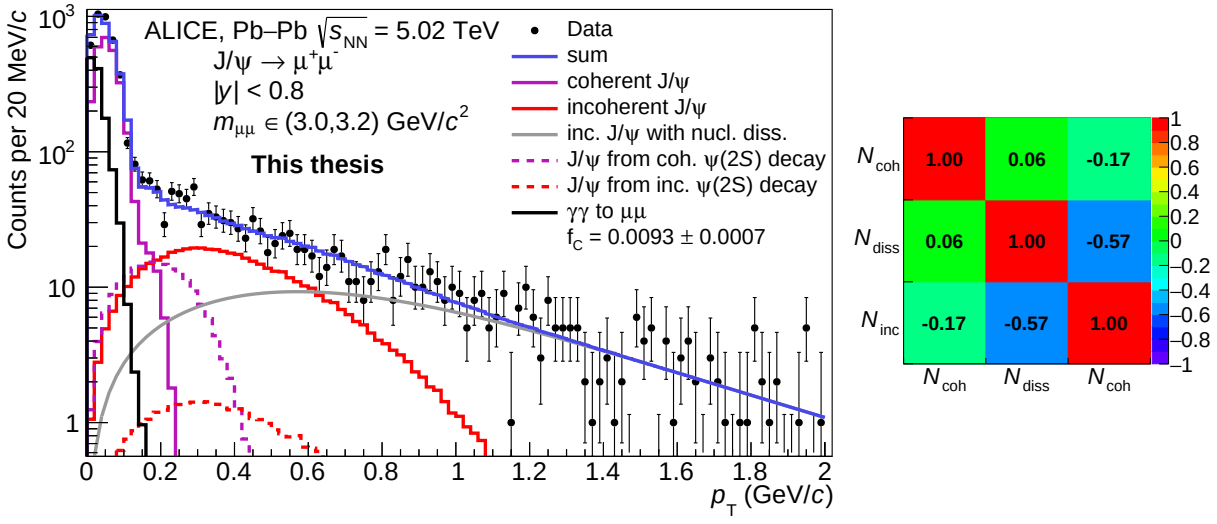

Figure 6.10: Fit of the transverse momentum distribution of measured events with $3.0 < m_{\mu\mu} < 3.2$ GeV/c^2 and $|y| < 0.8$. The shape of the background $\gamma\gamma \to \mu\mu$ was taken from STARlight.

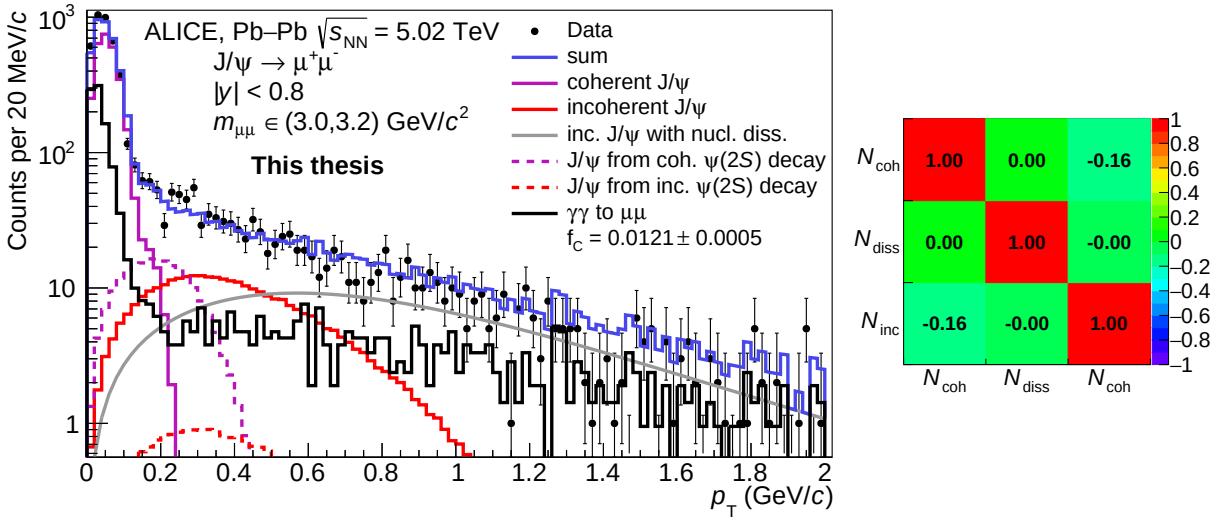

Figure 6.11: Fit of the transverse momentum distribution of measured events with $3.0 < m_{\mu\mu} < 3.2$ GeV/c^2 and $|y| < 0.8$. The shape of the background $\gamma\gamma \to \mu\mu$ was taken from the side band, see the text for the details.

where all the numbers were calculated within the incoherent-enriched sample, i.e. N_{coh} denotes the number of primary coherent J/ψ events with $p_{\mathrm{T}} > 0.2$ GeV/c and the other variables are defined analogously.

However, the main drawback of the procedure described above is that the background template from STARlight does not describe the data properly because it does not take into account high-p_{T} dimuons that originate from incoherently emitted photons. Thus, an alternative option was studied, where the template for continuum events was created from the p_{T} distribution of dimuons from the so-called side band of the measured invariant mass distribution of J/ψ events with $p_{\mathrm{T}} \in (0,\, 2)$ GeV/c. This means that the events with $3.3 < m_{\mu\mu} < 4.5$ GeV/c^2 from Fig. 6.5 were used.

No other modifications were made, so the background normalisation was again fixed to $N_{\mathrm{bkg}} = 1215$ and the fit was performed in the same way as before. The result can be found in Fig. 6.11 and the calculated coherent fraction is slightly higher, $f_C = (1.21 \pm 0.05)\%$. The increase in f_C was expected, as the inclusion of high-p_{T} background mostly affected the total number of incoherent events with $p_{\mathrm{T}} > 0.2$ GeV/c (including the dissociative contribution), $N_{\mathrm{inc}} + N_{\mathrm{diss}}$, which was reduced by $\approx 18\%$. The differences in the values of f_C, depending on which precedure was followed to perform the fit of the transverse momentum distribution, will be in the future considered as one of the sources of systematic errors.

6.8 Integrated luminosity of the sample

This section summarises the method which was employed to measure the "size" of the analysed data sample, which is expressed in terms of the integrated luminosity $\mathcal{L}$.

The total integrated luminosity recorded by ALICE in Pb–Pb collisions at $\sqrt{s_{\mathrm{NN}}} = 5.02$ TeV was determined by measuring the cross sections of reference processes (based on the detection of particles by the V0 and ZDC detectors), which were calculated in the van der Meer scans [57].

In this analysis, the so-called trending files [58] were used, where the recorded luminosities per run are stored together with the recorded numbers of events N_{rec} that were fired by the corresponding trigger (in this case CCUP31) in each run. The analysed luminosity per run is then obtained by scaling the recorded values by the ratio $N_{\mathrm{ana}}/N_{\mathrm{rec}}$, where N_{ana} is the number of CCUP31-trigerred events per run that were accessed in this analysis. Due to various computational errors that may occur during the processing of large data samples on Grid, N_{ana} is likely to be at least slightly lower than N_{rec} in most of the runs.

The results are shown in Fig. 6.12 and 6.13 for both analysed periods separately. The total recorded luminosity of the CCUP31 trigger in the periods LHC18q and LHC18r was measured as 245.634 $\mu\mathrm{b}^{-1}$. The integrated luminosity of the analysed data sample amounts to $\mathcal{L} = 238.723\ \mu\mathrm{b}^{-1}$, about 97% of the former value.

6.9 First estimate of the incoherent cross section

The summary of all presented results can be found in Tab. 6.6. Only statistical errors of the variables (and the uncertainties related to the branching ratios from [17]) were considered in this thesis. A thorough analysis devoted to various sources of systematic uncertainties is left for future work and is intended to be performed during the doctoral studies.

Based on the quoted results, one can make a preliminary estimate of the cross section of the incoherent J/ψ photoproduction. The veto efficiency, $\varepsilon_{\mathrm{veto}}$, was not calculated within this work, however, at the current level of the analysis, one may borrow the values that were

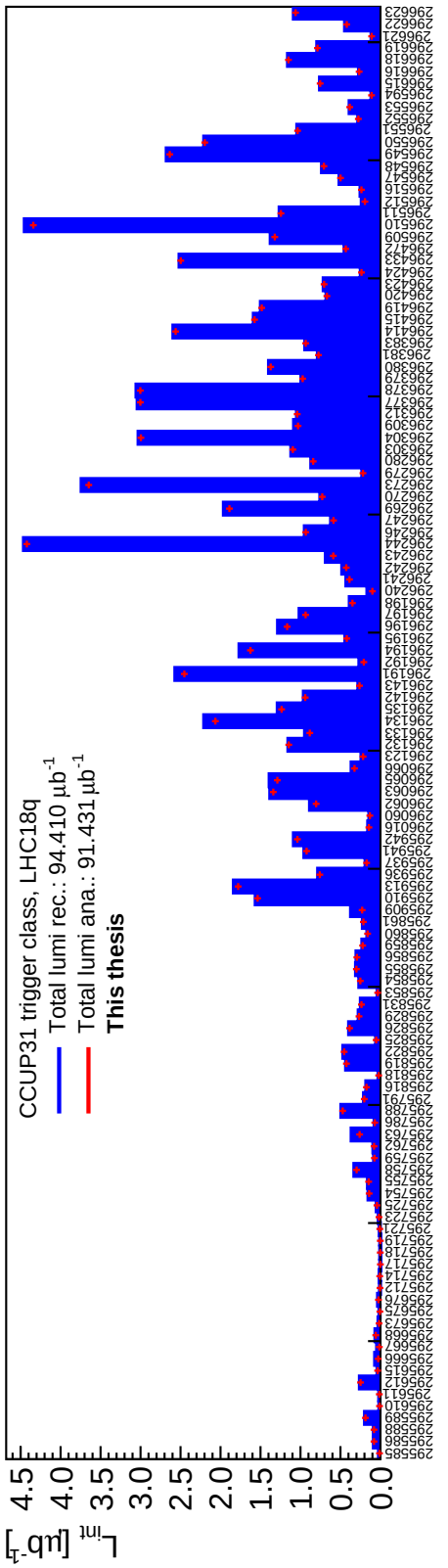

Figure 6.12: Integrated luminosity $\mathcal{L}$ of the CCUP31 trigger class per run in the period LHC18q. Blue columns indicate recorded values while red crosses correspond to the values analysed in this study.

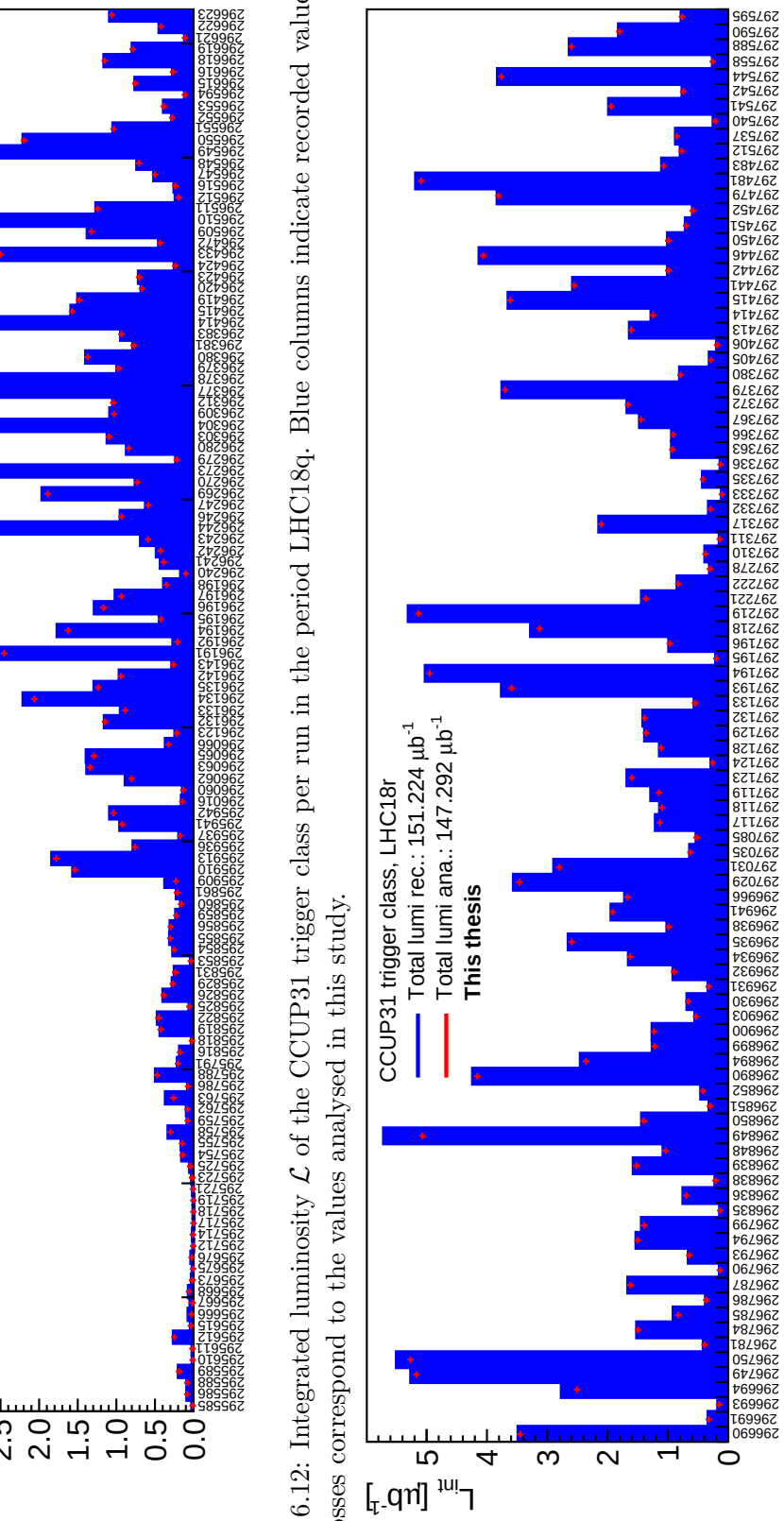

Figure 6.13: Integrated luminosity $\mathcal{L}$ of the CCUP31 trigger class per run in the period LHC18r. Blue columns indicate recorded values while red crosses correspond to the values analysed in this study.

Variable	Calculated value
N_{yield}	643 ± 31
$(\text{Acc} \times \varepsilon)_{\text{MC}}$	$(4.07 \pm 0.01)\%$
f_C	$(0.93 \pm 0.07)\%$
f_D	$(18.74 \pm 0.13)\%$
$\mathcal{L}$	$238.723\ \mu\text{b}^{-1}$

Table 6.6: Summary of experimental results of this work. Only statistic errors are considered. See the text for the definition of variables.

determined for the same dataset in [20, 25]. Adopting the same strategy, one can write the veto efficiency as a product of $\varepsilon_{\text{veto}} = \varepsilon_{\text{veto}}^{\text{pileup}} \cdot \varepsilon_{\text{veto}}^{\text{EMD}}$, where $\varepsilon_{\text{veto}}^{\text{pileup}} \approx 92\%$ and $\varepsilon_{\text{veto}}^{\text{EMD}} \approx 92\%$ [20]. The value of $\varepsilon_{\text{veto}} \approx 84.6\%$ was therefore used in the following estimate and the detailed analysis of the veto efficiencies will be performed in a future study to cross-check the above-stated values.

Inserting the values from Tab. 6.6, the estimated veto efficiency of $\approx 84.6\%$, $\Delta y = 1.6$ and the branching ratio of $(5.961 \pm 0.033)\%$ into Eq. (6.2), one obtains the value of

$$0.69 \pm 0.03 \text{ (stat.) mb} \quad (\textbf{this thesis}) \tag{6.12}$$

for the cross section of the incoherent J/ψ photoproduction at $|y| < 0.8$ in Pb–Pb collisions at $\sqrt{s_{\text{NN}}} = 5.02$ TeV. This result must be considered an early estimate and potential variations could appear with the next steps of the analysis. For instance, the resulting value is very sensitive to the value of the acceptance and efficiency of the signal reconstruction, which for the time being was computed from STARlight as $\approx 4.07\%$, but might be slightly varied if one takes additional corrections into account. One option is to include the matching of the SPD hits to fired pixels, which was carried out e.g. in [20, 25]. This quality selection can, however, be applied only on the level of ESD files as the necessary data are not included at the AOD level. Hence, this would require to perform the whole analysis on the ESD level, which might be considered in an upcoming study.

It is a well-known feature of STARlight to overestimate the photoproduction cross sections because it does not take into consideration possible nuclear effects such as gluon shadowing. Assuming (for simplicity) a flat dependence of the STARlight-predicted cross section (see Tab. 6.3) across $|y| < 1$, one can divide the value by the width of the rapidity interval, $\Delta y = 2.0$, and obtain the midrapidity value of $\text{d}\sigma_{\text{J}/\psi}^{\text{inc}}/\text{d}y \approx 2.6$ mb. The estimate of ≈ 0.69 mb is also rather low compared with the predictions of the LM model in Fig. 3.6 (right), where the formalism without subnucleonic fluctuations gives the values around ≈ 1.2 mb. The GG-hs prediction of the hot-spot model by J. Cepila et. al (see Fig. 3.8) is around 0.9 mb, which is not too far away from the provided estimate. A more thorough discussion about the accordance with the various models must be also left for future work.

Conclusion

First, the motivation for the study of the incoherent photoproduction of J/ψ vector mesons in collisions of heavy ions was presented in this master's thesis. It was shown that the hadronic substructure significantly varies depending on the energy of the process. It is especially the distribution function describing the gluonic content of protons that rapidly grows with increasing energy and becomes dominant in the region of low Bjorken-x, so one can expect gluon saturation to occur. This phenomenon, however, has not yet been convincingly observed in experiments. Besides, it is known that the situation in nuclei is more complex and that the distribution of gluons inside the nucleus cannot be treated simply as a sum of the contributions from individual nucleons. Instead, a suppression is observed, which is called nuclear gluon shadowing.

In order to shed light on these processes and to refine our knowledge of the low-x nuclear gluon distribution functions, which are poorly known, the nuclear structure has to be examined. Before an electron-ion collider is built, the most promising way is to study photoproduction reactions in ultra-peripheral collisions of heavy ions. In this thesis, the photoproduction of vector mesons was studied in detail. The analysis of photoproduction processes, specifically of diffractive vector meson productions, enables us to study the transverse dependence of the nuclear structure and is also sensitive to possible fluctuations of the subnucleonic structure through the incoherent cross section. A promising way to address the fluctuations are the models employing the colour dipole approach coupled to the hot spot description, some of which were discussed in Chapter 3. Therein, it was shown that the predictions of these models indeed considerably differ depending on whether the fluctuations are taken into account or not. In general, the observation of higher values of the incoherent cross section with respect to expectations that do not include subnucleonic degrees of freedom, would speak in favour of large fluctuations at the subnucleonic scale.

The coherent J/ψ photoproduction has been studied extensively at the LHC and the latest ALICE measurements were described in Chapter 5. This chapter also proved to be a very helpful review of experimental methods that can be exploited in the analysis of the photoproduction in UPC events. The first results of my ongoing analysis of the incoherent J/ψ photoproduction at the highest energy that has been achieved so far in heavy ion collisions at the LHC, $\sqrt{s_{\mathrm{NN}}} = 5.02$ TeV, were presented in Chapter 6.

Incoherently photoproduced J/ψ mesons in the central rapidity region, $|y| < 0.8$, were reconstructed via the dimuon decay channel. After the application of selections, the incoherent-enriched sample was defined by the selection of $p_{\mathrm{T}} > 0.2$ GeV/c. It was found that the raw yield of J/ψ candidates from the fit of the invariant mass distribution, ≈ 643, is at least seven times higher than the yield obtained in the previous analysis of the incoherent photoproduction. This is reflected in a significant reduction of the statistical uncertainty. Furthermore, it was observed that the double-sided Crystal Ball functions must be used to describe the invariant mass distribution of dimuons properly.

The contaminations from coherent and feed-down processes were determined utilizing the Monte Carlo samples generated by STARlight and examining the fit of the transverse momentum distribution of measured events. The simulated MC data were also employed to estimate the acceptance and efficiency of the signal reconstruction. Lastly, the integrated luminosity of the data sample was calculated as $\mathcal{L} = 238.723\ \mu\text{b}^{-1}$. These results were used to determine the first estimate of the incoherent cross section as 0.69 ± 0.03 (stat.) mb. A slight modification can be expected to occur in the following steps of the analysis when additional corrections are taken into account. The presented value is rather low, when compared with predictions of various models.

The analysis is intended to be finished during my doctoral studies. Within this thesis, only statistical errors were considered. The detailed study of various contributions to systematic uncertainties is thus left for a future study.

Bibliography

[1] Nobel Media AB 2021. *The Nobel Prize in Physics 1990. NobelPrize.org.* https://www.nobelprize.org/prizes/physics/1990/summary/. Accessed: 2021-03-13.

[2] M. A. Thomson. *Handout 6: Deep Inelastic Scattering.* https://www.hep.phy.cam.ac.uk/~thomson/partIIIparticles/handouts/Handout_6_2011.pdf. Accessed: 2021-03-13. 2011.

[3] J. I. Friedman. "Deep inelastic scattering: Comparisons with the quark model". In: *Rev. Mod. Phys.* 63 (1991), pp. 615–629. DOI: 10.1103/RevModPhys.63.615.

[4] D. Grund. "Measurement of incoherent J/ψ photoproduction in Pb–Pb collisions with ALICE". Research project. Czech Technical University in Prague, 2020.

[5] F. D. Aaron et al. "Combined Measurement and QCD Analysis of the Inclusive ep Scattering Cross Sections at HERA". In: *JHEP* 01 (2010), p. 109. DOI: 10.1007/JHEP01(2010)109. arXiv: 0911.0884 [hep-ex].

[6] B. Martin and G. Shaw. *Particle Physics.* Manchester Physics Series. Wiley, 2008. ISBN: 9780470721537.

[7] C. Adloff et al. "Measurement and QCD analysis of neutral and charged current cross-sections at HERA". In: *Eur. Phys. J. C* 30 (2003), pp. 1–32. DOI: 10.1140/epjc/s2003-01257-6. arXiv: hep-ex/0304003.

[8] H. Mäntysaari. "Balitsky-Kovchegov equation". Master's thesis. University of Jyväskylä, 2011.

[9] F. Gelis et al. "The Color Glass Condensate". In: *Ann. Rev. Nucl. Part. Sci.* 60 (2010), pp. 463–489. DOI: 10.1146/annurev.nucl.010909.083629. arXiv: 1002.0333 [hep-ph].

[10] S. R. Klein and H. Mäntysaari. "Imaging the nucleus with high-energy photons". In: *Nature Rev. Phys.* 1.11 (2019), pp. 662–674. DOI: 10.1038/s42254-019-0107-6. arXiv: 1910.10858 [hep-ex].

[11] N. Armesto. "Nuclear shadowing". In: *J. Phys. G* 32 (2006), R367–R394. DOI: 10.1088/0954-3899/32/11/R01. arXiv: hep-ph/0604108.

[12] *U.S. Department of Energy Selects Brookhaven National Laboratory to Host Major New Nuclear Physics Facility.* https://www.energy.gov/articles/us-department-energy-selects-brookhaven-national-laboratory-host-major-new-nuclear-physics. Accessed: 2021-03-18. January 9, 2020.

[13] J. G. Contreras and J. D. Tapia Takaki. "Ultra-peripheral heavy-ion collisions at the LHC". In: *Int. J. Mod. Phys.* A30 (2015), p. 1542012. DOI: 10.1142/S0217751X15420129.

[14] A. J. Baltz. "The Physics of Ultraperipheral Collisions at the LHC". In: *Phys. Rept.* 458 (2008). Ed. by G. Baur et al., pp. 1–171. DOI: 10.1016/j.physrep.2007.12.001. arXiv: 0706.3356 [nucl-ex].

[15] J. Cepila, J. G. Contreras and J. D. Tapia Takaki. "Energy dependence of dissociative J/ψ photoproduction as a signature of gluon saturation at the LHC". In: *Phys. Lett.* B766 (2017), pp. 186–191. DOI: 10.1016/j.physletb.2016.12.063. arXiv: 1608.07559 [hep-ph].

[16] G. Herrera Corral. "Diffractive Physics with ALICE at the LHC: the control of quantum collisions". In: *J. Phys. Conf. Ser.* 624.1 (2015). Ed. by N. Bretón, D. Fernández and P. Kielanowski, p. 012008. DOI: 10.1088/1742-6596/624/1/012008.

[17] P. A. Zyla et al. "Review of Particle Physics". In: *PTEP* 2020.8 (2020), p. 083C01. DOI: 10.1093/ptep/ptaa104.

[18] E. Kryshen. "Photoproduction of heavy vector mesons in ultra-peripheral Pb-Pb collisions". In: *Nucl. Phys. A* 967 (2017). Ed. by U. Heinz, O. Evdokimov and P. Jacobs, pp. 273–276. DOI: 10.1016/j.nuclphysa.2017.05.083. arXiv: 1705.06872 [nucl-ex].

[19] J. G. Contreras. "Gluon shadowing at small x from coherent J/ψ photoproduction data at energies available at the CERN Large Hadron Collider". In: *Phys. Rev. C* 96.1 (2017), p. 015203. DOI: 10.1103/PhysRevC.96.015203. arXiv: 1610.03350 [nucl-ex].

[20] S. Acharya et al. "Coherent J/ψ and ψ' photoproduction at midrapidity in ultra-peripheral Pb-Pb collisions at $\sqrt{s_{\mathrm{NN}}} = 5.02$ TeV". In: *submitted to EPJ C* (Jan. 2021). arXiv: 2101.04577 [nucl-ex].

[21] J. Cepila, J. G. Contreras and M. Krelina. "Coherent and incoherent J/ψ photonuclear production in an energy-dependent hot-spot model". In: *Phys. Rev.* C97.2 (2018), p. 024901. DOI: 10.1103/PhysRevC.97.024901. arXiv: 1711.01855 [hep-ph].

[22] G. Baur et al. "Coherent gamma gamma and gamma-A interactions in very peripheral collisions at relativistic ion colliders". In: *Phys. Rept.* 364 (2002), pp. 359–450. DOI: 10.1016/S0370-1573(01)00101-6. arXiv: hep-ph/0112211.

[23] C. A. Bertulani, S. R. Klein and J. Nystrand. "Physics of ultra-peripheral nuclear collisions". In: *Ann. Rev. Nucl. Part. Sci.* 55 (2005), pp. 271–310. DOI: 10.1146/annurev.nucl.55.090704.151526. arXiv: nucl-ex/0502005.

[24] S. Klein and J. Nystrand. "Exclusive vector meson production in relativistic heavy ion collisions". In: *Phys. Rev. C* 60 (1999), p. 014903. DOI: 10.1103/PhysRevC.60.014903. arXiv: hep-ph/9902259.

[25] S. Acharya et al. "First measurement of the $|t|$-dependence of coherent J/ψ photonuclear production". In: *submitted to EPJ C* (Jan. 2021). arXiv: 2101.04623 [nucl-ex].

[26] T. Lappi and H. Mantysaari. "Incoherent diffractive J/Psi-production in high energy nuclear DIS". In: *Phys. Rev. C* 83 (2011), p. 065202. DOI: 10.1103/PhysRevC.83.065202. arXiv: 1011.1988 [hep-ph].

[27] T. Lappi and H. Mantysaari. "J/Ψ production in ultraperipheral Pb+Pb and p+Pb collisions at energies available at the CERN Large Hadron Collider". In: *Phys. Rev. C* 87.3 (2013), p. 032201. DOI: 10.1103/PhysRevC.87.032201. arXiv: 1301.4095 [hep-ph].

[28] J. Cepila, J. G. Contreras and M. Matas. "Collinearly improved kernel suppresses Coulomb tails in the impact-parameter dependent Balitsky-Kovchegov evolution". In: *Phys. Rev. D* 99.5 (2019), p. 051502. DOI: 10.1103/PhysRevD.99.051502. arXiv: 1812.02548 [hep-ph].

[29] D. Bendova et al. “Solution to the Balitsky-Kovchegov equation with the collinearly improved kernel including impact-parameter dependence”. In: *Phys. Rev. D* 100.5 (2019), p. 054015. DOI: 10.1103/PhysRevD.100.054015. arXiv: 1907.12123 [hep-ph].

[30] B. Abelev et al. “Coherent J/ψ photoproduction in ultra-peripheral Pb-Pb collisions at $\sqrt{s_{NN}} = 2.76$ TeV”. In: *Phys. Lett. B* 718 (2013), pp. 1273–1283. DOI: 10.1016/j.physletb.2012.11.059. arXiv: 1209.3715 [nucl-ex].

[31] E. Abbas et al. “Charmonium and e^+e^- pair photoproduction at mid-rapidity in ultra-peripheral Pb-Pb collisions at $\sqrt{s_{\mathrm{NN}}}$=2.76 TeV”. In: *Eur. Phys. J. C* 73.11 (2013), p. 2617. DOI: 10.1140/epjc/s10052-013-2617-1. arXiv: 1305.1467 [nucl-ex].

[32] H. Mäntysaari and B. Schenke. “Evidence of strong proton shape fluctuations from incoherent diffraction”. In: *Phys. Rev. Lett.* 117.5 (2016), p. 052301. DOI: 10.1103/PhysRevLett.117.052301. arXiv: 1603.04349 [hep-ph].

[33] H. Mäntysaari and B. Schenke. “Probing subnucleon scale fluctuations in ultraperipheral heavy ion collisions”. In: *Phys. Lett. B* 772 (2017), pp. 832–838. DOI: 10.1016/j.physletb.2017.07.063. arXiv: 1703.09256 [hep-ph].

[34] V. Guzey et al. “Evidence for nuclear gluon shadowing from the ALICE measurements of PbPb ultraperipheral exclusive J/ψ production”. In: *Phys. Lett. B* 726 (2013), pp. 290–295. DOI: 10.1016/j.physletb.2013.08.043. arXiv: 1305.1724 [hep-ph].

[35] L. Evans and P. Bryant. “LHC Machine”. In: *JINST* 3 (2008), S08001. DOI: 10.1088/1748-0221/3/08/S08001.

[36] L. Evans. “The Large Hadron Collider”. In: *Philosophical Transactions of the Royal Society A: Mathematical, Physical and Engineering Sciences* 370.1961 (2012), pp. 831–858. DOI: 10.1098/rsta.2011.0453.

[37] M. Schaumann. *LHC report: xenon in action*. 2017. URL: https://home.cern/news/news/accelerators/lhc-report-xenon-action (visited on 07/03/2021).

[38] K. Aamodt et al. “The ALICE experiment at the CERN LHC”. In: *JINST* 3 (2008), S08002. DOI: 10.1088/1748-0221/3/08/S08002.

[39] A. Tauro. “ALICE Schematics”. General Photo. 2017. URL: http://cds.cern.ch/record/2263642.

[40] E. Abbas et al. “Performance of the ALICE VZERO system”. In: *JINST* 8 (2013), P10016. DOI: 10.1088/1748-0221/8/10/P10016. arXiv: 1306.3130 [nucl-ex].

[41] G. Contin. “Performance of the present ALICE Inner Tracking System and studies for the upgrade”. In: *JINST* 7 (2012), p. C06007. DOI: 10.1088/1748-0221/7/06/C06007.

[42] D. Andreou. “The upgrade of the ALICE Inner Tracking System”. In: *JINST* 14.05 (2019), p. C05004. DOI: 10.1088/1748-0221/14/05/C05004. arXiv: 1904.13237 [physics.ins-det].

[43] C. Lippmann. “Performance of the ALICE Time Projection Chamber”. In: *Phys. Procedia* 37 (2012). Ed. by T. Liu, pp. 434–441. DOI: 10.1016/j.phpro.2012.02.390.

[44] J. Alme et al. “The ALICE TPC, a large 3-dimensional tracking device with fast readout for ultra-high multiplicity events”. In: *Nucl. Instrum. Meth. A* 622 (2010), pp. 316–367. DOI: 10.1016/j.nima.2010.04.042. arXiv: 1001.1950 [physics.ins-det].

[45] *Gas Amplification with Micro Pattern Gas Detectors: Amplification with Proportional Wires*. https://www.lctpc.org/e8/e46/. Acessed: 2021-03-07.

[46] B. B. Abelev et al. "Performance of the ALICE Experiment at the CERN LHC". In: *Int. J. Mod. Phys. A* 29 (2014), p. 1430044. DOI: 10.1142/S0217751X14300440. arXiv: 1402.4476 [nucl-ex].

[47] F. Anghinolfi et al. "NINO: An ultra-fast and low-power front-end amplifier/discriminator ASIC designed for the multigap resistive plate chamber". In: *Nucl. Instrum. Meth. A* 533 (2004). Ed. by P. Dupieux, R. Santonico and E. Vercellin, pp. 183–187. DOI: 10.1016/j.nima.2004.07.024.

[48] M. Broz et al. "Performance of ALICE AD modules in the CERN PS test beam". In: *Journal of Instrumentation* 16.01 (2021), P01017–P01017. ISSN: 1748-0221. DOI: 10.1088/1748-0221/16/01/p01017. URL: http://dx.doi.org/10.1088/1748-0221/16/01/P01017.

[49] S. Acharya et al. "Coherent J/ψ photoproduction at forward rapidity in ultra-peripheral Pb-Pb collisions at $\sqrt{s_{\mathrm{NN}}}$ = 5.02 TeV". In: *Phys. Lett. B* 798 (2019), p. 134926. DOI: 10.1016/j.physletb.2019.134926. arXiv: 1904.06272 [nucl-ex].

[50] C. Alexa et al. "Elastic and Proton-Dissociative Photoproduction of J/ψ Mesons at HERA". In: *Eur. Phys. J. C* 73.6 (2013), p. 2466. DOI: 10.1140/epjc/s10052-013-2466-y. arXiv: 1304.5162 [hep-ex].

[51] ALICE DPG. *Reconstructed Run-2 data taking periods: Pb-Pb*. https://twiki.cern.ch/twiki/bin/view/ALICE/AliDPGReconstructedDataTakingPeriodsPbPb. Accessed: 2021-03-30.

[52] ALICE DPG. *Lists of good runs for LHC18q*. https://twiki.cern.ch/twiki/bin/view/ALICE/AliDPGRunList18q. Accessed: 2021-03-30.

[53] ALICE DPG. *Lists of good runs for LHC18r*. https://twiki.cern.ch/twiki/bin/view/ALICE/AliDPGRunList18r. Accessed: 2021-03-30.

[54] ALICE Collaboration. *Central barrel UPC anchored to LHC18qr pass1*. https://alice.its.cern.ch/jira/browse/ALIROOT-8366. Accessed: 2021-03-30.

[55] R. Lavicka. *Analysis note: t-Dependence of coherent photo-production of J/Psi in Pb–Pb ultra-peripheral collisions*. https://alice-notes.web.cern.ch/node/1083. Accessed: 2021-03-30.

[56] J. E. Gaiser. "Charmonium Spectroscopy From Radiative Decays of the J/ψ and ψ'". PhD thesis. 1982.

[57] ALICE Collaboration. *ALICE luminosity determination for Pb−Pb collisions at* $\sqrt{s_{\mathrm{NN}}} = 5.02$ *TeV*. https://cds.cern.ch/record/2749127. 2021.

[58] ALICE UPC group. *Ultra-Peripheral Collisions at ALICE*. https://twiki.cern.ch/twiki/bin/viewauth/ALICE/UltraPeripheralCollisions. Accessed: 2021-03-30.

Appendix A

Lists of good runs

The list for the period LHC18q [52] contains 123 runs, namely

295585, 295586, 295588, 295589, 295610, 295611, 295612, 295615, 295666, 295667, 295668, 295673, 295675, 295676, 295712, 295714, 295717, 295718, 295719, 295721, 295723, 295725, 295754, 295755, 295758, 295759, 295762, 295763, 295786, 295788, 295791, 295816, 295818, 295819, 295822, 295825, 295826, 295829, 295831, 295853, 295854, 295855, 295856, 295859, 295860, 295861, 295909, 295910, 295913, 295936, 295937, 295941, 295942, 296016, 296060, 296062, 296063, 296065, 296066, 296123, 296132, 296133, 296134, 296135, 296142, 296143, 296191, 296192, 296194, 296195, 296196, 296197, 296198, 296240, 296241, 296242, 296243, 296244, 296246, 296247, 296269, 296270, 296273, 296279, 296280, 296303, 296304, 296309, 296312, 296377, 296378, 296379, 296380, 296381, 296383, 296414, 296415, 296419, 296420, 296423, 296424, 296433, 296472, 296509, 296510, 296511, 296512, 296516, 296547, 296548, 296549, 296550, 296551, 296552, 296553, 296594, 296615, 296616, 296618, 296619, 296621, 296622, 296623.

The list for LHC18r [53] includes another 96 runs,

296690, 296691, 296693, 296694, 296749, 296750, 296781, 296784, 296785, 296786, 296787, 296790, 296793, 296794, 296799, 296835, 296836, 296838, 296839, 296848, 296849, 296850, 296851, 296852, 296890, 296894, 296899, 296900, 296903, 296930, 296931, 296932, 296934, 296935, 296938, 296941, 296966, 297029, 297031, 297035, 297085, 297117, 297118, 297119, 297123, 297124, 297128, 297129, 297132, 297133, 297193, 297194, 297195, 297196, 297218, 297219, 297221, 297222, 297278, 297310, 297311, 297317, 297332, 297333, 297335, 297336, 297363, 297366, 297367, 297372, 297379, 297380, 297405, 297406, 297413, 297414, 297415, 297441, 297442, 297446, 297450, 297451, 297452, 297479, 297481, 297483, 297512, 297537, 297540, 297541, 297542, 297544, 297558, 297588, 297590, 297595.